LAWRENCE
LIVERMORE
NATIONAL
LABORATORY

UCRL-TR-236300

High Energy Density Science at the Linac Coherent Light Source

R. W. Lee

November 7, 2007

Disclaimer

This work performed under the auspices of the U.S. Department of Energy by Lawrence Livermore National Laboratory under Contract DE-AC52-07NA27344.

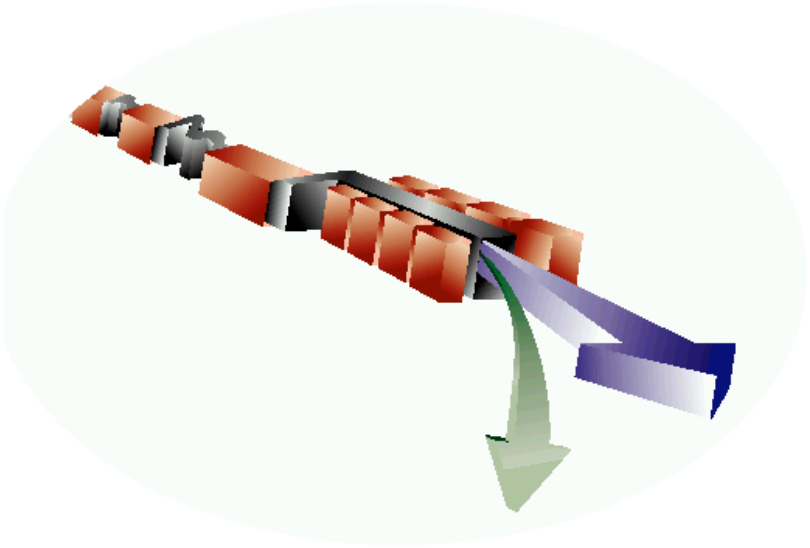

High Energy Density Science
at the
Linac Coherent Light Source

Report onWorkshop to Define the NNSA Mission Need

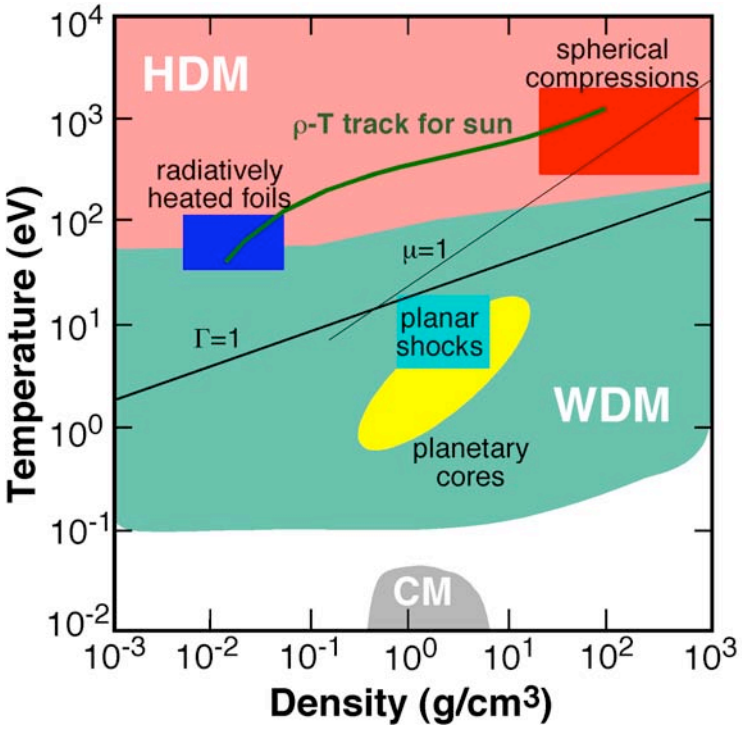

I) Executive Summary

High energy density science (HEDS), as a discipline that has developed in the United States from National Nuclear Security Agency (NNSA)-sponsored laboratory research programs, is, and will remain, a major component of the NNSA science and technology strategy. Its scientific borders are not restricted to NNSA. "*Frontiers in High Energy Density Physics: The X-Games of Contemporary Science*" identified numerous exciting scientific opportunities in this field, while pointing to the need for a overarching interagency plan for its evolution. Meanwhile, construction of the first x-ray free-electron laser, the Office-of-Science-funded Linear Coherent Light Source – LCLS: the world's first free electron x-ray laser, with 100-fsec time resolution, tunable x-ray energies, a high rep rate, and a 10 order-of-magnitude increase in brightness over any other x-ray source – led to the realization that the scientific needs of NNSA and the broader scientific community could be well served by an LCLS HEDS endstation employing both short-pulse and high-energy optical lasers. Development of this concept has been well received in the community. NNSA requested a workshop on the applicability of LCLS to its needs. "High Energy Density Science at the LCLS: NNSA Defense Programs Mission Need" was held in December 2006. The workshop provided strong support for the relevance of the endstation to NNSA strategic requirements.

The range of science that was addressed covered a wide swath of the vast HEDS phase space. The unique possibilities provided by the LCLS in areas of intense interest to NNSA Defense Programs were discussed. The areas of focus included warm dense matter and equations of state, hot dense matter, and behavior of high-pressure materials under conditions of high strain-rate and extreme dynamic loading. Development of new and advanced diagnostic techniques was also addressed. This report lays out the relevant science, as brief summaries (Ch. II), expanded descriptions (Ch. V), and a more detailed plans for experiments (Ch. VI), highlighting the uniqueness the HEDS endstation will play in providing mission-relevant HED data and in the development of the field.

One of the more exciting aspects of NNSA-relevant experiments on LCLS is that, given the extraordinary investment and consequent advances in accurate atomic-scale simulations of matter (to a large extent via the Accelerated Scientific Computing program sponsored by NNSA), the facility will provide a platform that, for the first time, will permit experiments *in* the regimes of interest *at* the time and spatial scales of the simulations.

In Chapter III, the report places the potential of LCLS with an HED science endstation in the context of science required by NNSA, as well as explicating the relationship of NNSA and HED science in general. Chapter IV discusses 4th-generation light sources, like LCLS, in the context of other laboratory technologies presently utilized by NNSA.

The report concludes, noting that an HED endstation on LCLS can provide access to data in regimes that are relevant to NNSA needs but no mechanism exists for providing such data. The endstation will also serve to build a broad-based community in the "X-Games" of physics. The science generated by the facility will be a collaboration of NNSA-based laboratory scientists and university-based researchers. The LCLS endstation fulfills the need for an intermediate-scale facility capable of delivering fundamental advances and mission-relevant research in high energy density science.

II) Mission Relevance of LCLS Experiments

The LCLS will be a unique instrument that can provide data in regimes of high energy density unobtainable by any other facility. The combination of brightness, tunability, and short timescale permit the ability to create and probe HED matter *in situ* in controlled conditions. Four general areas, and their relevance to NNSA missions, are briefly noted below. One of the more exciting aspects of NNSA-relevant experiments on LCLS is that, given the extraordinary advances in accurate atomic-scale simulations of matter, the facility will provide a platform that for the first time will permit experiments in the regimes of interest *at* the time and spatial scales of the simulations.

A) Warm Dense Matter and Equations of State

Warm dense matter (WDM) is an intriguing and largely unexplored state of matter that can be very roughly described as midway between condensed and plasma states. Molecular dissociation, partial ionization, strong coupling, nonlinear transport, and indeterminate quantum statistics make WDM very complicated but is a state that a solid must pass through en route to becoming a plasma. Accurate equations of state (EOS) – the relationship of density, temperature, pressure, and energy density for the system of interest – permit prediction of the state of a system and its evolution. For NNSA applications, knowledge of the EOS in the HED regime is extremely important. There are several reasons to study the WDM regime and EOSs with the LCLS. First, with LCLS one will be able, for the first time, to probe the conditions under which WDM is produced. Thus, a field of research that was once daunting will be turned into fertile ground for exciting research very much at the leading edge. Second, with the advance of theoretical methods, predictions will be made that will require verification by experimental data. Progress will in this complex regime requires theory and experiment can be compared directly. Indeed, as we show in detail below, the error in the WDM EOS can be significant even for the most studied materials. The LCLS will be able to provide data in this regime. Third, there are important mission-oriented research requirements where LCLS can provide data *in* regimes of largest uncertainty.

B) Hot Dense Matter

As owners/funders of large-scale, high-energy optical laser facilities, NNSA has considerable interest in higher temperature, dense plasma regimes. High temperature plasmas at electron densities in excess of 10^{21} cm^{-3} are produced with lasers (wavelengths $\lambda_L > 0.25$ μm) that do not directly heat the solid as they can not propagate beyond the critical electron density; however, heat flow from the surface efficiently generates the hot dense medium. This is the fundamental mode for the production of x-rays in indirect drive inertial confinement fusion and the source of the ablation employed in the direct drive inertial confinement fusion. The interaction of lasers with matter is central to the NNSA program and the LCLS will provide a unique experimental platform to study the basic interactions and the process of plasma formation.

The spectroscopic observations from these plasmas provides diagnostic information about the plasma itself, while permitting investigation of the mechanisms at play in the creation of the plasma and the interaction of the atoms/ions with the plasma in which they are embedded. Here the LCLS will provide two related and intriguing opportunities. First, the ability to perform Thomson scattering on plasmas at solid density will be a major step towards *in situ* probing of hot dense matter – and WDM – which has, to date, relied on non-interfering probes, *e.g.*, the

emitted radiation. Here for the first time we will be able to interrogate matter that is both hot and dense on time scales on 100-fs time scales to measure temperatures, densities, mean ionization state, *etc*. Second, we can explore laser pump-probe techniques for high-density plasmas that have been used in low-density plasmas to measure line shapes, observe radiation redistribution, and determine the kinetics processes. The LCLS will provide a major advance in the development of our understanding of intrinsic line shape formation, level shifts, radiation transfer, and detailed kinetics processes – all of which play a role in the formation of relevant high energy density plasmas.

C) High Pressure States under High Strain Rate

The strength, and other material properties, of solid-state materials are very uncertain at extremely high pressures, (*e.g*. see Fig. V.8). Experimental access to high-pressure, high-strain-rate systems is important as these are a part of the phase space that is reached in matter at extreme transient conditions, which is relevant to defense program science. Moreover, the dynamic response and strength of solid-state materials under extremely high strain-rate deformations are equally uncertain. In regimes where low-strain-rate data exist, *i.e*., when $d\varepsilon/dt < 10^4\ s^{-1}$, material models are largely in agreement with the data and each other. However, at higher strain rates the models diverge rather dramatically, with all current models assuming a transition to some other process. Since there are little or no data on high pressure, high-strain rate deformation mechanisms and strength, there are very large uncertainties. What is needed is a careful and systematic set of high pressure, strain-rate data to bound the models at P >> 1 Mbar, $d\varepsilon/dt >> \sim 10^3\ s^{-1}$. These measurements must be *in situ*, requiring preparation of the high-pressure, high-strain state and measurement on the same, very fast, timescale. These conditions can be achieved with experimental capabilities of the LCLS.

D) High Pressure shocks and phase transitions

When a crystal is shocked above its Hugoniot Elastic Limit (HEL) it starts to deform plastically, and the shocked state of the material – the Hugoniot - asymptotes to that of the hydrostat. In the limit of negligible shear strength within the solid, pure hydrostatic conditions would be reached. That is, if one started with a cubic crystal, and shocked it under uniaxial strain conditions far above its HEL, the shocked part of the crystal should comprise, assuming the absence of any induced polymorphic phase transition, a cubic crystal once more but with reduced lattice spacing. The processes occurring on the lattice level to enable such atomic rearrangement to take place under uniaxial strain conditions have been the subject of intense debate for decades. Plastic flow is known to occur due to the generation and movement of dislocations. Using this as the starting point, one would conclude that the plastic strain rate, $\dot{\varepsilon}$, within a shocked sample would be determined by Orowan's equation, $\dot{\varepsilon} = Nbv$, where N is the number of mobile dislocations, b the magnitude of the Burgers vector, and v the mean velocity with which the dislocations move.

There is one major problem associated with the above simple model. Plastic strain rates within shocked samples can be deduced from strain-profile measurements, and hence the Nbv product is presumed known. The lattice type determines the Burgers vector, and it is presumed that the velocity of the dislocation cannot be supersonic; hence, the strain rate measurement places a lower bound on the number of dislocations present within the sample. When this dislocation density is calculated, it is usually is up to 3 orders-of-magnitude higher than the

dislocation density measured in recovered post-shock samples. This is the crux of the problem – how were the dislocations generated during the shock, and why are they never seen in post-shocked materials? A satisfactory resolution of this problem is of fundamental importance to the field of shock physics – if we do not know what occurs within a shock at the lattice level, what understanding do we have? Since shocks, phase changes and high pressure states in general are a essential by-product of inertial compressions, the study of these process is critical to NNSA and the ability to measure the processes involved on the time scale and spatial scale the can match the fundamental simulation will be a boon to the fundamental understanding of these states.

III) The Mission Need Workshop:

A) Background and Motivation for the Workshop

High energy density (HED) science as a discipline was born out of the research programs at the NNSA laboratories. The scientific research motivated by the nuclear weapons mission and the availability of large-scale experimental facilities capable of achieving the extreme conditions of HED matter were unique in that environment and much of the research that was being pursued was classified into the early 1990's. Over the past decade, the NNSA laboratories have increasingly opened their doors to the broader scientific community, including access to their large-scale experimental facilities and state-of-the-art computing resources. Coupled with the many revolutionary advances in both experimental and computational tools over that time, allowing universities to house increasingly sophisticated capabilities on their campuses, involvement of academic researchers in this exciting field has increased steadily.

The field of high energy density science is in many ways unique among the core disciplines relevant to NNSA missions and as such presents several challenges. HED science is at a critical juncture in its development. The report "Frontiers in High Energy Density Physics: The X-Games of Contemporary Science" (National Academies Press, Washington, DC, 2003), commonly referred to as the Davidson report, identified numerous scientific opportunities in this field, but pointed to the need for interagency research initiatives to advance the field, currently scattered across numerous research areas in the physical sciences including astrophysics, plasma physics, and fusion energy science. An interagency working group was formed to address this question and to help shape the future of this discipline. This working group identified the need to develop the key attributes of other well-established subfields of physics, including an 'owner' in the government to steward development, as an essential first task.

The Davidson report identified the need for an intermediate scale facility to help focus and galvanize this community, one that would allow access to both NNSA's researchers, who are expert in the use of large, extremely complex experimental facilities, as well as academic researchers, more comfortable in 'laboratory-scale' facilities typically found at universities. In response to this need a proposal has been put forth to build a high-energy-density science experimental endstation at the Linac Coherent Light Source (LCLS), an Office of Basic Energy Sciences (BES) facility currently under construction at the Stanford Linear Accelerator Center (SLAC).

LCLS is free-electron laser designed to produce coherent photons at x-ray wavelengths, an x-ray free-electron laser (XFEL). When completed it will be the brightest source of keV

radiation on Earth by 10 orders-of-magnitude, in tunable bunches with 100 fsec resolution. The XFEL will be used in forefront experiments in bio-imaging, femtochemistry, nanoscale dynamics, and atomic, molecular and optical science. The incredible brightness and short timescale also make LCLS an ideal facility for HED studies. The LCLS Scientific Advisory Committee strongly endorsed a HED experimental endstation and its proposed scientific program, though BES deemed HED science to be outside its portfolio.

NNSA requested a workshop to explore the mission-specific scientific case for this HED endstation. This report, which documents the mission-relevant scientific opportunities it affords, and summarizes the current state of the HED endstation project and its future prospects is the result of that workshop. Approximately fifty participants from the NNSA laboratories, LBNL, SLAC and the academic community convened at LLNL for two days in December of 2006 for this purpose. The agenda and participant list from the meeting are contained in the appendices.

B) NNSA Mission Need for Science and Technology

Since the cessation of underground nuclear testing and the formation of a science-based certification program in the 1990's, the weapon certification and assessment process has relied on increasingly sophisticated simulation tools. During the nuclear testing era detailed understanding of all the physical processes underlying weapon operation was not required because aggregate results from simulations could be calibrated to test data. However, the need to maintain confidence as the stockpile moves steadily away from the tested regime, through aging, numerous small changes introduced via life extension programs, or new requirements, dictates that emphasis is now be placed on enhancing the *predictive* capability of weapon simulation codes. Science and technology are key underpinnings of this program and have allowed confident certification and assessment of the stockpile for more than a decade.

The development of a truly predictive capability has focused the weapon science program on addressing the major uncertainties present in current understanding at a level of detail heretofore unnecessary. This entails detailed studies of the behavior of materials present in the stockpile including plutonium and other metals, energetic materials, polymers, foams and ceramics under the wide variety of conditions relevant to operation of a nuclear explosive, studies of matter in the high-energy-density regime including opacities and other radiative properties, and nuclear properties. This work includes experimental, theoretical, and simulation studies and also includes a strong component of interaction with the broader scientific community to ensure that adequate scrutiny of methods and conclusions is provided.

NNSA has determined that it will undergo a "Complex Transformation" in the coming years, consisting of four strategies to achieve goals of the process. The first three concern development of Reliable Replacement Warheads, refurbishment of legacy designs, accelerated dismantlement of the Cold War stockpile, and modernization of the defense programs complex.

The fourth strategy is to drive the science and technology base essential for long-term national security. This strategy has several components. The first is to maintain the essential science and technology base at the NNSA laboratories to ensure their ability to meet their ongoing commitments to the stockpile, current and future. This also requires a strong S&T program to attract and retain the workforce required to carry out this important mission. Second it emphasizes the need to support the broad national security mission, including nuclear non-

proliferation and activities in support of other government agencies. Finally, it puts a strong emphasis on the need to aggressively pursue partnerships with the DOE SC and other leading R&D sponsors to effectively leverage the NNSA investment in S&T. This final component is essential to maintaining the health and vitality of the S&T programs at the NNSA laboratories.

C) Relationship of the NNSA S&T Mission Need to High Energy Density Science

Numerous scientific disciplines form the suite of core competencies required for the NNSA laboratories to support their defense missions. These include materials science, chemistry including energetic materials, polymers, and nuclear radiochemistry, engineering, nuclear, condensed matter and shock physics, and the emerging discipline of high energy density science. In each of these areas NNSA takes care to ensure that vigorous programs are in place in academia to ensure that well-qualified scientists and engineers will be available to ensure the success of their important national security mission.

The NNSA laboratories have long been leaders in the field of HEDS due to the scale and complexity of experimental facilities required to access these regimes in the laboratory. These regimes can be categorized using the definition of "high energy density" put forward in the Davidson report. Therein "high energy density" was defined as energy densities exceeding 10^{11} Joules per cubic meter (J/m^3), or equivalently, pressures exceeding 1 megabar (Mbar), was provided and shall be adopted here. Researchers have continually looked for better ways to both create and probe matter in these regimes to drive a more fundamental understanding of its properties and to address key uncertainties relevant to nuclear weapon performance.

HED matter is terrestrially rare and is prodigiously difficult to simultaneously create, characterize, and measure. Numerous important questions remain to be addressed regarding HED matter including developing accurate equations of state, determining radiative properties and opacities, and probing the behavior of materials, including transport properties, under extreme conditions such as high-pressure shock and isentropic compression. The enhanced focus in Defense Programs on developing a predictive capability, informed and validated by high fidelity experimental data, requires significant advances in the study of HED matter and significant mission drivers were identified in several areas that will be discussed further within this report. The assembled workshop participants did not believe that the restriction of unclassified research in place at SLAC would substantially diminish the impact of research at LCLS within the Defense Programs mission. However several research topics were identified that, were this option to be made available, would be of interest to pursue. These will not be discussed further here.

D) Capabilities of the HED Science Proposal for LCLS

This document contains descriptions of a set of HED experiments that will be performed at the Linac Coherent Light Source (LCLS). These experiments are unique to the coming generation of light sources as they all employ the LCLS laser to produce an unprecedented flux of x-rays that interact with the samples of interest, causing substantial alteration of the sample in the process. The short time (100 fsec) resolution of LCLS permits meaningful measurements on the timescale of the experiment. *i.e., in situ* measurements. Although there are examples of experiments on current light sources, where heating and/or perturbing matter is achieved, in those experiments the light source is used as a probe and not the "pump." In the present proposals the laser-like

qualities of the LCLS – short pulse duration, high number of photons per pulse, >10 Hz repetition rates, and tunable photon energies – make these experiments possible. The experiments described below are unique to an XFEL.

The uniqueness of the facility has attracted a substantial number of researchers to a capability that is yet in its infancy. The proposals here represent areas of research covering a wide range of topics from condensed matter physics to plasma science. More than 100 individuals have been involved at various levels in the production of this document, and are cited in the proposal. This represents only a small number of those that will be involved at the outset of the fielding of the experiments; however, given the newness of using light sources as described below this indicates a rather substantial interest in the broader community.

The experiments can be grouped broadly as having their primary focus in finite-temperature condensed matter, higher temperature plasma states, and high pressure states.

Experiment	Brief Description
Warm Dense Matter Creation	Use XFEL to uniformly warm solid density samples
Equation of State Measurements	Heat and probe a solid with an XFEL to provide a diagnostic of material properties
Shock Phenomena	Create shocks with a high-energy lasers and probe with the XFEL
XFEL / Solid Interaction	Use XFEL directly to create extreme states of matter at high temperature and density
Pump–Probe experiments	Use XFEL as a pump to excite bound-state populations and study radiation redistribution
Diagnostic Development	Develop the XFEL for Thomson scattering, interferometry, and radiographic imaging
High Pressure Studies	Validate imaging techniques. Study shock, high pressure states, phase transitions, material properties at high pressure and strain

IV) Defining Interdependence: HED Science, NNSA, and XFELs

A) High Energy Density Science and X-ray Sources

Since the late 1960's laboratory research into finite temperature dense matter had moved toward higher density regimes. Then with the advent of laser-produced plasmas and laser-based plasma diagnostics, which fueled interest in the formation of plasmas at densities nearing solid density, the possibilities of creating and probing matter at conditions that started to approach solid density became both scientifically interesting and necessary. However, due to the limitation of visible lasers, which cannot access regimes with electron densities higher than ~ 10^{22} cm^{-3}, the access or ability to selectively pump these systems was not possible. The obvious solution would be a x-ray laser which can penetrate high density matter; however, after much research on laboratory-based x-ray lasers [1], the current state-of-the-art is a fixed wavelength VUV laser with > 10 picosecond temporal duration, operating at 14 nm on a many-minute duty cycle. These

laboratory x-ray lasers are insufficient to realize the goal of performing HEDS experiments.

On the other hand, the development of synchrotron-based light sources, the 3rd generation of which provide broad-band x-rays on a virtually continuous basis to numerous users simultaneously, has provided some potential to perform HEDS in a small set of experiments. The basic drawback of the light sources is that the intensity is low so that the experiment must be repeatedly to build up signal. This is acceptable for many applications, but not for the study of HED matter that is highly transient; the limitation requires that the physical conditions be repeatable on a shot-to-shot basis. This greatly limits the utility of the 3rd generation light sources in HEDS.

Finally, in this brief review, we note that lasers can produce x-rays indirectly by illuminating a sample, effectively up-converting the visible light to x-rays.[2] Indeed, this method can produce sufficient x-ray intensity and has a temporal duration of 10's ps and remain the primary x-ray diagnostic source on high energy lasers, *e.g.*, the LLE Omega Laser. Further, many of the experiments to be proposed here have been validated by experiments perform on large-scale lasers on long time scales.

Therefore, although we can access an extremely limited part of the HED phase space with 3rd generation light sources and can access some part of the HED phase space with high-energy lasers at 100-ps time scales, there are many experiments that require a novel x-ray source. Such a source is the LCLS, an x-ray laser-based SASE process [see Appendix VII.A]. The LCLS has the combined advantages of the visible laser and x-ray light source; it will be extremely intense, be tunable, reach wavelengths of 0.15 nm, have repetition rates > 50 Hz, and operate as a science-based user facility with multiple experimental stations.

To recapitulate, we require three critical features from an experimental source for the study of HEDS. First, since the matter is at finite temperature and dense, the time scales for change are rapid; we require a sub-picosecond time scale. Second, as the matter is dense we require x-rays to provide *in situ* pumping and/or probing. This translates into the need for x-rays and given the desire to pump specific energies states, requires a tunable x-ray source. Third, due to the intrinsically statistical nature of the creation of HED matter we find that obtaining data on single shots is important. This translates into the need for an intense source so that data can be taken on as few shots as possible.

B) Evolution of the NNSA Mission to Laboratory-based Experiments

The use of high-energy lasers to create matter at high temperatures and densities is a component integral to the future of the NNSA science program. These lasers provide the means to pursue fusion energy in the laboratory and to create matter at extreme conditions. However, no matter which experiment is being pursued the basic idea, for the creation of hot dense matter, is that the laser interacts with a sample and the laser energy is up-converted to x-rays through the processes of laser-matter interactions and plasma production. These interactions are, at their most fundamental, non-local thermodynamic equilibrium (NLTE) processes. Further, the time scales of importance in the formation of the hot dense matter are rapid, as the temperatures are high, the densities are high and ionization stages created are large, *e.g.*, ten-times ionized or more: a combination of physical conditions that leads to sub-picosecond collisional and radiative rates. As these conditions are created by physical phenomena, the fundamental study of which requires

a high intensity – to provide data in a single experiment – short pulse duration – to provide sufficient temporal resolution to investigate unchanging conditions – an x-ray source –necessary to penetrate the dense matter – we again arrive at the need for a versatile x-ray laser capability, which is precisely what the LCLS will provide. It is important that the use of high-intensity lasers, for example, petawatt laser systems, to create intense absorption sources would also benefit from the LCLS capability as the underlying mechanism that give rise to the production of the high-Z emitters via the laser-matter interaction can be studied in detail. As examples of NNSA mission-oriented high-energy laser experiments that would be augmented by an x-ray laser source, one sees that the high temperature holhraum campaign now pursued at the Omega Laser [3], and the holhraum filling experiments, see for example Dewald et al. [4], depend on the details of the laser-matter interactions. Finally, the development of the x-ray Thomson Scattering as an *in situ* probe of the HED matter can be developed using the x-ray laser as a source. The prototype x-ray Thomson Scattering experiments are currently being developed on high-energy lasers and in fact now provide the proof-of-principle experiments for the future Thomson Scattering experiments on the LCLS.

C) The Free Electron Laser: an X-ray Light Source and X-ray Laser

There are several separate areas where proposed next-generation light sources, which will be the free-electron-based, can play a critical role in moving these fields substantially forward. The first is in the area of warm dense matter (WDM) research where the LCLS will provide major improvements over the current state of the field. The second is in the area hot dense matter where the role of the 4th generation light sources, which are in this regard essentially x-ray lasers, will provide substantive improvements. Third, with a tunable, intense source of sub-picosecond coherent photons one can develop truly novel diagnostic capabilities to probe matter at extreme conditions. These developments include x-ray Thomson scattering, coherent x-ray imaging of dynamic systems, and pump-probe techniques extended into the x-ray regime. Finally, there is the study of high-pressure states where the x-ray laser coupled to both long pulse high-energy and short pulse intense lasers will allow measurements of matter at extreme conditions. For more information on the facility see the website http://www-ssrl.slac.stanford.edu/LCLS/ for information on the LCLS facility.

For the 4th generation sources we note that whether we are interested in creating WDM, performing Thomson scattering, or probing a plasma, the LCLS capability provides a major advance on any capability that exists with 3rd generation sources where NNSA maintains a presence. The key to the advance is the tunable, narrow band x-ray source with very short pulse duration. Since the individual bunch photon intensity is the essential quantity for all the research into matter in the high energy density regime, comparing peak spectral brightness, *i.e.*, the number of photons per mm^2-s-milliradian^2-Hz in 0.1% bandwidth, best summarizes the comparison of the LCLS to current synchrotron sources. Indeed, one finds a 10 order-of-magnitude enhancement that makes the LCLS a most promising source. The utility of the high repetition rate of other sources, *e.g.,* APS or ESRF, are not relevant here since we require a single photon pulse to either heat, scatter, or probe matter that is transient. Indeed, to create solid matter at temperatures greater than 1 eV temperature before hydrodynamic expansion occurs demands the capability of the LCLS. This, then, will provide for HED samples that have gradients small compared to the size of the heated volume. Further, the coupling of a intense short pulse laser source at the future XFEL facility provide, *e.g.*, shock heating. In this manner

the x-ray FELs will provide advances into the WDM regime.

As an example of the diagnostic promise of the LCLS we find that to measure the Thomson scattering signal in a dense plasma or the WDM regime requires a probe, with temporal duration that is short compared to the evolution of the system, but long enough to probe the plasma collective modes. The nominal ~100-fs pulse duration will be able to probe the electron feature, arising from the collective behavior of the electrons and this will be discussed below. Further, pump-probe techniques applied to high energy density matter requires a short pulse high-energy source. For the x-rays to be useful as a probe requires a spectrally tunable source for which the number of photons-per-mode must be on the order of unity. Photons-per-mode is a measure of the probe's ability to dominate a radiative transition required to provide observable signal - due to the high peak brightness the 4th generation sources this will become possible.

V) HED Science Relevant to NNSA Needs

In this chapter we explicate those scientific areas, of concern to NNSA, where the LCLS can have critical impact. The first three sections expand on and elucidate the areas briefly summarized in Chapter II. Noting that new diagnostics techniques and advanced forms of extant techniques are always desired, the fourth section describes how LCLS will enable such developments. In each of these areas, a set of possible LCLS experiments has been mapped out. Details on those experiments can be found in Chapter VI.

A) Warm Dense Matter

1) Overview

The area of WDM refers to that part of the density-temperature phase space where the standard theories of condensed matter physics and/or plasma statistical physics are invalid. Thus, WDM refers, on the one hand, to states from liquid to greater than solid density with temperatures comparable to the Fermi energy. On the other hand, it also refers to those states of matter that are plasma-like, but are too dense and/or too cold to admit to standard solutions used in plasma physics. This is the region where plasmas become strongly coupled so that perturbation approaches fail as no small expansion parameters exist. Moreover, it is the region where the temperature of a solid nears or exceeds the Fermi temperature, thus indicating the failure of standard cold condensed matter approaches. Warm dense matter, therefore, defines a region between solids and plasmas, a regime that is found in planetary interiors, cool dense stars, and in every plasma device where one starts from a solid, *e.g.*, laser-solid matter produced plasmas as well as all inertial fusion schemes. Experiments into the WDM regime at the LCLS will provide a solution to the problem of probing dense matter on sub-picosecond time scales.

Indeed, in general, the study of dense plasmas has been severely hampered by the fact that laser-based methods have been unavailable. The single most useful diagnostic of local plasma conditions, *e.g.*, the temperature (T_e), the density (n_e), and the ionization (Z) has been Thomson scattering. However, due to the fact that the critical electron density where visible light will not propagate, is ~ 10^{22} cm^{-3} indicates that all dense matter can not be probed in depth. Moreover, as the plasmas become denser one reaches regime where the ideal plasma theories break down and this will certainly occur in cool dense plasmas.

2) Discussion

The LCLS with its short duration pulse containing a substantial number of high-energy photons can be used to probe solid matter at finite temperatures, *i.e.*, WDM. The interest in the WDM regime arises because in dense plasmas the atoms and/or ions will start to behave in a manner that is intrinsically coupled to the plasma. That is, the plasma starts to exhibit long- and short-range order due to the correlating effects of the atoms/ions. This intriguing regime where the plasma can no longer be considered a thermal bath and the atoms are no longer well described by their isolated atom behavior provides a tremendous challenge to researchers. In the limit of dense cool plasmas one obviously arrives at the threshold of condensed matter. Here the problem has changed from a perturbative approach to ground state methods where complete renormalization of the atom/ion and it environment is essential.

From the prospective of plasma studies the defining quantity is the coupling parameter Γ which is the ratio of the inter-atomic potential energy to the thermal energy given by the equation:

$$\Gamma = \frac{Z^2 e^2}{r_0 kT} \quad \text{where } r_0 = \left(\frac{3Z}{4\pi n_e}\right)^{1/3}$$

here Z is the ion charge and r_o is the interparticle spacing given in terms of the electron density n_e. The regions of interest span the density-temperature phase space going from modestly coupled ($\Gamma \leq 1$) to strongly coupled ($\Gamma > 1$), while bridging the transition regimes between solid to liquid to plasma.

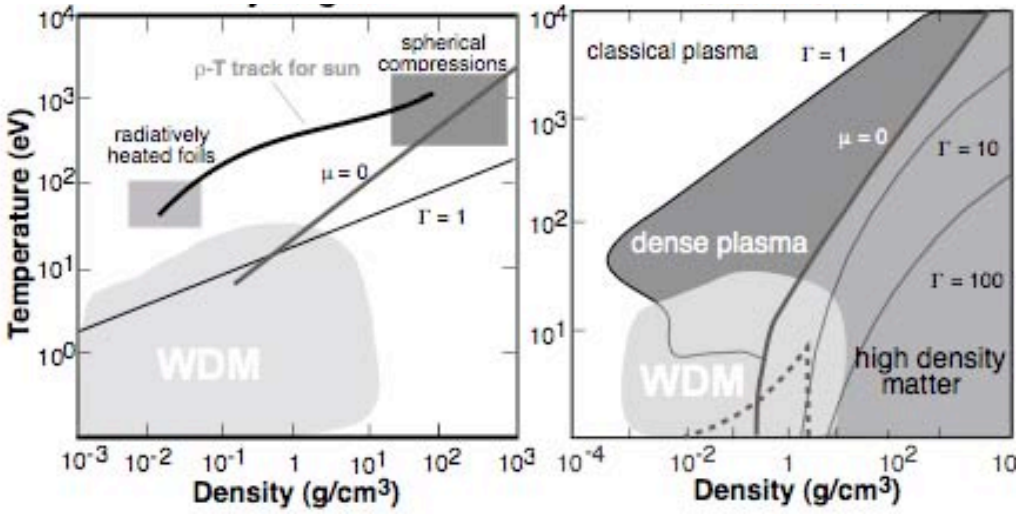

Fig. V.A.1. The temperature-density phase diagram for hydrogen on the left and aluminum on the right. The relevant regimes are noted, as are the various values of the strong coupling parameter Γ. The regions greatest uncertainty are roughly noted by the black outlined areas. Also indicated is the region where degeneracy will become important: it is the region to the right of the line where the chemical potential $\mu = 0$. The hydrogen data is taken from a compilation of data from the NRL Plasma Formulary [5] while the aluminum data is derived from the QEOS formalism (see Ref. [6])

In Fig. V.A.1 above we show the region of the temperature-density plane where WDM studies are important. Here we show the temperature (T) in eV versus the density (ρ) in g/cm^3 both for hydrogen, a low Z element, and aluminum, a moderate Z element. The region where the theoretical uncertainties are largest are those where the standard theoretical approaches fail and experiments are exceedingly difficult. The difficulty arises theoretically from the fact that this is a regime where there are no obvious expansion parameters, as the usual perturbation expansions in small parameters used in plasma phase theories are no longer valid. Further, there becomes an increased importance on density-dependent effects, *e.g.*, pressure ionization, as the surroundings starts to impinge on the internal structure of the ion or atom. Experimentally the study of WDM is difficult, as the isolation of samples in this regime is complicated. Indeed, although the plasma evolution of *every* ρ-T path that starts from the solid phase goes through this regime and plays an important role in its evolution, trying to isolate WDM remains a major challenge.

The study of WDM offers the possibility of exploring new frontiers in diverse areas, including strongly coupled plasma physics, high temperature condensed matter physics, planetary science, astrophysics, as well as extremely high-pressure chemistry. Moreover, in many areas of research the transition from a cold dense solid to tenuous hot plasma occurs in a time-dependent manner, being important to the physical description of the system and its evolution. Examples are numerous, with the most obvious being the density–temperature (ρ-T) track of inertial fusion targets, laser produced plasma sources, and shock heated systems.

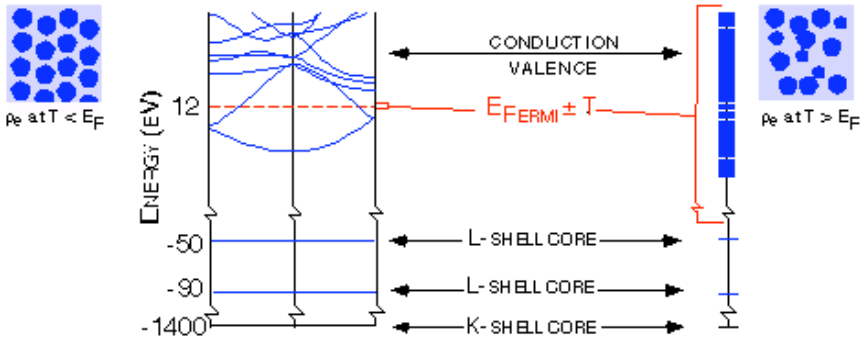

Figure V.A.2. A schematic energy level diagram that indicates the difficulties with treating the WDM regime. The electron density distributions, ρ_e, for both low and high temperature relative to the Fermi energy is shown on the upper left and right, respectively.

However, from a condensed matter perspective strong coupling is not the relevant measure, as the matter is fully structured and correlated. In a condensed matter system the issue becomes the temperature of the system relative to the Fermi energy, E_{Fermi}. In the case where the $T < E_{Fermi}$ the normal methods of condensed matter theory will work as only a few valence/conduction bands need to be taken into accounts. However, when $T > E_{Fermi}$ the number of bands that are required to describe the system become enormous. In addition to the shear number of bands, one must also include both excited core states and ionized species in the description, as multiple species are required. This is shown schematically in Fig. V.A.2.

The importance of WDM studies is threefold:

- First, with LCLS one will be able, for the first time, to probe the conditions under which WDM is produced. Thus, a field of research that was once daunting will be turned into

fertile ground for exciting research at the leading edge.

- Second, with the advance of theoretical methods future predictions will be made that will require verification by experimental data. Thus, progress will only be possible in this complex regime when theory and experiments can be compared. Indeed, as we show below in detail the error in the WDM EOS can be significant. As a simple example we show in Fig. V.A.3 the temperature-density phase diagram of Al and Cu, which are experimentally the two most studied elements, where the contours are percent differences in two EOS tables that are in both valid but show very large disagreements in the lower temperature dense region. That is, they are in disagreement in the WDM regime. Moreover, and importantly there is a path for both Al and Cu where the errors disappear. These paths of agreement are actually where EOS data exists from shock experiments – making the point clear that data is absolutely essential to provide guidance in this part of phase space. The LCLS will be able to provide data in this regime as will be discussed below.

- Third, there are important mission-oriented research requirements, e.g., weapons related studies, that come directly into the area of WDM. Indeed the regimes of largest errors and uncertainties in many of the applied research areas of, for example, chemistry and physics come in the warm dense regime.

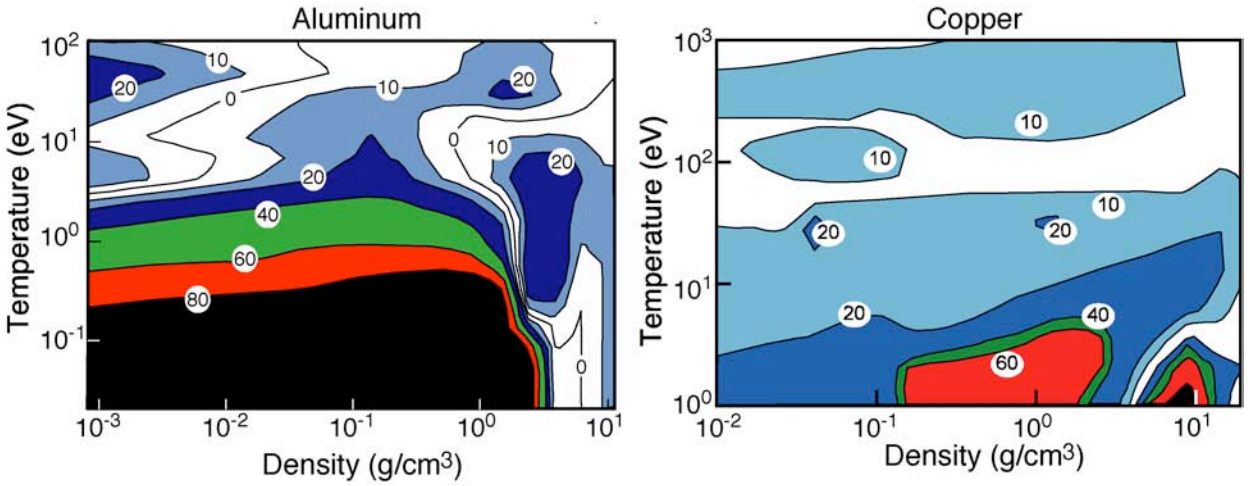

Figure V.A.3. The temperature-density contour plot for aluminum, left, and copper, right. The contours represent the pressure differences in percent of two valid EOS models. The regions of the largest discrepancies are in the WDM regime. The tracks, in white, denote the path where experiments have provided guidance for the theoretical EOS model, illustrating the essential part that high quality experimental data plays in the development of WDM EOS.

The data we expect to obtain from WDM experiments are mainly equation of state (EOS) data. The EOS is a thermodynamic description of matter - pressure-density-temperature – that is a description of how matter reacts to any change in one of those three variables. The EOS is, in effect, a description of matter; it is the component of a problem that specifies, *e.g.*, whether one is using uranium or air. There are regimes where we believe that we can accurately depict the EOS of a material: an ideal gas, possibly with plasma effects, describes extremely high temperature matter; condensed matter theory works well for normal room-temperature

conditions; Thomas-Fermi theory describes extreme densities. Warm dense matter, on the other hand, is in the complex regime in the middle. Note that the topics that affect the EOS are precisely those that effect the microscopic description of matter. Thus, the populations of all the energy level bound and/or free need to be accounted. The state of ionization, *i.e.*, whether electrons are free or bound, is an extremely complex topic when the plasma is correlated with the ionic structure. Indeed, the conductivity, the opacity, and other properties of the systems all depend on similar levels of understanding. Therefore, the EOS data provides a test of our fundamental understanding of these systems.

The development of a WDM equation of state can be seen in Fig. V.A. 4 where we show a temperature-density phase diagram for copper. The EOS in the various different regions of the phase diagram is calculated with different approximations. However, the region inside the oval is the WDM regime and is a combination of disparate approximate schemes.[7] at the limit of their applicability. Moreover, and importantly, some of the WDM regime has no known valid theoretical constructs. From the view of applications in hydrodynamics simulations the situation, indicated by the left-hand phase diagram of Fig. V.A.4, proved untenable for two reasons. First, to construct an EOS using the numerous approximations took over a month. Second, and more importantly, the EOS thus generated could not be made a smooth function of the thermodynamic variables over the entire phase space, due to the fact that the schemes are reaching their limits at the boundaries. This latter problem led to numerical instabilities in hydrodynamic simulations and thermodynamic inconsistency. To resolve this problem in the late 1980's a new form of single approximation EOS was devised, [6] which although not coming to grips with the WDM regime sped up the production of EOS tables and allowed hydrodynamic simulations to run – albeit providing questionable answers at times. This ploy has been likened to pulling a tarp over the abyss, leaving us with no WDM EOS.

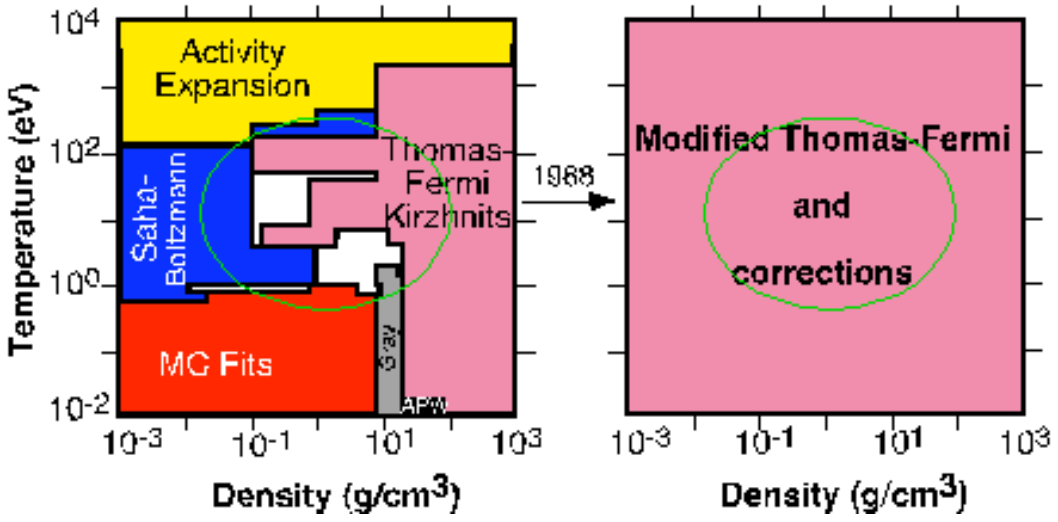

Figure V.A.4. The phase diagram for copper as constructed from all the various theoretical models. Note that the oval indicates the WDM regime where large parts have no valid description or are on the boundaries of validity. The phase diagram on the right indicates the solution to the problem: cover the problem over.

There is also an astrophysical interest in WDM. Large planets and low-mass stars exist in a state that can be described as WDM. This is true whether the major constituents are hydrogen

and helium or more complicated compounds. A correct description of a brown dwarf requires consideration of elements at Mbar pressures over a range of high densities and temperatures. Theories of formation of planetary bodies rely on structure models that are in turn determined by fundamentals like EOS and constrained by observations. While there are good observations of the large solar planets, extrasolar planets are more difficult. By far the largest uncertainty in the structure of extra-solar planets is the EOS, which is the EOS of WDM [8].

It has been exceedingly difficult to perform experiments in the WDM regime, which is, simply, why we know so little about it. The first step is to create a well-characterized WDM state; the second step is to gain information on the state through experiments. The first step has been the problem: WDM is not a limiting case of matter, *e.g.*, high- or low-temperature. When created in a laboratory environment, it does not tend to remain in a specified thermodynamic state for very long, making characterization difficult. To be able to do this on macroscopic samples with a 100 fs x-ray pulse using the 4^{th} generation sources will be a boon.

3) Summary

The study of WDM can be substantially advanced by access to new experimental capabilities. The production of WDM in the laboratory is in itself not difficult but, as it is an inherently transition state of matter between condensed matter and plasmas, it is essential to create the WDM in a manner that can be isolated. Broadly speaking there are two paths to access WDM states that can be studied. The first is to expend a large amount of energy to create, over timescales greater than 10 ps, warmed solid matter that is constrained hydrodynamically. This method has been proposed for ion beam machines and has been successfully employed at high-energy lasers to demonstrate x-ray Thomson scattering, see Section V.D.1. These experiments provide a good example of both the quality of data attainable and the amount of energy required. The second method is to provide a heating source that is sufficiently rapid, i.e., on time scales much less than the hydrodynamics, that the warmed matter is create and measurements can be performed before temporal variation and spatial gradients obviate isolating a unique state. This latter approach has been the goal of numerous intense short pulse laser experiments and has had very limited success due to the lack volumetric uniform heating. The LCLS will move this approach to the point where a volume can be heated rapidly by the intense short pulse LCLS x-ray source and then probed with the LCLS itself and/or with short pulse intense visible lasers. Finally, the repetition rate of the LCLS, at 120 Hz, is more than sufficient to allow a phase-space parameter studies to be performed cost-effectively, while providing training and technique development for researchers whose goal is to reach the higher temperature limits of WDM regime on the large-scale facilities.

B) Hot Dense Matter

1) Background

There is interest in the higher temperature dense plasma regime within NNSA. Here the problem arises from the production of high temperature plasmas at electron densities in excess of 10^{21} cm^{-3}. In any experiment where a high intensity, *e.g.*, $I \geq 10^{12}$ W/cm^2, laser irradiates a solid target there will be a region of the solid that is hot and near solid densities. Lasers with wavelengths $\lambda_L > 0.25$ μm do not directly heat the solid as they can not propagate beyond the critical electron

density n_{cr}, where $n_{cr} \approx 10^{29} cm^{-3} / \lambda_L^2$ (Å) [9]; however, heat flow from the surface efficiently generates the hot dense medium. This is the fundamental mode for the production of x-rays in indirect drive inertial confinement fusion, and the source of the ablation employed in the direct drive inertial confinement fusion. Thee interaction of lasers with matter is central to the NNSA program and the LCLS will provide a unique experimental platform to study the basic interactions and the process of plasma formation.

The spectroscopic information derived from these plasmas provides, on the one hand, diagnostic information about the plasma itself, while on the other hand we can investigate, using spectroscopy, our understanding of the mechanisms at play in the creation of the plasma and the interaction of the atoms/ions with the plasma in which it is embedded. Here the LCLS will provide two related and intriguing possibilities. First, there is the possibility to perform Thomson scattering on plasmas at solid density, see the Section V.D.1. [10,11] The development of a robust x-ray Thomson scattering capability at the LCLS will be a major step towards *in situ* probing of hot dense matter – and WDM – which has, to date, relied on non-interfering probes, e.g., the emitted radiation. Here for the first time we will be able to interrogate matter that is both hot and dense on time scales, less than 1 ps, that allow one to ascertain in a single experiment the temperatures, densities, mean ionization state etc. of the high energy density matter. The development of an x-ray Thomson Scattering source will be discussed below, as it is an application that holds out tremendous promise for providing detailed information in much of the phase space associated with matter at extreme conditions.

Second, we can explore laser pump-probe techniques for high-density plasmas that have been used in low densities plasmas to measure line shapes, observe radiation redistribution, and determine the kinetics processes. For examples of the radiation pumping see Back [12] and Koch [13] where it can be seen that, to date, in higher density plasmas only the total emitted fluorescence has been studied in photopumping experiments of ion emitters. Through photopumping one can extract information on the mechanisms involved in the plasma formation. Further, using a laser as a pump to selectively populate levels, providing a redistribution of the emitted radiation, can illuminate the details of the population kinetics. In a particularly intriguing possibility, one will be able to study the formation of plasma x-ray lasers that currently depend on kinetics processes [14, 15]. Thus, one could disentangle the plasma production from the inversion-forming processes that lead to the x-ray lasing. Numerous aspects of plasma spectroscopy have been severely constrained by a lack of data. The LCLS will provide a major step forward in the development of our understanding of intrinsic line shape formation, level shifts, radiation transfer, and detailed kinetics processes – all of which play a role in the formation of relevant high energy density plasmas.

These studies would use the high-energy laser and/or the short pulse intense laser to create the plasma source. However, the direct interaction of the LCLS x-ray laser with matter will provide novel regimes that may be of great use in future applications. The direct use of the LCSL can be broadly separated in to two regimes, which we discus briefly below, the interaction with underdense matter, that is, matter at less than solid density, and the interaction with solid density matter.

2) LCLS-non-solid matter interactions

XFEL-gas interactions is built on two unique properties of the intense x-ray source: the ability to photoionize gas and create an electron distribution function (EDF) with sharp energy distribution defined by ionization stages, and the small value of the ponderomotive potential compared to optical lasers at the same intensity. The latter allows creation of the plasma with high degree of spatial uniformity, free of parametric instabilities and sources of super-energetic particles. Thus, for the first time one can engineer hot uniform plasmas with prescribed EDFs over a wide range of conditions. In the proposed experiments, the gas will be both irradiated and probed by the LCLS beam. The Thomson scattering measurements are used to determine plasma parameters and details of the EDF. They will provide a proof-of-principle for x-ray Thomson scattering and will enable further developments and applications of this powerful diagnostic. The anisotropy of EDF in photoionized gases gives rise to unique plasma physics processes, such as electrostatic two-stream instability, Weibel instability, magnetic field generation, and terahertz radiation emission. Measurements of the magnetic field and of the emitted radiation will provide additional detailed diagnostics of these plasmas.

The relevance of the XFEL-gas studies is directly related to two important aspects of the NNSA program. First, the interaction of the short pulse intense lasers to generate the backlight beam for experiment on NIF is fundamentally produced by strongly non-Maxwellian distributions creating highly ionized plasmas. The basic mechanisms by which these non-Maxwellian plasmas evolve over the relevant time scale can be studied in situ at the LCLS. Second, the interaction of the intense beams needed to create the fast ignition sequence is an inherently non-Maxwellian process. The study of the underlying mechanisms that both create the beams and the physical processes involved in the beam matter interactions can be studied *in situ* be use of the short pulse intense laser or the LCLS with solid matter and the probing of the interaction region by the LCLS on the appropriate time scales.

3) LCLS-solid interactions

XFEL-solid interactions play an important role in the long history of the use of high-energy laser beams to generate high energy density matter in the laboratory. The single most compelling application from the NNSA standpoint is inertial confinement fusion and the associated high energy density investigations. In this context, it is of interest to use short-wavelength laser light to couple efficiently to the solid. The plasmas generated by direct irradiate of solids with LCLS will be unique as one can expect primary photo-electrons to have energies ~ 10 KeV, while simple estimates using Spitzer formulas indicate that free electrons thermalize within 10 fs, the excited states of the ions will have substantially longer lifetimes, and ions equilibrate only after 1 ps. However, more detailed studies indicate that the electron distributions stay non-thermal for substantially longer, which will be monitored via the emission spectra observing the effects on the line shapes, line shifts and ionization potential depression. Optical probing of x-ray heated non-conducting material via reflection and transmission can be used to characterize the time dependent evolution of the electron relaxation.

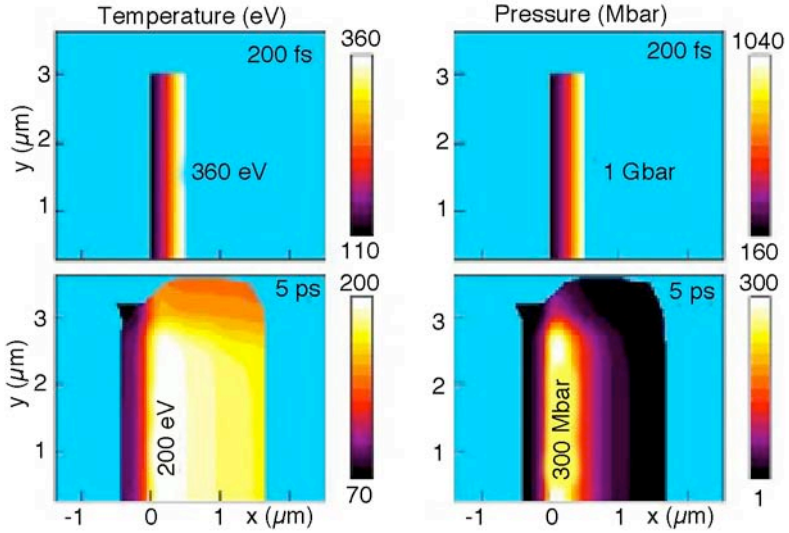

Figure V.B.1 Simulation of a 0.5 μm Au foil irradiated from the right by an XFEL with 3100 eV photons focused to 10^{17} W/cm^2. The temperature is shown on the left hand graphs and the pressure on the right hand graphs. Two time are shown the top graphs are for 100 fs after the pulse and the bottom graphs represent the conditions at 5 ps.

Indeed, the LCLS will allow rapid heating to high temperatures and pressures of high-Z matter. In Fig. V.B.5 we show the simulation results of a tightly focused XFEL beam on a 0.5 μm Au foil. The XFEL photon energy is 3100 eV and the foil thickness is 1 absorption depth at this energy. The simulation results are obtained with the MULTI code [16] that included beam energy deposition, hydrodynamics, heat conduction and radiative transport, and equation of state tables taken from the SESAME library. Since hydrodynamic expansion is mainly planar during the first few picoseconds see Fig. V.B.5, a one-dimensional simulation is relevant. The absorption of the XFEL photons was modeled with Beer's law, using absorption coefficients calculated with the SNOP code [16]. The important point here is that the XFEL can create extreme states of matter with gold at a Gbar and 300 ev being an interesting regime. However, the real issue will be the ability to verify these conditions through the development of advanced sub-ps diagnostic capabilities.

4) Summary

The advent of the next generation of x-ray light sources will bring about an advance our ability to probe hot dens matter on the same level as the introduction of the optical laser provided for interrogating atoms and near-neutral species in the 1970's. That revolution was not able to proceed to the realm of hot dense matter as a visible laser is strongly refracted and absorbed. Thus, high-energy density matter, which is central to the NNSA scientific mission, was largely understood by the use of emission spectroscopy a non-interfering probe. X-ray backlighting, which provided some inroads in understanding the *in situ* nature of these density systems, was limited to relatively long duration samples of modest temperature matter. The LCLS will allow pumping of selective transitions providing detailed information to assist in understanding the nature of laser matter interactions, population kinetics and radiative transfer. As an added bonus, the LCLS will be able to create interesting states of high-energy density matter, which will

provide novel possibilities for reaching difficult to access region of the HEDP phase space.

C) High Pressure Studies: Phase Transitions, EOS, and High Strain Rate

1) High Pressure to Study Phase Transitions and EOS

a) Background

When a crystal is shocked above its Hugoniot Elastic Limit (HEL) it starts to deform plastically, and the Hugoniot of the material asymptotes to that of the hydrostat. In the limit of negligible shear strength within the solid, pure hydrostatic conditions would be reached. That is, if one started with a cubic crystal, and shocked it under uniaxial strain conditions far above its HEL, the shocked part of the crystal should comprise, assuming the absence of any induced polymorphic phase transition, a cubic crystal once more but with reduced lattice spacing. The processes occurring on the lattice level that enable such atomic rearrangement to take place under uniaxial strain conditions have been the subject of intense debate for decades. Plastic flow is known to occur due to the generation and movement of dislocations. Using this as the starting point, one would conclude that the plastic strain rate, $\dot{\varepsilon}$, within a shocked sample would be determined by Orowan's equation, $\dot{\varepsilon} = Nbv$, where N is the number of mobile dislocations, b the magnitude of the Burgers vector, and v the mean velocity with which the dislocations move.

There is one major problem associated with the above simple model. Plastic strain rates within shocked samples can be deduced from strain-profile measurements, and hence the Nbv product is presumed known. The lattice type determines the Burgers vector, and it is presumed that the velocity of the dislocation cannot be supersonic; hence, the strain rate measurement places a lower bound on the number of dislocations present within the sample. When this dislocation density is calculated, it is almost invariably far higher –by up to 3 orders of magnitude, depending upon the shock conditions– than the dislocation density measured in recovered post-shock samples. This is the crux of the problem – how were the dislocations generated during the shock, and why are they never seen in post-shocked materials? A satisfactory resolution of this problem is of fundamental importance to the field of shock physics – if we do not know what occurs within a shock at the lattice level, what understanding do we have?

b) Recent Progress

Over past few years significant increases have been made in the understanding of the processes that take place at the lattice level within a shocked solid. On the experimental front, the application of laser-plasma-generated sub-nanosecond X-ray sources to diagnose, via diffraction, laser shocked samples has indeed confirmed that the unit cell of uniaxial shocked samples does indeed reduce in size in all three dimensions, and that such rearrangements can take place in less than a couple of hundred picoseconds.[17] On the computational front, large scale multi-million atom molecular dynamics (MD) simulations have shown how, even in perfect crystals, dislocations can be homogeneously nucleated at the shock front, and sustain plastic flow.[18] Furthermore, as has long been presumed, the MD simulations indicate that the rarefaction that inevitably follows shock compression causes the vast majority of these dislocations, composed of those of equal and opposite sign, to annihilate, and thus be unobservable in recovered post-shock samples. One of the most important tasks, therefore, now remaining is to experimentally

verify the presence of high dislocation densities *in situ* within the shocked sample.

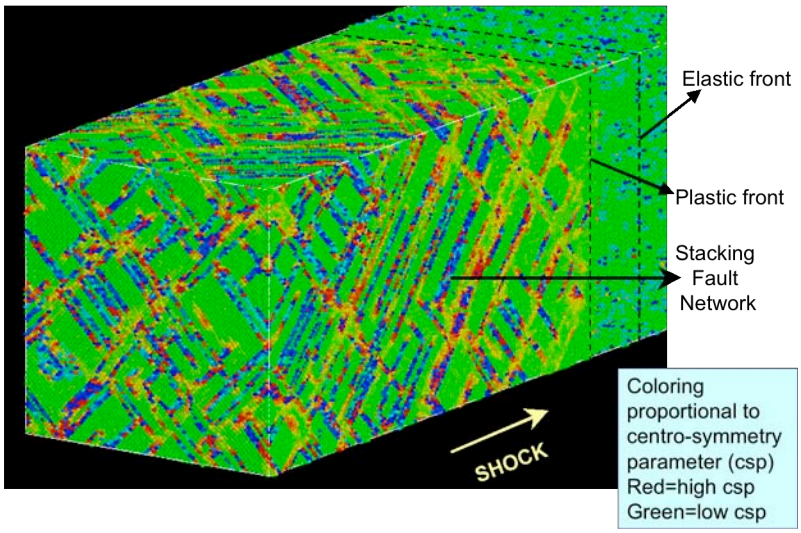

Figure V.C.1. Molecular Dynamics simulation of an FCC crystal shocked to 500 kbar. Atoms are colored according to centro-symmetry parameter. Work performed by Bringa *et al*, [19].

c) Role of the LCLS X-Ray FEL

Diffuse X-ray scattering can make the observation and measurement of high dislocation densities present within shocked materials. However, the intensities required for such observations during the brief passage of a shock wave necessitate the use of 4th generation sources. Dislocation densities can be inferred from the structure surrounding individual Laue spots. Figure V.C.1 shows a MD simulation of an FCC crystal shocked to ~ 500 kbar, in which an embedded atom potential determines the motion of the individual atoms. This is work performed by Bringa and co-workers [19]. The single crystal has been shocked along the (002) direction. Plastic deformation of the crystal has occurred by homogeneous generation of stacking faults at the shock front, owing to the high shear stresses. A partial dislocation surrounds each stacking fault, with the faults lying in {111} planes. The atoms have been colored according to a centro-symmetry parameter, by which the stacking faults are visible, as they are effectively regions of HCP crystal within the rest of the FCC lattice.

As the stacking faults lie in the {111} planes, we expect to observe them in reciprocal space as diffuse scattering emanating from each Laue spot, in the <111> directions with respect to each spot. Figure V.C.2 shows an extract from a post-processed X-ray diffraction image of the MD simulation.[20] This image represents the projection of the (002) spot onto the k_x-k_y plane in reciprocal space. Note that the peak intensity of the spot is not at k_x=k_y=0, owing to relaxation of the lattice under shock compression, although the lack of symmetry indicates that the finite number of atoms within the simulation may still play a role. The important feature to note from Fig. V.C.2 is the 'streaks' along the <111> directions, due to the stacking faults. Furthermore, a clear periodicity or typical feature size can be discerned, and the inverse of this feature size in k-space is a direct measure of the average distance between the stacking faults in real space. Note that the extent of these features is really very large –with considerable intensity being diffracted beyond 10% of the distance to the next adjacent Laue spot. This large extent in k-space is, of

course, due to the extremely high dislocation density present in real space. We reiterate, however, that such high dislocation densities within the shocked sample, although long predicted from Orowan's equation, and now also seen in far more sophisticated MD simulations, have never been experimentally observed.

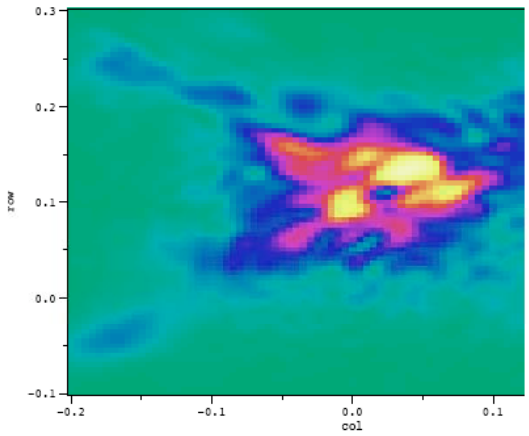

Figure V.C.2. Simulated x-ray diffraction image of the (002) spot when X-rays are scattered from the shocked crystal in Fig. V.C.1. The image is a projection down onto the k_x-k_y plane in reciprocal space.

2) High Pressure High-Strain Rate Studies

a) Background

The strength of solid-state materials is very uncertain at extremely high pressures, as illustrated in Fig. V.C.3 [21]. The blue curve shows the predictions of the full potential linear muffin-tin orbital (FP-LMTO) model for the strength of an ideal crystal sample of Ta, assuming no dislocations, giving the predicted shear stress required to deform by twinning. The red curve serves as a lower limit, and assumes that dislocations are the carriers of deformation. This calculation starts with the ambient strength, Y_0, and assumes that the strength scales directly with the shear modulus as pressure increases, ignoring work hardening and thermal effects. Again, the FP-LMTO model is used to predict the shear modulus of Ta at pressures increasing to 10 Mbar. The actual strength is expected to lie between these two bounding curves, showing that at the higher pressures the uncertainties can reach a factor ~5. If the material goes through a phase transition, the uncertainties will be even larger as Y_0 will be unknown.

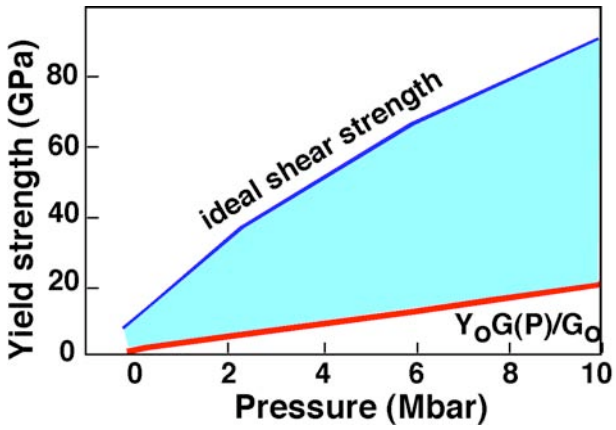

Fig. V.C.3 Pressure vs Yield strength for a Ta sample. The blue curve assumes no dislocations. The red curve assumes that dislocations are the carrier of the deformation. Y_o is the ambient strength. The G_0 is the shear modulus at ambient condition, while the G(P) is the shear modulus at finite pressure. The region between the curves is the where the actual strength will be found.

The dynamic response and strength of solid-state materials under extremely high strain rate deformations are equally as uncertain, see Fig. V.C.4. [22] In the regimes where Hopkinson data exists, $d\varepsilon/dt < 10^4\ s^{-1}$, the models are largely in agreement. However, at higher strain rates the models diverge rather dramatically. A selection of widely used high-strain rate models were used for this illustration: Hoge-Mukherjee (HM) [23], Steinberg-Lund (SL) [24], Preston-Tonks-Wallace (PTW) [25], and Raevsky [26]. The HM model assumes thermal activation as the rate-controlling process to assist pinned dislocations to surmount their obstructing barriers. SL and PTW assume the same process. Above a critical strain rate, all of these models assume a transition to some other process. HM assumes the rate controlling process to be phonon drag, with a constant drag coefficient, for strain rates above $\sim 10^3\ s^{-1}$. In this very high strain rate regime, the flow stress is then assumed to be linearly proportional to strain rate in the HM model. The SL model also assumes a transition at the same critical strain rate, $\sim\sim 10^3\ s^{-1}$, but then assumes that flow stress is independent of strain rate, and scales the strength only with the high pressure shear modulus. The PTW model is similar to HM, but differs in that its high strain rate regime is calibrated to the theory of overdriven shocks in metals, which leads to a flow stress $\sigma \sim (d\varepsilon/dt)^{1/4}$ dependence. Thus, the critical strain rate for the transition is a factor of 10^3 higher in PTW than either SL or HM models at $\sim 10^3\ s^{-1}$. Clearly there are very large uncertainties in high pressure, high strain rate deformation mechanisms and strength. What is needed is a careful and systematic set of high pressure, strain-rate data to bound the models at $P >> 1$ Mbar, $d\varepsilon/dt >> \sim 10^3\ s^{-1}$.

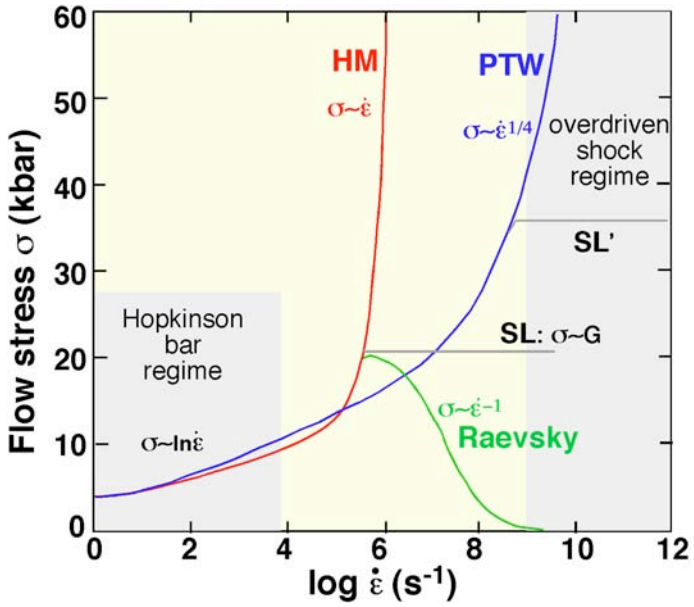

Fig. V.C.4: The dynamic response of material under high strain rate. The region of low rate is accessible by the Hopkinson Bar technique. The region of high strain rate shock is accessible by overdriven shocks. The regions in between have only recently been accessed. The various different theoretical models (see text for the definition of HM, PTW, SL, Raevsky) predict widely disparate result for the strain rate at higher flow stress.

b) Recent Progress

To develop a new experimental technique to achieve very high pressure, high strain rate dynamic conditions in the solid state, we have adapted a shockless compression technique [27] to lasers. We illustrated the technique in Fig. V.C.5, where a laser drives a strong shock through a low-Z plastic reservoir. On the left and side of Fig. V.C.5 we show the experimental concept at three different times. When the shock breaks out the backside of the reservoir, the reservoir unloads across a vacuum gap stagnating on the metal sample of interest. The accumulating ram pressure ($P_{ram} \sim \rho v^2$) gently increases in the sample without creating a shock. This allows the sample to be taken to high pressure in the solid state. [28] This technique has been demonstrated on the Omega laser in a configuration shown on the right hand side of Fig. V.C.5. [29]

Recent experiments have demonstrated the production and propagation of high stress ramp-waves that result in the quasi-isentropic compression of condensed materials. [29] This permits the sampling of thermodynamic space not accessible by near-instantaneous shock compression or static-pressure methods and ensures a solid state even at very high pressures. Depending on the ramp-wave-loading method, risetimes can be varied between nanoseconds to several microseconds. This capability enables the study of time-dependent material behavior associated with structural changes and deformation in solids subjected to extreme compressions. In these quasi-isentropic compression experiments (ICE) the EOS of a material may be determined from Lagrangian sound speed analysis from a multi-stepped target if an identical ramped stress-wave is applied simultaneously to each of the step samples. [30] Using this technique, the stress-strain response for aluminum Al-6061 has recently been determined up to a peak stress of 240 GPa when ramp compressed over hundreds of nanoseconds on the Sandia Z-machine. [31]

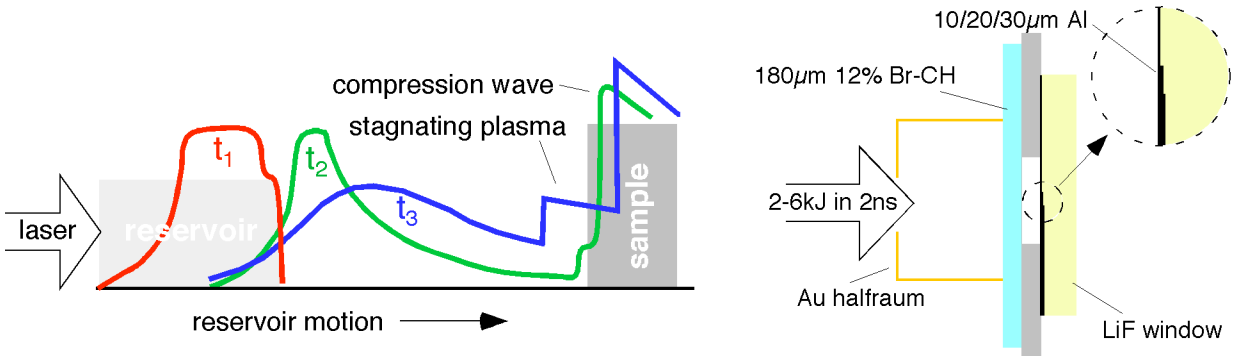

Figure V.C.5. Left hand side is the concept of the quasi-isentropic compression experiment shown at three times. Schematic of target density at three times: t_1 the shock is about to break out of the reservoir; t_2, the reservoir has unloaded across the gap and is starting to pile up against the sample initiating the shockless compression wave; t_3, the reservoir continues to rarefy, the load is increasing, and the wave in the sample is beginning to steepen. On the right hand side an experimental configuration use at the Omega Laser is show. The laser irradiates a Au enclosure which up-converts the laser light to x-rays that then impinge on the reservoir (here a 180 μm slab of brominated plastic, that will be shocked and release into the vacuum gap and then impact an Al sample that has three steps. One observes the rear surface with a VISAR to infer the break out of the stress waves.

In previously developed laser-driven ICE an ablatively driven shock in a primary target is transformed into a ramp compression-wave in a secondary target via unloading followed by stagnation across an intermediate vacuum gap. [29, 32] Using this direct laser-drive technique peak longitudinal stresses, P_x, of 200 GPa have been obtained. The planarity of the stress drive reported, however, is limited by the performance of the current state-of-the-art laser focal spot smoothing techniques, which precluded their use for EOS measurements. Previous work has demonstrated the potential for generating spatially planar ablative shocks when laser photons are first converted into x-rays within a high-Z hohlraum. [33]

Thus, a laser-produced x-ray drive has been recently develop to generate ramp-wave loading that is spatially uniform to 0.2% over 500 μm. This uniform loading ensured that different thicknesses of a multistep target had the same loading history. Ramp-loading risetimes in laser-driven ICE are more than an order of magnitude faster than with other drivers. e.g., pulsed power, gas guns, high explosives and offer new insights into the rate-dependent response of materials at high levels of compression.

In order to make reliable EOS measurements from a laser ICE a number of criteria need to be satisfied. Each thickness on the multi-step sample must experience shockless compression. If a compressive shock forms, entropy will be generated and an uncertain amount of target heating will result. In addition, the experimental design should preclude the possibility of target preheat so that the initial temperature and density conditions are well known. The pressure drive needs to be spatially planar such that each step experiences the same loading history. Finally, a detailed error analysis incorporating target and experimental uncertainties coupled with shot-to-shot repeatability is required. One central assumption for all current ramp-wave analysis techniques for extracting EOS information is that the ramp-wave is a simple wave. This implies that there is no rate-dependence in the material properties, e.g., strength as the propagating ramp-

wave steepens during transit.

To illustrate the ability to realize the ICE experiments we show in Fig. V.C.6 the applied ramp-stress waves for the target conditions described in right hand side of Fig. V.C.5 for a number of input laser energies,. Higher peak stresses and correspondingly shorter risetimes are achieved with increasing E_{laser}. An increase in E_{laser} results in an increase in the radiation temperature and therefore a higher pressure in the ablatively driven shock-wave launched into the reservoir material. Breakout of the higher shock pressure at the rear surface of the reservoir material causes the Br-CH material to unload at higher velocities across the vacuum gap. In turn this increased momentum gives rise to a higher peak pressure in the ramp-compression-wave with associated shorter risetimes.

The highest peak longitudinal stress is achieved for a E_{laser} of 5.9 kJ. For this particular shot a 20 μm Be ablator was glued onto the halfraum side of the Br-CH reservoir and a 600 m vacuum-gap was used. Be has a higher ablation velocity than the 12% Br-CH and so for a fixed input energy a higher P_{peak} is achieved. This target and irradiation geometry have been simulated with the radiation hydrodynamics code, Lasnex, with good agreement to the experimentally determined stress source, see Fig. V.C.61. Increasing E_{laser} from 2.3 kJ to 5.7 kJ, increases P_{peak} from 21 to 120 GPa. This is driven by the approximately linearly increase in T_{rad} from 105 eV to 134 eV. In these experiments T_{rad} is measured with a spectrometer composed of many x-ray filtered channels. For all E_{laser} the late time shock is observed 10–20 ns after the onset of the ramp wave. For the $P_{peak} \leq 55$ GPa the ramp waves have reached a peak before the arrival of the late time shock. In these cases EOS measurements, which are made up to the peak of the ramp-unloading-wave, would be unaffected. For $P_{peak} \geq 55$ GPa the risetime of the ramp wave has increased such that the late time shock cuts off the ramp-wave before it has reached a peak. For P_{peak} of 26 GPa the risetime of the ramp wave t_{ramp} is 15 ns truncated by the late time shock whereas for a P_{peak} of 120 GPa, t_{ramp} is 3.3 ns. The shock-up distance is shorter for shots with higher P_{peak}.

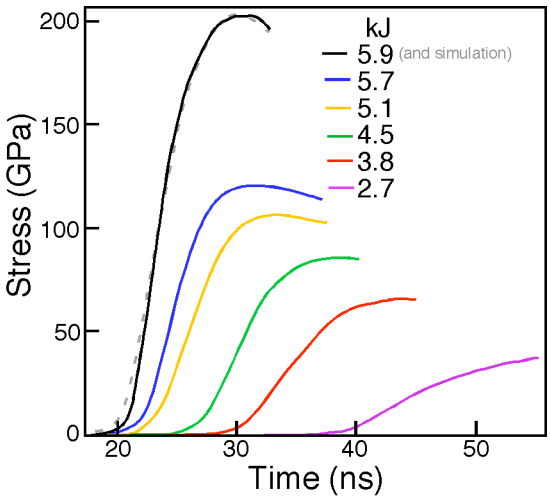

FIG. V.C.6: The time-resolved stress source is calculated from the observed stress on the rear surface of the sample via a back-integration technique. A family of loading profiles is shown as a function of input laser energy. An increase in energy results in an increase in T_{rad} and therefore higher P_{peak} in the ablatively driven shockwave launched into the reservoir material. The shock ionized Br-CH travels at

higher velocities across the vacuum-gap and the increased momentum gives rise to higher ramped peak P_{peak} in the aluminum target with associated shorter risetimes. The 5.9 kJ case has been simulated and the stress versus time is shown to be if good agreement with the experimental data.

Thus, this new technique for generating a high planarity 0.2% ramp compression over a several hundred micron region, by converting spatially inhomogeneous laser radiation into a spatially uniform temperature x-ray drive. This ensures an identical ramped-stress wave is applied simultaneously to the loading surface of a stepped Al sample. The use of a 12% Br-CH foil has been shown to be an effective heat shield from energetic x rays produced in the halfraum which could otherwise preheat the target. Using the x-ray drive technique described here, single shot EOS data close to the room temperature isentrope of pure Al has been extracted up to 110 GPa. [34] Designs predict that we will be able to extend this quasi-isentropic compression technique to above 1000 GPa on NIF

3) Summary

The LCLS HEDP capability will provide for an assortment of methods to generate high-pressure states, with the use of the high-energy laser, the intense short pulse laser or the LCLS x-ray laser. The ability to generate these high-pressure states and also probe them with the LCLS x-ray laser will create a unique resource for high-pressure research in the world. The importance of the high-pressure research at the LCLS will be critical to understand the nanoscale behavior of shocked material. The ability to measure the high pressure state on sub-ps times scales and nanometer length scales will provide critical information for the development of simulation techniques, moving toward a predicative capability. For example, simultaneous probing of a shock using all the current tools, e.g., VISARs, Fourier Domain Inferometry and long pulse x-ray backlighting, will be augmented by Phase Contrast Imaging –see V.D.3– and Thomson Scattering –see V.D.1– on sub-ps time scales. Moreover, the intensity of the LCLS will allow, in addition to Bragg diffraction, the measurement of diffuse and small-angle scattering on a single experiment. These will provide essential information on phase mechanisms and dislocation dynamics.

For the case of high pressure high strain rate studies the relatively new technique which uses quasi-isentropic compression allows access to a very much larger part of the Pressure-Temperature-Density phases space than the previous accessible using with static cells or shock generated experiments. The shockless methods are well suited to provide data a wide range of data on high-pressure high-strain rate samples. The extension of these methods to the study of failure of materials under pressure is also extremely attractive as one can reach very high heating rates and large cooling rates necessary to study matter at extreme conditions.

D) Diagnostic Developments

1) Thomson Scattering

a) Background

One can extend the power of spectrally resolved Thomson scattering to the x-ray regime for direct measurements of the ionization state, density, temperature and the microscopic behavior of strongly coupled plasmas and warm dense solids. [35] This would be the first direct measurement of microscopic parameters of solid density matter, which could be used to properly

interpret measurements of material properties such as thermal and electrical conductivity, equation of state (EOS) and opacity found in astrophysical environments as well as many plasma production devices. In current plasma physics experiment, except those discussed in V.D.1.b, the concept of Thomson scattering is use to explain the spectrum derived when a probe scatters from the free electron in a plasma. However there are three possible scattering processes that occur when photons interact with a plasma, ignoring photoabsorption: 1) there is true Thomson scattering, a coherent process, in which in the photons interact with the tightly bound electrons – as the electrons are coupled to the nucleus there is essentially no Compton shift; 2) there is the Compton shifted scattering from those weakly bound electrons that have ionization energies less than the Compton shift – this is an incoherent process; and, 3) there is the Compton shifted scattering from the unbound, i.e., free, plasma electrons – this is an incoherent process. In the standard plasma literature the latter scattering process has come to be called the "Thomson" scattering. As we speak of plasma type studies we will retain this nomenclature here, but note the various components schematically.

Thomson scattering is characterized by the scattering parameter α, proportional to the ratio of the laser probe scale-length, λ_L, to the screening length, λ_S, and the scattering angle Θ:

$$\alpha = \lambda_L/4\pi\lambda_S\sin(\Theta/2) = 1/[2k_L\lambda_S \sin(\Theta/2)\ ] \qquad \text{V.D.1}$$

For $\alpha < 1$, the scattering is due to individual electron so that the spectrally-resolved incoherent Thomson scattering provides information on, *e.g.*, the velocity v, hence temperature, and the directed flow of free electrons from the Doppler shifts experienced by scattered probe photons. For $\alpha > 1$, the collective scattering regime, the scattering is sensitive to temporal correlations between electron motion separated by more than a scattering length, hence the scattering is dominated by ion-acoustic and electron plasma wave resonances, the latter set by the Bohm-Gross dispersion relation. [9] The frequency shift of the resonance is dependent on density through the plasma frequency, while the width of the resonances yields information on the wave damping rates. In the intermediate regime, *i.e.*, near $\alpha = 1$, the form of the high frequency electron plasma component depends strongly on both the electron temperature and density, providing a robust internal measurement of these basic plasma parameters, confirmed by spectroscopy. Clearly Eq. V.D.1 will break down when the concept of Debye shielding becomes invalid as the coupling becomes large, thus necessitating the use of the screening model of Eq. V.D.1.

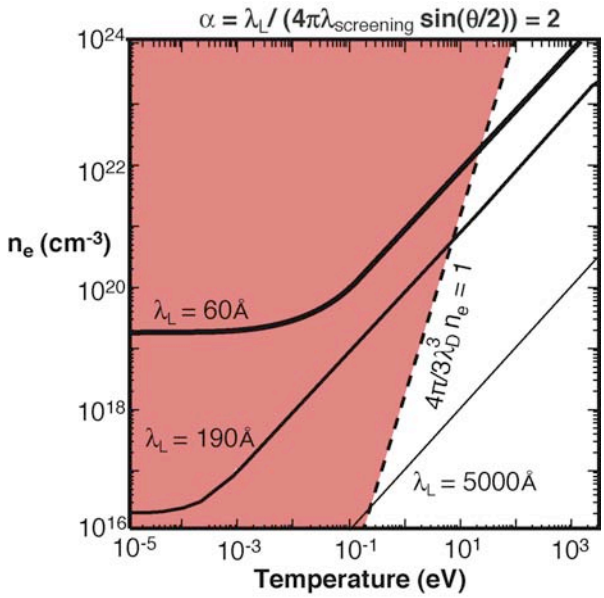

Fig. V.D.1. Temperature and density phase space indicating the nonideal plasma regime by the gray area. Nonideal is defined as a plasma for which there is less than one particle per Debye sphere. The heavy dashed line indicates the temperature density contour at which there is one particle per Debye sphere. We also indicate by solid curve the temperature and density at which the parameter a = 2 for backscatter (Q = 180°) for thee probe wavelengths. The 1 Å a = 2 curve, which requires the LCLS is at densities beyond 10^{24} indicating that the LCLS will be able to probe all density matter. The wavelengths 60 and 190 Å shown are achievable with the FLASH VUV-FEL, can probe the strongly coupled plasma regime, but will suffer severe attenuation due to absorption, whereas a standard visible laser at, e.g., 5000 Å, cannot access this region.

Figure V.D.1 shows the regions in the electron temperature and density space that can be probed by various wavelength probes. In Fig. V.D.1 the temperature and density space is divided into two regions depending on whether the number of particles per Debye sphere is larger or smaller than unity. The region above this demarcation line is essentially the region in which the strong coupling parameter Γ of Eq. V.D.1 is greater than one. For the study of strongly coupled plasmas or, more generally, warm dense matter, one would be able to probe these regions with the LCLS. In addition, in Fig. V.D.1 we show lines of constant scattering parameter $\alpha = 2$ for 180° backscattering, for three probe wavelengths of 60, 190, and 5000 Å. Stated differently, for a given plasma temperature, we should be able to access a density that is 6-7 orders of magnitude higher than previously attempted. Finally, Fig. V.D.1 indicates that for x-ray wavelengths, e.g., 1 Å, the curve of constant $\alpha = 2$ crosses into the strongly coupled plasma regime above the regime of solid densities, $\sim 3 \times 10^{23}$ cm^{-3}, indicating that this regime is accessible by Thomson scattering.

b) Current status

Currently there is several proof-of-principle experiment in x-ray Thomson scattering being performed on high-energy lasers with long pulse lengths. These experiments provide confidence that the LCLS will be a viable probe for the HEDS regime. It is understood that definite measurements of temperatures, densities, and ionization states are critically important for the fundamental understanding of matter in the high-energy regime [36, 37, 38, 39]. Novel precise techniques that make use of x-rays that can penetrate through compressed materials will be

broadly applicability to those involved in HEDS [40, 41, 42]. The current status is that experiments [43, 44] have successfully applied x-ray Compton backscattering on isochorically heated beryllium and carbon; however, the results indicate that backscattering techniques may be limited to dense plasmas of significant ionization, which will not be achieved with laser-driven compressed low Z foils [45]. The development of forward scattering techniques, i.e., the measurement of plasmons [46, 47] is required. With this development one could characterize compressed CH foil plasmas, while determining the effect of bound electrons and non-equilibrium conditions on the non-collective Compton and Rayleigh scattering spectrum obtained in backscatter geometry. Further, this provides the proof of principle experiment for those to be carried out on the LCLS.

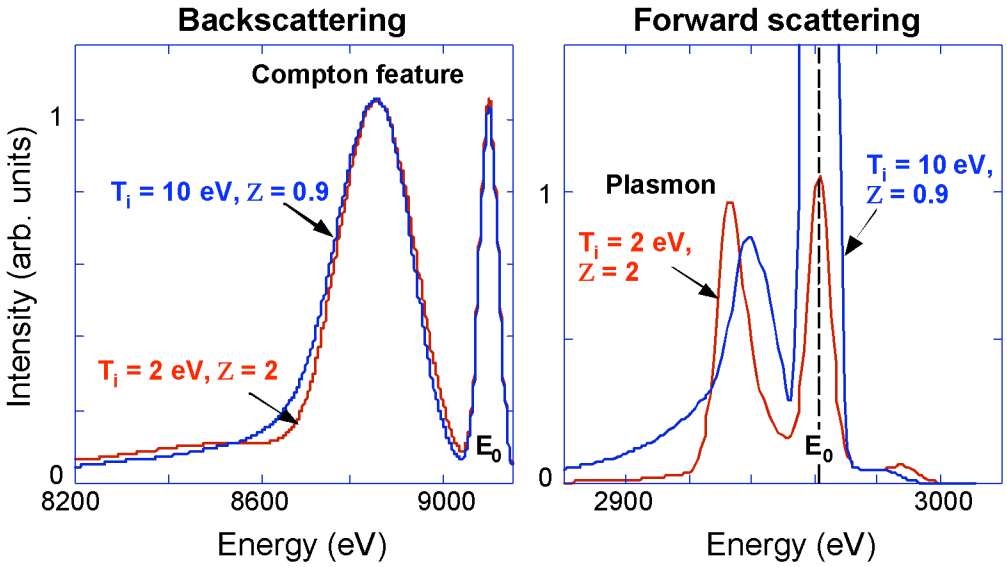

Figure V.D.2. Calculated x-ray scattering spectrum from CH in backward at θ = 120° (left) and forward at θ = 40° (right) scattering geometry for two different scattering energies and in each figure there are two different plasma conditions. Since the ionization state of Z = 2 results in significantly larger electron density of $n_e = 3 \times 10^{23} cm^{-3}$ compared to Z = 0.9 with $n_e = 1.6 \times 10^{23} cm^{-3}$ the plasmon peak observed in forward scattering is significantly more shifted from the incident x-ray probe energy E_L. Thus, forward scattering will allow a precise measurement of the electron density that cannot be obtained in backscattering geometry.

The effort to characterize under-dense and solid-density plasmas with optical and x-ray scattering, respectively, is well established [32, 33,48, 49, 50, 51]. Temperature, density, and ionization state measurements have been demonstrated in isochorically-heated solid-density plasmas using non-collective backward scattering [29] and are presently applied in numerous plasmas with a significant amount of ionization [37]. Recently, forward x-ray scattering on collective plasmon oscillations has been demonstrated. By combining these two techniques using simultaneously collective and non-collective, *i.e.*, forward and backward x-ray scattering with a suitable narrow-band x-ray source, one can accurately characterize compressed states of matter.

Figure V.D.2 shows examples of calculated x-ray scattering spectra in back scattering geometry (θ = 120°) with a Zn He-α x-ray source at E_0 = 9.1 keV and in forward scattering geometry (θ = 40°) with a Cl Ly-α x-ray source at E_0 = 2.96 keV. In the first case, we observe

non-collective scattering where the x-ray scattering spectrum shows the Compton downshifted line that is broadened by the momentum distribution of the electrons in the scattering volume. In the latter case, collective scattering conditions are reached and a plasmon is observed from collective electron oscillations.

The calculations were performed for CH plasmas with density of ρ = 1.5 g/cc and electron temperature of T_e = 10 eV. Two different plasma conditions have been investigated, the first with little effective ionization of Z = 0.9 and $T_i = T_e$ = 10 eV. The second case considers a non-equilibrium plasma with Z = 2 and T_i = 2 eV. Although these ionization stages result in very different electron densities the resulting spectra in backscattering geometry are very similar and cannot be distinguished experimentally. On the other hand, these two plasma conditions can be distinguished and precisely diagnosed using forward scattering. Figure V.D.2 clearly demonstrates that conditions in compressed matter can be reached where backscatter alone is insufficient for probing densities and ionization states. This is due to the fact that elastic scattering contributions described by the ionic form factor $S_{ii}(\mathbf{k})$ are not well understood in non-equilibrium conditions.

In the non-collective (backscattering) regime, the contribution of the free electrons that carry the information on the temperature of the solid density plasma is blended with the component from bound electrons making temperature measurements less accurate. Moreover, bound electrons with ionization energies larger than $\hbar\omega/2\pi$ (states deep in the Fermi sphere) cannot be excited, and no energy can be transferred during the scattering process. The corresponding spectral feature is a non-shifted scattering component at E_L that is commonly referred to as the Rayleigh peak whose intensity is provided by the first term of the dynamic form factor [44, 52, 53]

$$S(k,\omega) = \left|f_I(k) + q(k)\right|^2 S_{ii}(\mathrm{k}) + Z_f S_{ee}(k,\omega) + Z_c \int S_{CE}(k,\omega-\omega')S_S(k,\omega')d\omega' \qquad \text{V.D.2}$$

with Z_f and Z_C the number of free and bound electrons, respectively. It is primarily the intensity of the Rayleigh peak that has been previously applied to infer the number of tightly bound electrons and in this way the ionization state and density of the target, see left graph in Fig. V.D.2. Clearly, this procedure is dependent on the theoretical approximation made for $S_{ii}(\mathbf{k})$.

Independent of these modeling assumptions, the application of the forward scattering method will provide a unique data set on the density and ionization of compressed matter. In forward scattering we find that the plasmon frequency is a sensitive measure of the density in the CH foil plasma, see right graph of Fig. V.D.2. These scattering tools will provide precise characterization of the plasma state and further help guiding the theoretical developments of calculations of the ion-ion structure factor $S_{ii}(\mathbf{k})$ by simultaneously measuring the backscattering spectrum in these well-characterized conditions. The precise measure of the conditions in compressed matter will have a far-reaching impact on other experiments in the high-energy density science community.

c) Experimental Method: Proof-of-principal experiment

The first collective x-ray scattering experiments on plasmons have recently been performed at

the Omega Laser at LLE. These proof-of-principal measurements have used isochorically-heated beryllium at solid densities and a Ly-α x-ray source at 2.96 keV. Figure V.D.3 shows the experimental scattering spectrum along with a theoretical fit.

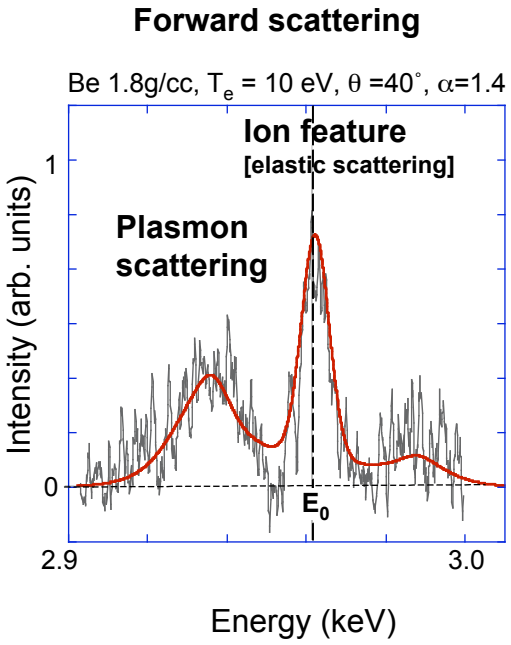

Figure V.D.3. Experimental forward scattering (θ = 40°) spectrum from isochorically heated beryllium plasmas along with best fit, indicating a 10 eV plasma . The spectrum shows the plasmon peak at 2937 eV, which is shifted from the incident probe energy E_0 = 2962 eV by 25 eV indicating solid density conditions.

For the conditions of this experiment the scattering is collective and the spectrum shows the collective plasma oscillations resulting in a plasmon peak down-shifted from the incident probe radiation E_L by ΔE_{Pl} = 25 eV. In the limits of degenerate or classical plasmas the screening length assumes the Thomas-Fermi length or the Debye length, respectively. The latter results in the familiar expression for α, see Eq. V.D.1

$$\alpha = \frac{1.08\,\mathrm{x}10^{-8}\ \lambda_0(\mu\mathrm{m})}{\sin(\theta/2)}\left(1-\frac{n_e}{n_{cr}}\right)^{-\frac{1}{2}}\sqrt{\frac{n_e(\mathrm{cm}^{-3})}{k_B T_e(\mathrm{eV})}} \qquad \text{V.D.3}$$

As expected for solid density beryllium with densities of 1.8 g/cc, we observe a plasmon frequency shift of only 25 eV. The dispersion relation for plasmons in dense matter determine the shift [54]:

$$\omega^2 = \omega_{pe}{}^2 + 3(kv_{th})^2 + \left(\frac{\hbar k^2}{2m_e}\right)^2 \qquad \text{V.D.4}$$

For conditions of isochorically heated solid-density matter or for compressed matter, the first term of Eq. V.D.4 dominates the frequency shift. With $\omega_{pe}{}^2 = 4\pi n_e e^2/ m_e$ we directly obtain

the electron density, n_e. The second term is known as the thermal correction from the Bohm-Gross dispersion relation and is of 5-10% of the total shift. We expect to measure T_e with high accuracy applying the principal of detailed balance as described below. Moreover, T_e will influence the damping of the plasmon and an estimate can be inferred from the fit to the width of the experimental data. The third term is the well-known Compton shift.

These high-energy laser Thomson-scattering experiments will provide a complete study of the detailed requirement for successful scattering experiments at LCLS. Therefore, not only will the data be important in itself, but it will also set the stage for future advancements.

2) Pump-Probe techniques

The mechanisms involved in the formation of a plasma and the details of the kinetics processes can be illuminated by using a laser as a pump to selectively populate levels and thus redistribute radiation. In a particularly intriguing possibility one will be able to study the formation of laboratory x-ray lasers that currently depend on kinetics processes. [55] Thus, one could disentangle the plasma production from the inversion-forming processes that lead to the x-ray lasing. It is clear that numerous aspects of plasma spectroscopy have been severely constrained by a lack of data. The 4th generation sources will provide a substantial improvement in the development of our understanding of intrinsic line shape formation, level shifts, radiation transfer, and detailed kinetics processes.

In both of these areas the LCLS/XFEL will provide information that would not be obtainable with any other source. The combination of the short pulse length, the tunable wavelength, the repetition rate, and the energy per pulse will make the data derived from these plasma-based experiments a major advance in our knowledge in this area.

Since the creation of high-density laser produced plasmas there have been virtually no quantitative *in situ* measurements of the kinetic rates or the populations. This is a major impediment to progress, as population kinetics of highly stripped ions is a complex problem. The complexity derives from the large number of states that must be considered in a model and the detail to which one must incorporate these states. The situation is made more difficult yet due to the fact that these plasmas tend to have rapid time evolution and large spatial gradients. [5]

Indeed, much of the effort to improve the situation has been focused on target design and advanced diagnostic development; however, the difficulties in determining the level populations or the kinetic rates remain. Therefore the interest, which comes from all areas involved with dense plasma studies and its underlying theoretical problems, *e.g.*, laboratory x-ray laser generation, laser plasma production, astrophysics, and inertial fusion, has never been met with substantial improvements in experiments.

The import of the 4th generation sources for high energy density plasma experiments is that one can use these x-ray sources to pump individual transitions in a plasma creating enhanced population in the excited states that can be easily monitored. The idea has been used in lower density plasmas with visible lasers and can, with the 4th generation sources, be employed to advance the study of high-density plasmas. [56, 57].

Variations on the idea of pumping individual transition in high energy density plasma include the selective pumping of the wings of a line transition to observe redistribution within the line profile and pumping of selected transitions to attempt to understand the inversion mechanisms for the production of laboratory x-ray lasers. In all of these applications the tests of the theoretical developments in the areas of atomic processes, kinetics model creation, line shape formation, and x-ray gain studies would be the first of their kind as there are currently no available probes.

There are several constraints on the x-ray source for it to be useful as a laser probe of the high energy density regime. First, the probe must be tunable and this is easily satisfied. Second, the line width of the pump must be such that it can pump entire line profiles and also be capable – for studies of redistribution within line profiles – of pumping parts of the line profile. Again, these conditions will be readily met. Finally, we need to have a pump that can move enough population from one state to another so that the population changes can be monitored. This last requirement can be verified by looking at the radiative pumping rate, R_{LU}, due to the source compared to the spontaneous emission rate, A_{UL}, of the transition being pumped. This is proportional to the number of photons per mode and is given by [58]

$$\frac{R_{LU}}{A_{UL}} = 6.67x10^{-22}\frac{g_U}{g_L}\lambda_{\mathring{A}}^5 I_o^{laser}\left(\frac{W}{cm^2}\right)\frac{[,]}{\delta_\lambda \Delta_\lambda} \qquad \text{V.D.5}$$

where the g's are the statistical weights of the upper and lower states, λ_L and I_o are the source wavelength and intensity. The δ_λ and Δ_λ are the bandwidths of the x-ray source and the line shape of the transition being pumped, respectively, while [,] represents the minimum of the two. Two important insights emerge when evaluating Eq. V.D.5. First, if we conservatively assume $I_o \sim 10^{14}$ and $[,]/\delta_\lambda\Delta_\lambda \sim 0.001$ we find that the ratio is approximately 1 for λ_L of 10 Å. This number is at least 10^3 larger than can be obtained by using a plasma source to pump a transition. Second, the ratio does not increase with decreasing source wavelength, indicating that large numbers of photons per mode will not be available as we move toward shorter wavelengths. This is due to the fact that the spontaneous rate has a strong inverse dependence on wavelength. Of course, matching, or at least controlling the source bandwidth can have salutary effects as indicated by Eq. V.D.5.

The possibilities provided by plasma spectroscopic probing are illustrated with the simulation of an aluminum layer tamped on both sides with a thin layer of CH plastic irradiated by x-rays.[59] An undiluted radiation field emitted from the rear side of a 1000 Å Au target impinges on the Al foil, heating it uniformly. The Au foil is irradiated by a single 1 ns, temporally square-shaped pulse of 0.52 μm light at an intensity of $1.6x10^{14}$ W/cm^2. [60, 61, 62]

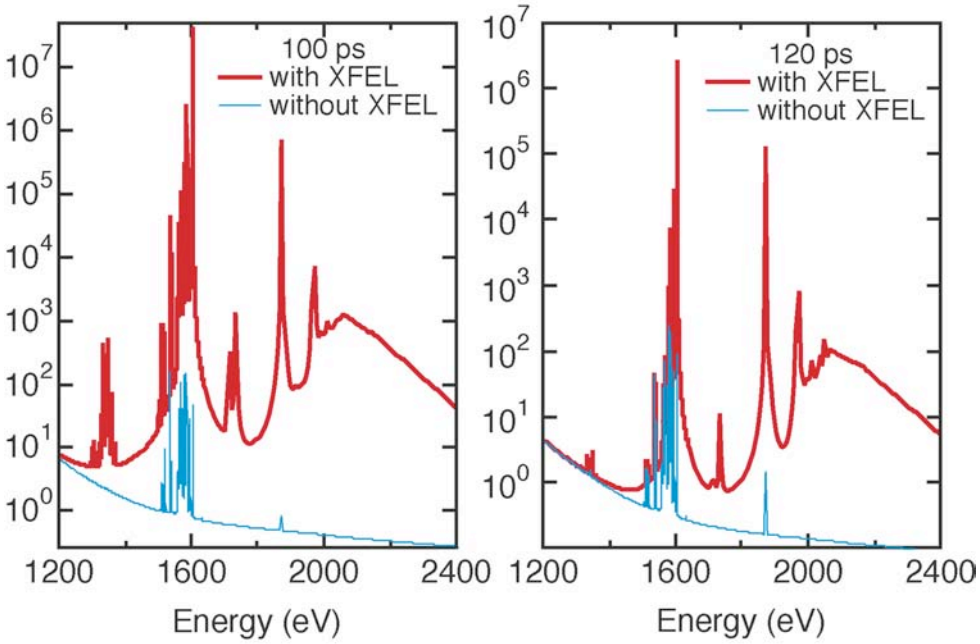

Fig. V.D.4. The logarithm of the emissivity versus spectral energy for two times in the evolution of an exploding aluminum foil. The emission from the plasma with no x-ray pump is the blue curve while the red curves indicate the emission when the XFEL pumps the He-like n =1 to n = 3 transition. The He-like emission, from, *e.g.*, n =2, 3 and 4 at 1598 eV, 1868 eV, and 1963 eV, respectively, increases substantially while the H-like n=2 emission at 1724 eV arises with the pump.

The emission spectrum will be the observable and it is shown in Fig. V.D.4 at two times in the evolution of the plasma, one at the initiation of the x-ray pulse and the other at 18 ps later. The most notable feature is that there is a substantial increase in the hydrogenic transitions. For example, the Lyman α line at ~ 1724 eV which is unobservable in the He-like background emission without the LCLS/XFEL pump, rises well above the background with the x-ray pump. Further, the structure of the He-like resonance series starting at ~1598 eV and ending at the bound-free continuum near 2086 eV is substantially changed by the pumping. Indeed, the Li-like satellite transitions seen on the low energy side of the He-like $1s^2$-1s2l transitions are substantially enhanced. The major effect of the pump, although it is tuned to a particular transition, is to cause photoionization due to the pump strength. The ionization of the Li-like stage and the pumping of population from the He-like ground state up to the H-like ion stage cause slow recombination decay back towards the He-like ground state.

It is clear from the emission spectra shown in Fig. V.D.4 that one could use a fraction of these x-ray sources as pumps to generate observable signals. The detailed information that can be obtained from these measurements would provide unique constraints on the complex processes necessary to construct a complete kinetics model for the highly charged ions. Indeed, we chose to use as an example the K-shell spectra as it is easily interpretable; however, the generation of L-shell and M-shell models is also of importance and raises the level of complexity substantially. Thus, one can understand the need for experiments that can provide basic information on the processes necessary to build kinetics models.

3) Phase Contrast Imaging: Dynamic Imaging at the nanoscale

Our current understanding of shock phenomena such as dislocations, plasticity and phase changes has benefited in recent years from careful experiments with time resolved x-ray diffraction techniques combined with optical laser drive shocks. However, there is still a long way to go in developing this understanding. LCLS will provide a unique source for such experiments. With keV photons in a well-collimated beam, it is ideally suited to probing shocks driven by high-energy lasers.

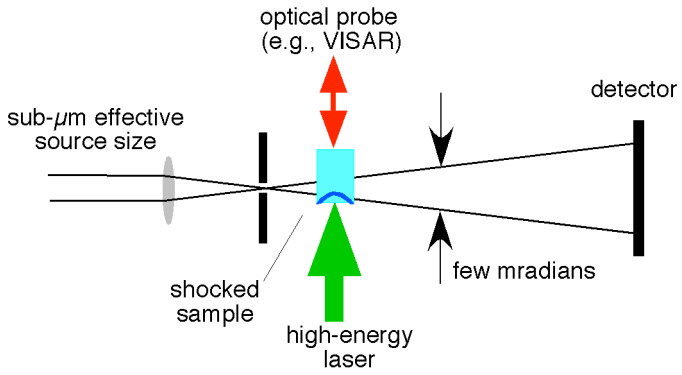

Figure V.D.5 Schematic of an example probing experiment. Previously with laser-sources the effective source size was ~10 microns and still led to some spatial coherence.

As an example we would perform the experiment schematically represented in Fig. V.D.5, where the high-energy laser is used to generate a shock in solid samples, such as a Si crystal wafer. Optical reflection techniques such as Velocity Interferometry System for Any Reflector (VISAR) can be used to diagnose the shock speed and particle velocity on exit of the shock. The LCLS beam will provide a means to probe the structure of the material after compression in the bulk of the sample. The excellent time resolution, < 1 ps, available will allow the observation of changes in structure due to phase changes to be recorded in unprecedented detail. For example, the α-ε phase transition in iron –see Fig. VI.D.1, from bcc to hcp, has been observed in laser-shocked sample. Molecular dynamics simulations suggest this occurs in ~1ps timescale, longer than the LCLS pulse duration. As mentioned above in Section V.C the high flux of the LCLS beam will allow not only the traditional Bragg diffraction peaks to be observed, but the small angle and diffuse scattering (for example from stacking faults) will be observable, adding more detail to our picture of material under pressure and high strain rates. In Fig. V.D.5 we see an example of an experiment that can be used to determine directly the compression profile in a shock wave. The spatial coherence of the source will be evident in features caused by refraction in the very steep gradients of the shock front. Some sample data using a laser produced x-ray source is seen in Fig. V.D.6. With the LCLS unprecedented temporal resolution will allow the compression, speed of the shock, and with VISAR, the particle velocity to be determined simultaneously. With pulse shaping capability added, it will be possible to investigate isentropic compressions as well as shock Hugoniots. The limit of the spatial resolution from coherent diffractive imaging in the far field will be at the 50 nm range. This puts the LCLS capability to image on the nanoscale in femtoseconds permitting for the first time shock front size measurements, phase transition kinetics, nucleation and growth information, and grain structure deformation.

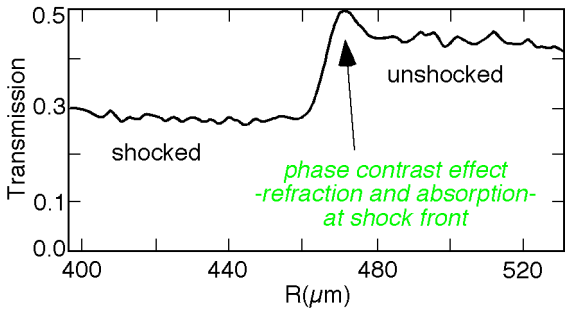

Figure V.D.6 Point projection profile of a shock front taken with a 10 micron X-ray source. Phase contrast effects are evident at the shock front. These should be more evident and provide more information with a spatially coherent LCLS with sub-micron effective source size.

4) Summary

The LCLS will provide a set of advanced diagnostics that will augment current high-energy density diagnostics by having intense, sub-picosecond, tunable x-rays. The example of Thomson Scattering, selective Pump/Probe, and Phase Contrast Imaging will reveal levels of detail never before possible in high-energy density experiments. These techniques coupled to the high-energy laser and intense short-pulse laser will move current experiments to a new level of sophistication.

VI) Experimental Descriptions

A) Warm Dense Matter and Equation of State

1) Background

The fact that the next generation FEL-based light sources will allow the creation and probing of the warm dense matter regime, as discussed briefly below, will serve to provide NNSA with a unique opportunity to develop a resource for large-scale equation of state data generation. The idea is simple, but the impact should be large, as the data obtained in the generation of the warm dense matter along an isochore, *i.e.*, a track of constant density, with subsequent probing along the release isentrope, *i.e.*, a track of constant entropy, will be unique and critically important for progress in the field.

The importance of this data derives from the fact that to date the only viable and reliable method of generating warm dense matter is exposing the material to a shock. The shock method provides information along the principal Hugoniot, that is, the locus of points in the pressure-density space that are accessed by a single shock – one point for each shock strength. Although this has been exceedingly useful, it provides a very limited set of data yielding little information on the general behavior in the warm dense matter regime. Indeed, the amount of data that is currently available is so proscribed that one finds insufficient constraints on theoretical development.

Here we discuss a more recent development that uses short pulse laser to heat thing foils. This method has been used successfully in two important cases, and after we briefly discuss the method we will make it clear how using this as a starting point will provide for future improvements in the WDM and EOS measurements.

2) Current Status

High-contrast ultrashort pulse laser facilities – pulse duration in the order of 100 fs – are capable of accessing the WDM regime. Measurements of the optical properties of these rapidly heated targets have been developed far enough to yield high-quality EOS-*relevant* data, such as the AC conductivity. The implementation of such an experiment at a short-pulse, short-wavelength laser facility – like the LCLS - would provide the additional tools necessary for performing measurements of the EOS itself. The most relevant, and most recent, example of EOS related experiments can be found in the work of Widmann et al. [63]

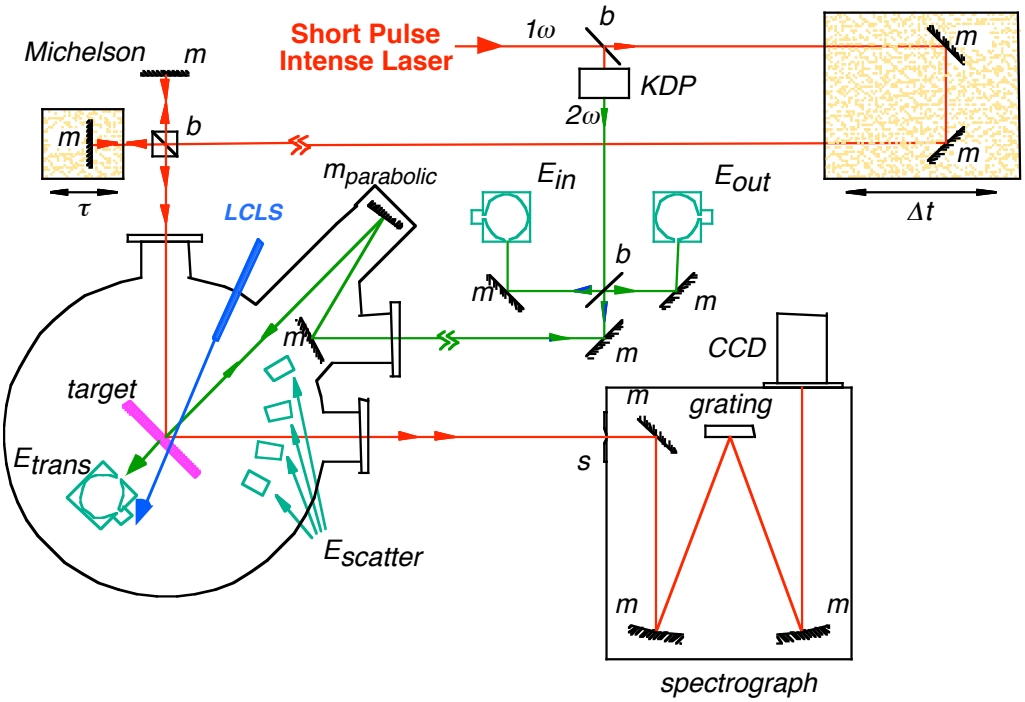

Figure. VI.A.1 The experimental setup shows the incident optical short pulse driving laser (SPL) from the left, shown in red is frequency doubled to 2ω, which is shown in green. The 1ω beam (red) is used to measure the expansion of the surface using FDI. The laser intensity is ~ 10^{13} W/cm^2 with a 100 fs FWHM pulse length. The laser is incident on a foil of thickness d ~ 300 Å. The incident energy, reflected energy, transmitted energy, and the scattered energy are measured to determine the absorbed energy.

As noted above the creation of WDM is not at issue, the problem is to create the state in manner that allows measurements of the state variables with sufficient accuracy to provide benchmarks for the theoretical development. Since the EOS relates, the state variables, e.g., temperature, density, and pressure, the measurement requires considerable diagnostic power. In the present example we emphasize independent measurements of the density and temperature. In Fig. VI.A.1 we show a schematic of the experimental setup where a thin foil is illuminated with a short pulse laser (SPL), which allows heating of the sample before any hydrodynamic motion takes place. The thin foil is required to achieve uniform heating of the solid [64]. The foil thickness needs to be on the order of one optical depth, i.e., approximately equal to an absorption length. Here the thinner the foil the more uniform the heating; however, the thicker the foil the

longer the time before it starts to move – in the terminology of shock physics – before it unloads. In the present example we compromise the two factors using a 300 Å thick foil for heating and then measuring the density and temperature. Here a SPL pulse length of 100 fs is used to achieve heating before hydrodynamic effects take place.

For the case of a 300 Å Al foil heated by an optical laser of intensity of between 10^{13} and 10^{14} W/cm^2 and pulse length of 100 fs FWHM, simulations indicates an electron temperature of between 1 – 20 eV in the solid density sample. In Fig. VI.A.2 simulation the conditions of the irradiation of a 300 Å Al foil by an optical laser with a wavelength of 400 nm (2ω), an intensity of 10^{13} W/cm^2, and pulse length of 100 fs FWHM. On the left hand side of the figure we show the time evolution of the electron temperature and the electron density of the center of the heated foil. Here the peak of the laser pulse is at 120 fs and the maximum electron temperature is ~ 3 eV with an electron density of 10^{23} cm^{-3}. This temperature can be seen to decrease to T_e = 1.5 eV at 3 ps where the electron density is seen to reduce to 10^{22} cm^{-3}. Clearly from the time evolution one needs to use a probe with time resolution of better than 500 fs. On the right hand side of Fig. VI.A.2 the electron temperature, T_e; ion temperature, T_i; and electron density, n_e, are shown at a time of 1 ps. The density and temperature profiles indicate that at 1 ps the sample has substantial gradients. However, the ion and electron temperatures, which differ by a factor of two at the end of the heating pulse, are essentially in equilibrium at 1 ps with a peak temperature of 3 eV.

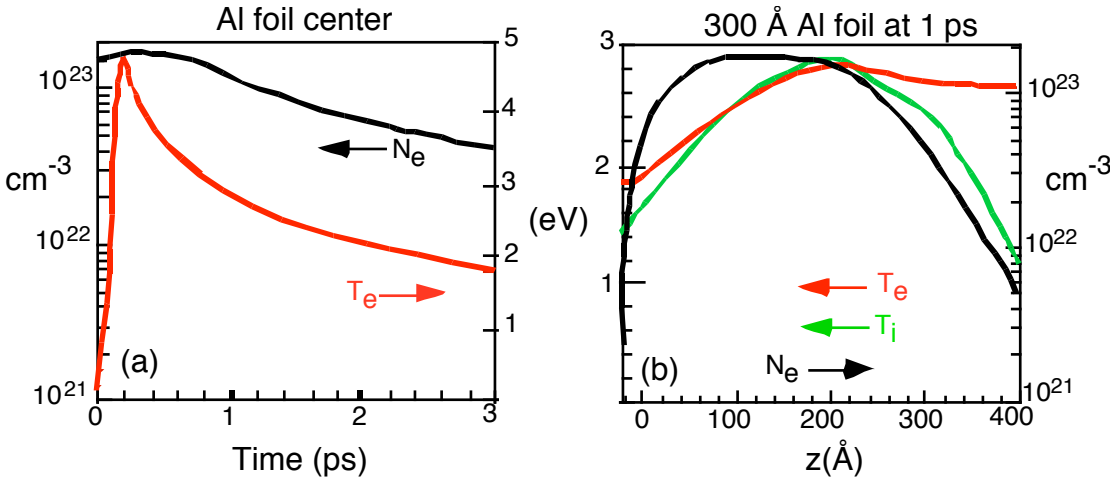

Figure VI.A.2 Simulations of the electron density and temperature and ion temperature for a short pulse laser-produced plasma of a thin (300 Å) Al foil. The laser has an intensity of 10^{13} W/cm^2 and pulse length of 100 fs FWHM and is incident from the right hand side. (a) Shows the time evolution of the center of the foil. The peak of the driving pulse is at 120 fs and the foil remains at solid density for several hundred fs after the peak of the pulse. (b) shows the temperature and density at t = 1 ps, where the ion and electron temperature come into equilibrium.

This example illustrates several of the issues that must be addressed to validate the experimental procedure. First, we note that the very quantities that we are setting out to measure, the densities and temperatures, are determined not from measurement but from simulation or inferred from the motion of the critical density surface as derived from the FDI. In other words, there are no *in situ* measurements of the conditions of the bulk of the heated foil. Further, we note that the gradients are rather large from front to back of the thin foil and this would confound the idea that we are measuring a well-defined sate of matter.

3) Future Experiments

The resolution of these problems can be taken in stepwise fashion to eventual provide a data set that is independent of simulations. The first, step is to measure the behavior of the bulk with either the use of Thomson Scattering to provide a validation of the simulations as one could then compare, on 100 fs timescales, the measured and predicted temperatures, and densities of the WDM sample. This can only be performed by the use of a short pulse intense x-ray source such as the LCLS. This information will augment the FDI to provide a better understanding of the behavior of the SPL irradiated foils. Note that this is one critical role for the LCLS in that the x-ray laser can provide essential information of the details of the experiments that are primarily carried out on long wavelength short pulse laser. In doing so the LCLS can provide validation of the experimental techniques. In Fig. VI.A.1 we note that the LCLS beam has been introduced to indicate this option.

The next step is to use the LCLS to heat the foil. First, the heating of the sample will arise from photoabsorption, which is a much better understood process than electron conduction from a critical density surface. Second the sample size can be made to match the photoabsorption length so that initial deposit gradients can be minimize. As discussed in Section V.C it will be possible to create samples of matter in the WDM regime, away from the shock Hugoniot. However, the critical point is that the samples will have small gradients on the time scale of 1 ps. This, by monitoring the incident, scattered and transmitted energy, one will have a measure of the absorbed energy density, which is a measure of one of the three variables required to establish the EOS. The situation is illustrated in Fig. VI.A.3 where we employ the LCLS with a focal spot of 20 μm on a sample of Al that is optically thin, being only ~0.55μm thick. The conditions across the foil are very uniform, with the temperature of ~11 eV corresponding to a deposited energy density of $>4x10^5$ J/cm^3. Of course, even higher energy densities can be by tighter focusing and/or using different photon energies.

It is clear that with LCLS heating the foil one would reproduce the diagnostic procedures currently used in the SPL heated sample experiments. Any difference in the results, when the deposit energy density is measured to be equivalent for similar samples, would be an indication of difficulty in the use of SPL heating. This may lead to better sample preparation and experimental technique to improve the SPL heating mechanism.

The final step would be to both heat the sample with the LCLS and then use the a portion of the LCLS split off from the main beam to determine the *in situ* temperatures and densities via one or more of the techniques discussed in Section V.D. This important class of experiments that uses the LCLS as both pump and probe by the use of grazing angle reflectors, e.g., ~0.5° for C at 3 keV. This would allow the use of a portion of the LCLS as a probe to measure the X-ray absorption for the WDM. It is important to note that the isochoric heating of the sample leads to isentropic expansion, thus the amount if information on the EOS will be substantial for each successful experiment.

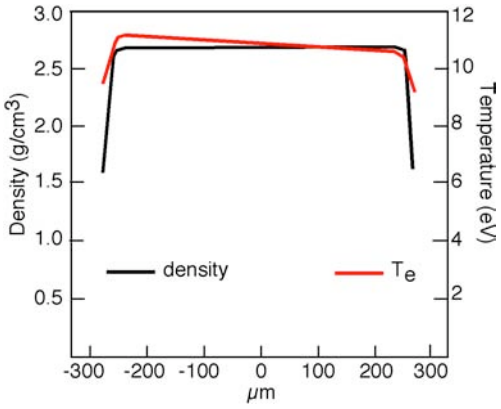

Figure VI.A.3 Density and temperature of an XFEL heated Al foil, 1ps after heating. The foil is 0.55 mm thick and is heated by 3.1keV radiation.

We note that the SPL laser will remain a useful diagnostic of WDM sample surface and for very thin samples can provide information on transmission.. That is, the SPL can provide measures of the optical properties in the ultra-thin targets discussed. Reflectivity and transmissivity can be determined at specific wavelengths and polarizations. Conductivity models can then be used to link transport properties to target conditions. From a single probe pulse the energy of the heating pulse can be inferred, spatial profiles obtained of the pump beam spot in reflection and transmission, and a spatially resolved 2D image of the target illuminated by the probe pulse in reflection and transmission. Reflectivity data could be important in understanding the melting process and expansion of the heated target. The measurement of phase shift, reflectivity and attenuation, yield a wealth of EOS quantities. FDI, which is mentioned above, is used to precisely measure the expansion-induced phase shift. FDI can determine expansion velocity, density and temperature. Thus, on the ultimate experiment there will be several measurements we would make with such a sample. One would employ both the x-ray laser and the visible laser diagnostics to determine the state of the matter.

B) Hot Dense Matter

1) Background

The interest in the higher temperature dense plasma regime arises from the central role that laser-matter interactions with solid targets play in the laboratory-based NNSA program. The most important limitation in understanding the interaction arises from the fact that we require production of high temperature plasmas at electron densities in excess of 10^{22} cm^{-3}. In any experiment where a high intensity laser, *e.g.*, $I \geq 10^{12}$ W/cm^2, irradiates a solid target there will be a region of the solid that is hot and near solid densities. Lasers with wavelengths > 0.25 μm do not directly heat the solid as they cannot propagate beyond the critical electron density, n_{cr},

$$n_{cr} \sim 10^{29} cm^{-3} / \lambda^2(\text{Å}).$$

However, heat flow from the critical density surface efficiently generates the hot dense medium. The spectroscopic information derived from these plasmas provides, on the one hand, diagnostic information about the plasma itself, while on the other hand, we can investigate the underlying physical mechanisms at play in the creation of the plasma together with the interaction of the atoms/ions with the plasma in which it is embedded. Here the LCLS will provide two related

and intriguing possibilities. First, there is the possibility to perform Thomson scattering on plasmas at near solid density, which is discussed in Section V.D.1. Second, we can explore laser pump-probe techniques for high-density plasmas that have been used in low densities plasmas to measure line shapes, observe radiation redistribution, and determine the kinetics processes.

2) Future Experiments

The case illustrated below has several aspects. First will be to create a hot dense plasma of interest using the high-energy laser, second we can diagnose the plasma using various LCLS based probing techniques and third one can pump a selected transition to produce sensitized fluorescence [65]. Here we illustrate the photoionization arising from excitation of inner shell states. This will have two effects: 1) the experiment provides a critical test of the population kinetics models and, once we validate the population kinetics models, 2) it will provide a versatile *in situ* probe of the local temperature and indirectly the density via knowledge of the ionization balance. This has some advantages over Thomson scattering as the photo-absorption cross-sections are orders of magnitude larger and the signal will be strong even when employing only a small percentage of the LCLS. In a further development, we could the intense short pulse laser to create a fast electron beam providing a test of the underlying physical processes of the fast ignitor concept.

The simulation of the emission from atoms and ions provides one of the most unambiguous and powerful methods for the understanding of basic phenomena in laboratory and astrophysical plasmas. [66] An important underlying assumption is that atomic physics is sufficiently well known to accurately predict the spectral signatures. In high-density plasmas, however, particle correlations will alter the statistical mechanics of the free and bound states so that the internal states of the system are dependent on the plasma parameters: Continuum lowering, energy level modifications and altered spontaneous transition rates may occur. An extreme case would be the Warm Dense Matter regime discussed in Sec. V.A [67].

We study the effects of LCLS on the x-ray transitions of inner shell states, i.e., $K^0L^n \rightarrow K^1L^{n-1} + h\nu$, where K (L) represent the n = 1 (2) shells and the superscript is the number of electrons in the shell. These transitions connect the most strongly bound states in these systems. We will show that the LCLS can empty the K-shell preferentially producing hollow ion (HI) states. Importantly, HIs have negligible ground state populations and as the continuum absorption is negligible for x-rays it is clear that even for extreme density finite temperature matter the optical depths will be small. In contrast, visible and IR laser production of HIs in HDM samples is quite small, i.e., below the bremsstrahlung. Further, the x-ray induced HI production will far exceed those found in heavy ion beam surface interaction experiments [68] where only under low-density conditions does efficient HI production occur.

We show here that intense pulses of x-ray photons with parameters of the LCLS can generate spectra from HIs that is more than 13 orders of magnitude more intense than that created, e.g., in a visible laser-produced plasma experiments. This will make HI transition spectroscopy extremely important in the probing of high-density finite temperature matter.

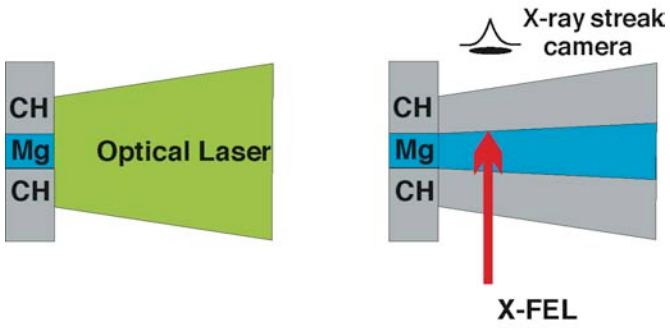

Fig. VI.B.1 Schematic sketch of a pump probe experiment

The basic scheme for a relevant experiment (pump-probe) is shown in Fig. VI.B.1 where a high-energy laser creates a dense plasma on a ps time scale that is then probed by the 100 fs duration intense narrow bandwidth tunable x-ray source, as indicated on the right hand side of Fig. VI.B.1. The simulation of the radiative properties involves atomic population kinetics together with radiation physics.

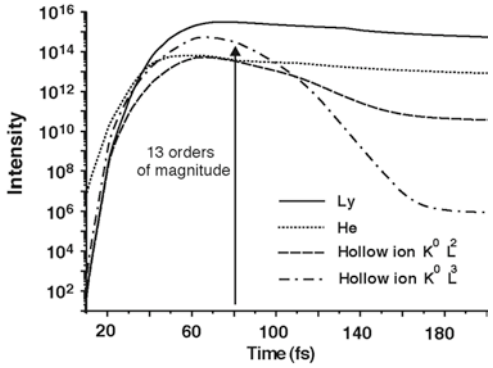

Fig. VI.B.2 Transient line emission of magnesium ions in a pump-probe driven configuration: $n_e=10^{21}$ cm^{-3}, T_e=30 eV, L_{eff} = 30 μm, I=9.2x10^{16} W/cm^2, E_{LCLS} =3.1 keV, ΔE=6.2 eV, focused to a 30 μm diameter spot with all photoionization channels.

In order to discuss the basic phenomena originating from an intense radiation field let us consider the HI transitions $K^0L^2 \rightarrow K^1L^1 + h\nu$ and $K^0L^3 \rightarrow K^1L^2 + h\nu$. Simulations show that the population of the HI configuration K^0L^2 and K^0L^3 is essentially driven by a chain of photoionization processes from autoionizing states:

$$K^2L^2 + h\nu \rightarrow K^1L^2 + e^-;\ K^1L^2 + h\nu \rightarrow K^0L^2 + e \text{ and } K^2L^3 + h\nu \rightarrow K^1L^3 + e^-;\ K^1L^3 + h\nu \rightarrow K^0L^3 + e$$

Figure VI.B.2 shows the time-dependent line emission of magnesium from the pump-probe experiment depicted in Fig. VI.B.1. In the figure the emission of several transitions is tracked: H-like $1s \rightarrow 2p$ (Ly_α), He-like $1s^2 \rightarrow 1s2p$ (He_α) and the HI transitions $K^0L^2 \rightarrow K^1L^1$, $K^0L^3 \rightarrow K^1L^2$. Here the simulation where all processes are included, for example, those to and from the states K^0L^2, $K^0L^1M^1$, K^0L^3, $K^0L^2M^1$. Indeed, it is found that if one disregarded these channels the HI emission would be reduced by more than 10 orders of magnitude. Due to large autoionizing rates - $\sim 10^{12}$-10^{15} s^{-1} - the HI states will rapidly decay; however, the 100 fs x-ray pulse is

sufficiently intense to initiate a chain reaction of inner-shell driven processes before destruction by autoionization. As can be seen from the Fig. VI.B.2 the x-ray pulse drives the HI emission up by more than 13 orders of magnitude to the level of the resonance line intensity, i.e., compare with Ly_α, which is well known to be observable [69]. That the x-ray pulse drives a sequence of photoionization processes efficiently can be seen from the intensity rise of Ly_α. That is, the dominant radiative process from the outer shell is photoionization: $K^0L^2 + h\nu \rightarrow K^0L^1 + e^-$

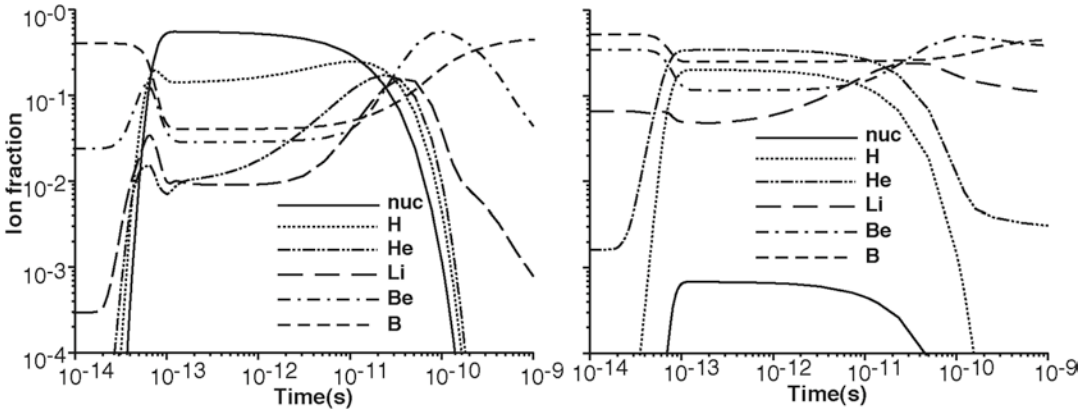

Fig. VI.B.3 Evolution of the ionic fraction of magnesium ions in a pump probe driven configuration. Left side: as Fig. V.C.2 but with $I=9.2\times10^{12}$ W/cm^2; right side as Fig. V.C.2 but with T_e = 40 eV, $I=5.3\times10^{12}$ W/cm^2, E_{LCLS} =1.85 keV, ΔE=6.0 eV

During the x-ray pulse, the plasma starts to over-ionize and the intensity of all line transitions decreases after about 60 fs. On the left hand side of Fig. VI.B.3 the ionic fractions from bare nucleus to B-like ions is shown. During the LCLS pulse the bare nucleus fraction rises rapidly toward unity indicating a strong over-ionization. When the pulse turns off strong radiative recombination leads to a re-population and a long lasting strong emission of the resonance lines, Ly_α and He_α .

The effect of over-ionization can be reduced by tuning the pump-probe spectral energy below the ionization threshold of H-like ions and by decreasing the laser intensity so that over-ionization does not occur during the laser pulse. The right hand side of Fig. VI.B.3 shows the ionic fractions for such a simulation. The LCLS pulse is adjusted to keep the fraction of bare nucleus below 10^{-3} and the H-like fraction below 0.3. Figure VI.B.4 shows the resulting time integrated Ly_α and HI emission on logarithmic and the linear scales. Since the LCLS intensity variation and energy tuning will allow optimization for the HI emission, the LCLS provides a versatile tool for the creation of this distinct regime.

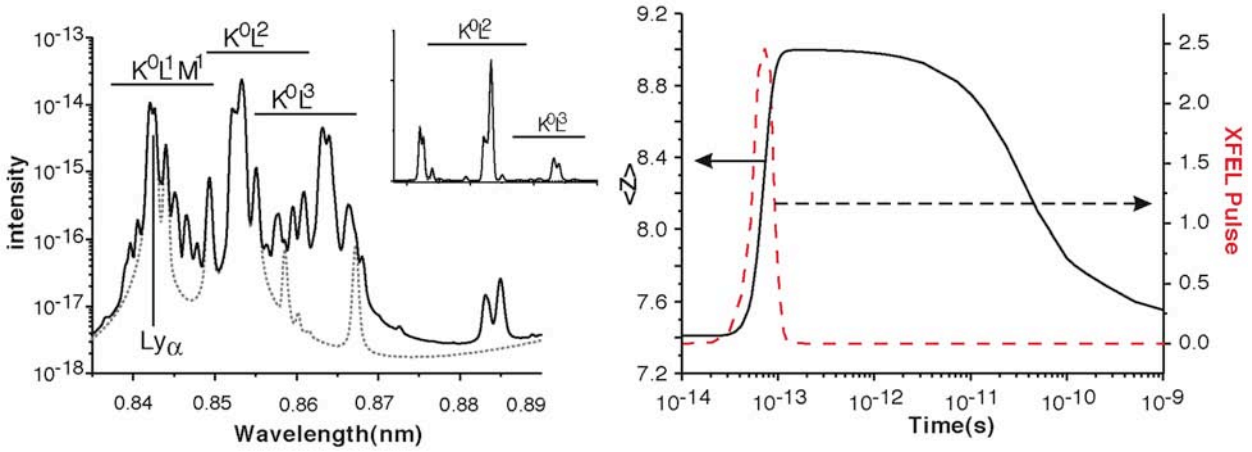

Fig. VI.B.4 On the left, the time integrated HI emission on a logarithmic scale, as right hand graph of Fig. VI.B.3 with L_{eff} = 10 μm. Inset shows the emission on a linear scale. The solid curve includes satellite transitions from the states K^0L^2, $K^0L^1M^1$, K^0L^3, $K^0L^2M^1$whereas the dotted curved includes only the transitions from K^0L^2. On the right graph shows mean ionization <Z> and LCLS pulse shape.

The question arises about the plasma heating due to LCLS pulse. For the simulation parameters of Fig. VI.B.3 the heating by the pump can be shown to be negligible, indicating that that the probe does not perturb the plasma conditions. We estimate an upper limit of the plasma heating by assuming all the photon energy is deposited and thermalized. With an initial temperature of T_e, the final temperature is

$$T_e^{LCLS}(eV) = T_e(eV) + 1.39x10^8\, I(W/cm^2)/n_e(cm^{-3})$$

which indicates that heating by the probe is negligible for the parameters of Fig. VI.B.3.

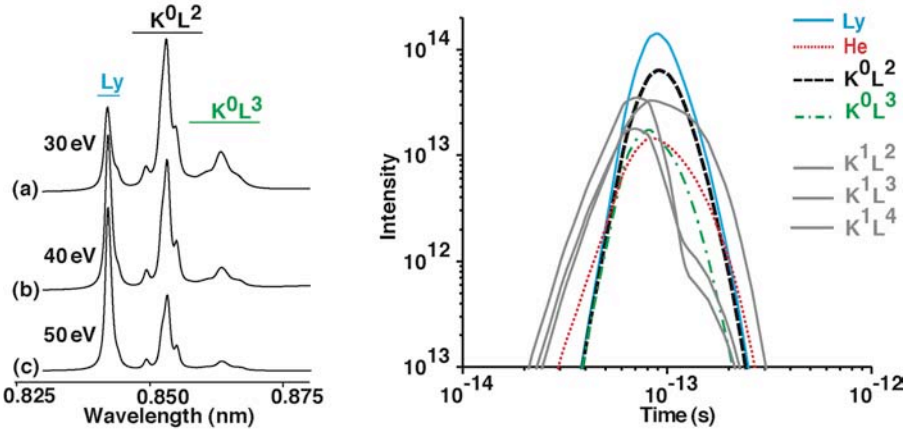

Fig. VI.B.5 Radiation emission induced by the LCLS pump (linear scale) in strongly coupled plasmas for different electron temperatures is shown on the left hand side, I_o = 5.5x10^{12} W/cm^2, n_e = 10^{23} cm^{-3}, L_{eff}=10 μm, E_{LCLS} = 1850 eV, (a) T_e = 30 eV, (b) T_e = 0 eV, (c) T_e = 50 eV. On the right hand side the transient x-ray line radiation emission is shown

Under the assumption that the probing of hot dense matter will provide the needed data to confirm the cross-sections and rate necessary to ensure accurate modeling of the inner shell kinetics, we now illustrate how the HI can be used to determine local plasma conditions. As the LCLS initiates efficient chain reactions of the type $K^2L^n \rightarrow K^1L^n + e^- \rightarrow K^0L^n + 2\,e^-$ it turns out that the relative intensity of the HI transitions $K^0L^n \rightarrow K^1L^{n-1} + h\nu$ and $K^0L^3 \rightarrow K^1L^2$ provide information about the electron temperature and mean ionization <Z>. Not only does the HI emission provide *in situ* diagnostic information in the weakly coupled regime, but it will provide time-resolved information in the strongly coupled plasma regime. In Fig. VI.B.5 curves a-c show the LCLS induced emission from Ly_α and the HI transitions for near solid density plasmas, $n_e = 10^{23}$ with temperatures of T_e=30, 40, 50 eV, while the right hand side shows the temporal behavior of the emission. For the selected irradiation parameters the emission is strong only during the LCLS pulse, which is distinct from the cases in Figs. VI.B.2 and VI.B.3. Thus, we obtain information on the ionization balance and the temperature, from the line HI line ratios, with temporal resolution $\sim 10^{-13}$ s. We note that for this case the ion-ion coupling parameter, $\Gamma_{ii} = 2.32 \times 10^{-7} \langle Z \rangle^2 n_i^{1/3} / T_i$, where n_i is the ion density and T_i the ion temperature in eV, approaches values greater than 10 proving that HI emission diagnostics will also effective in the strongly coupled plasma regime.

Note that more usual K_α satellite diagnostics are difficult in these situations as the satellites are also created during usual plasma heating processes. On the other hand, HI transitions can be excited only by strong LCLS irradiation and, thus, permit one to probe both high and low temperature regimes, associated with HDM and WDM, respectively. Moreover, compared to usual intense optical fs-laser pulses, which create extremely energetic electrons that affect the radiative properties employed for diagnostics, the LCLS pulse does not create hot electrons as it is in the classical regime with a small parameter $I\lambda^2$ [70]. Indeed one pf the evolutions of this technique would to study the plasmas formed by an intense short pulse laser.

We have shown that tunable sub-picosecond intense narrow-band x-ray sources can produce observable HI emission. Further, the ability to control the pump spectral energy and intensity will provide a method to probe the finite-temperature dense matter on sub-picosecond time scales due to the rapid emission characteristics of the K_α radiation. This radiation can provide information about temperature and density and, therefore, provides complementary information to x-ray scattering methods.

C) High Pressure States under High Strain

One of the most intriguing possibilities for the LCLS would be to measure the real-time organization of matter under high strain rate. To illustrate the potential we show the recent numerical simulations where a liquid collection of atoms at 5000 K are initially isothermally compressed by exponentially ramping the volume from an initial value of 121.6 au to 74.6 au with a time constant of 100 ps. In Fig. VI.C.1 the evolution of the solid fraction of the system, as well as the compression is shown. The point marked "*" notes the crossing of the equilibrium melt pressure for this temperature (43 GPa). Nucleation is seen to occur at (a), nearly 100 ps after the equilibrium melt pressure was reached. It is unclear at this time whether the delay represents a true lag for nucleation, or whether the pressure at this time (160 GPa) corresponds to a pseudo-spinodal for this system (e.g., the point at which solid nucleation can occur with

minimal energy barrier). We are currently performing simulations at different strain rates to investigate this further.

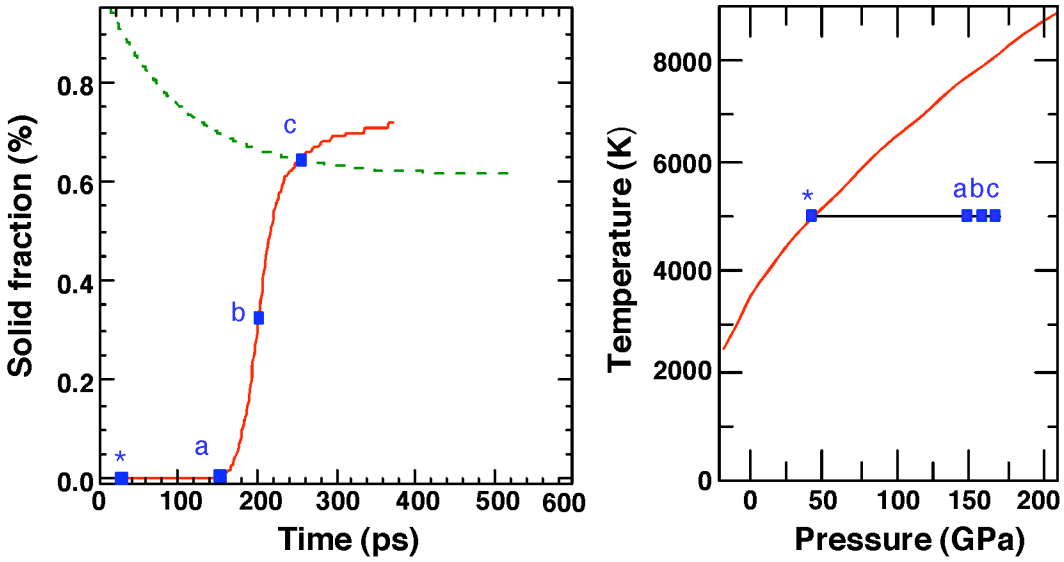

FIG. VI.C.1: On the left: the percentage of the simulation cell that has solidified as function of time (solid red line), along with the compression ratio (dashed green line). The melt curve for Ta is shown on the right hand side, which also depicts the isothermal compression path (black line). The labeled points refer to (*) the crossing of the equilibrium melt curve, (a) the onset of nucleation, (b) the period of explosive growth and (c) the onset of coalescence.

Regardless of the nature of the nucleation, rapid growth of the solid grains then occurs at point (b), with the solidification rate far exceeding the compression rate. This high growth period ends at point (c) when the grains have grown into each other, i.e., the onset of coalescence. At point (c), approximately 65% of the material has solidified - the remaining material comprises an extensive, percolating network of liquid and disorder separating grains of differing orientation. The percolation threshold is reached from above, as liquid is consumed by the growing solid. From this point forward the continued growth of grains is no longer accomplished by the speedy conversion of free liquid atoms but rather by the assimilation of smaller grains by larger grains - a far slower process mediated by the network of disorder that spans the simulation cell.

We display in Fig. VI.C.2 on the top row a time sequence of cross-sectional images obtained from slices of a 16M-atom simulation cell at the points marked as a through c, respectively, in Fig. VI.C.1. In the figure the atoms have been colored according to a parameter that is a measure of the correlation of local symmetry – blue represents atoms in a liquid-like environment, i.e., these have local symmetry which is poorly correlated; the red atoms possess a local symmetry which is highly correlated with their neighbors [71]. Finally, the yellow atoms identify a distinct population of "intermediate" atoms that occupy the interfaces and grain boundaries. Homogenous nucleation in the sample is seen to occur across the entire sample.

1) Experimental Considerations

To make the connection with the potential experiment at the LCLS, Belak [72] has used the 50 nm cube represented in the simulation shown on the top row of Fig. VI.C.2 as a sample to be

probed with the 100 fs 8 keV energy photons of LCLS. The time for the solidification to get from the initial liquid state to the final state shown in Fig. VI.C.2 is ~80 ps which implies that to resolve the processes would require ~10 ps resolution with sufficiently high signal to obtain a diffraction image. In the lower row of Fig. VI.C.2 we show the results of the diffraction simulations representing the three times in the simulation. The results for the initial liquid phase show a uniformly speckled ring pattern with indicating that the size of the grouped bismuth atoms is smaller then 50 nm. This result is typical of liquid diffraction. In the phase where the nucleation is starting to rise rapidly a similar ring pattern is observed with higher intensity region formed around the ring. The intensity and localization of these spots is a direct measure of the size of the nucleating sample. In addition one can see, with some difficulty in this representation, an inner ring that indicates that the Bi is organized into different structures. Finally, in the highly nucleated state the ring pattern with more bright spots of higher intensity indicating the number, size, and from of the cluster being formed.

A critical aspect of the scattering pattern signal is that each of the images would require a small fraction of the LCLS beam. Indeed, less than 10^{-3} of the 10^{12} photons would be used to make an image of the 50 nm cube of material. The would then allow one to use a split beam technique to obtain multiple 100 fs duration time-resolved images of the processes of interest.

The fact that the example starts with a liquid state and compresses it into a solid is a function of the simulation. As simpler experimental plan would be to expose the solid to a stress source and observe the change from solid toward a liquid as the sample becomes disordered.

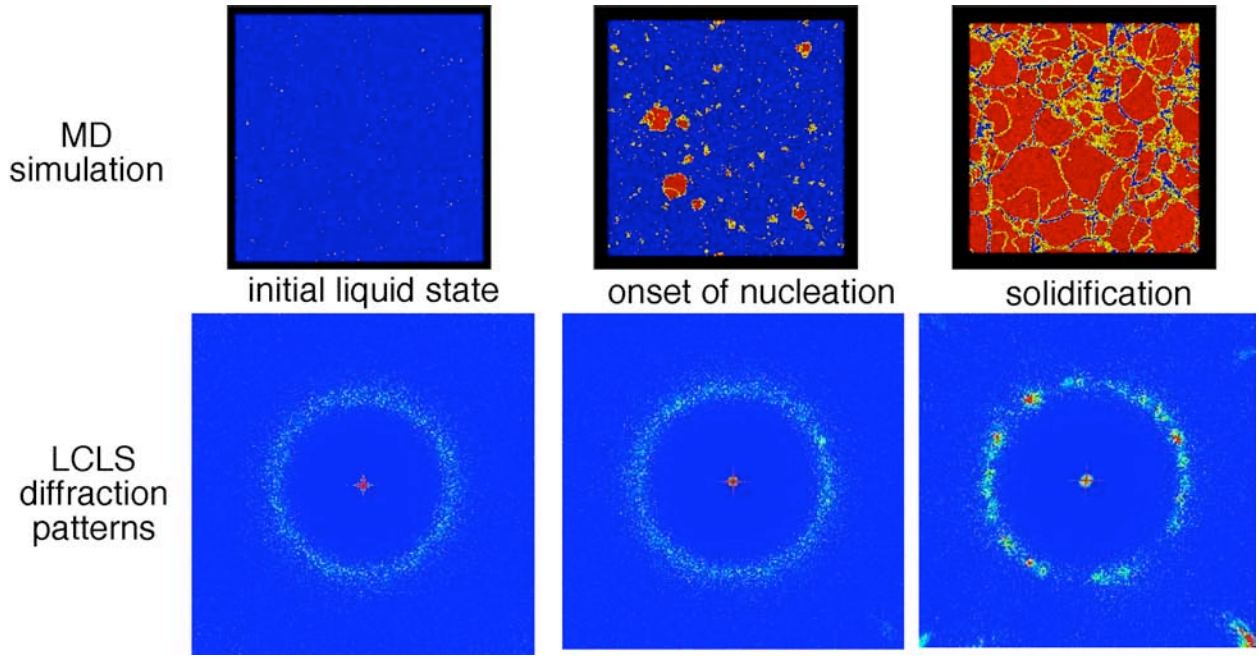

FIG. VI.C.2: Cross sections of the 16M-atom simulation are show on the top row. The image at the times in Fig. VI.C.1 labeled a through c going from left to right, respectively. The bottom row is a series of diffraction images created by passing ~10^7 8 keV photons through the sample at the times represents by a through c.

2) Requirements

The two possible approaches have been discussed in Section V.C.2, i.e., the direct laser irradiation of a reservoir material or the use of a laser-to-x-ray converter to irradiate a reservoir requires with a substantial mount of energy. Indeed, using these techniques requires laser energy of > 2 kJ to obtain the drive condition over areas that allow uniform conditions. Moreover, there are indications that one cannot drive the experiment at low energy. That is, in direct drive laser ICE rapid cooling at the ablation front results in a more rapid falloff after the peak of the ramp-compression wave in contrast to the indirect-drive technique described. In the indirect drive method the halfraum heat source decays more slowly. Below a certain E_{laser} the T_{rad} will be sufficiently low so that the heating associated with the ablatively driven shock will ionize the reservoir material. In this case, the material unloads across the vacuum-gap in a combination of low-density matter and solid fragments so that a secondary ramp drive will *not* be launched. This sets a lower P_{peak} limit in the ramp-compression wave, which is expected to be ~10 GPa.

Further, when one extends the studies of high-pressure matter to the case where there is high pressure, high strain and long times one arrives at the important study of the failure of matter under extreme conditions. Examples of studies where the spall of samples can be studied using lasers indicate that long pulse lasers could be quite useful. [73] This work reported on rapid laser-shock-driven melting, resolidification, and subsequent recovery of bismuth, in which estimated effective superheating and undercooling rates of order 10^{10} K/ s are achieved in bulk material. These rates were achieved by using a laser to drive the phase transition primarily with pressure changes rather than temperature changes. This technique opens a new avenue to study the bulk phase-transition behavior of materials driven far from equilibrium by rapid pressure transients. An important consideration is that long pulse drive is of great utility. Thus, laser pulse durations of > 100 ns can provide insight into the mechanisms of material strength after material has been subjected to high pressures.

3) Future Experiments

The lattice-level response of polycrystalline matter to shock compression is considerably more complicated than that of mono-crystalline matter. For example, it is well known that uniaxial strain can be made to prevail at the macroscopic level in many experiments, it not clear what actually occurs on the scale-length of a single grain and no doubt this will form an thrust area for non-equilibrium MD simulations in the future. Clearly, given that crystals are anisotropic, with in some cases vastly differing response according to crystallographic direction, it is not clear that uniaxial strain conditions hold at the length-scale of an individual grain. Indeed, even under elastic compression, or compression where few dislocations are generated and/or move, we might expect differing responses from individual grains, depending on their orientation, and hence differing reaction to a given imposed stress that will be a complicated function of the elastic compliances. The introduction of plasticity into the problem complicates matter further, and our understanding of the way individual grains react in such circumstances is in its infancy. How and on what time-scale such complicated granular response is accommodated to produce an overall uniaxial macroscopic response is still a matter for debate. Ultimately, what we wish to understand is how individual grains respond elastically and plastically to shock compression as a function of their orientation with respect to a given overall uniaxial shock wave, and the degree to which stress and/or strain is continuous across grain boundaries, i.e., in the terms of material

science, the degree to which the Voigt – where strain is uniform– or Reuss – where stress is uniform– conditions hold. The long-term goal of the interrogation via *in situ* x-ray diffraction of shocked-crystals at the granular level is to develop an understanding of the physics at the microscopic level that will inform mesoscopic, and ultimately macroscopic (continuum) models of the material in question that could be utilized, for example, in hydrodynamics simulation codes in order to model large-scale phenomena.

The x-ray FEL at LCLS has the potential to answer many of the fundamental questions of shock-induced plasticity alluded to above. The narrow divergence and bandwidth allow for diffraction from polycrystalline foils that have been simultaneously shocked with a synchronized optical laser, with the LCLS brightness being sufficient to ensure that the response of individual grains, of varying orientation with respect to the shock propagation direction, can be interrogated. The experimental design of choice will involve placing the shocked, polycrystalline foil at an angle to the incident x-rays, such that the normal to the target is not parallel to the incident x-rays, as this breaking of symmetry allows information to be gained about the response of grains making a variety of angles with respect to the direction of shock compression.

This can seen by noting that diffraction occurs when the difference between the scattered and incident k-vectors equals the reciprocal lattice vector of an appropriately oriented grain in the foil, thus producing a set of diffraction rings, the position of each ring being defined by the Bragg angle. However, the angle, a, between the reciprocal lattice vector **G**, and the surface normal, i.e., shock propagation direction, $\vec{N}$, is given by:

$$\cos(\alpha) = \cos(\theta)\cos(\phi)\sin(i) - \sin(\theta)\cos(i)$$

where θ is the Bragg angle, ϕ the azimuthal angle, and i the angle between $\vec{N}$ and the direction of the incident x-rays. Thus, by altering the angle i it is possible to tailor the instrument to look at sets of lattice planes within grains that have a range of orientations with respect to the shock propagation direction. The arrangement is illustrated in Fig. VI.C.3.

The micro-radian scale divergence of the LCLS beam will be far less than the rocking curve width, i.e., acceptance angle ,of an individual grain. Typically, ignoring defects, the acceptance angle of a grain is on the order of the number of unit cells across the grain. One must also take into account the finite bandwidth of the source (of order 0.1%). Then, within a shocked sample of 25 μm thickness, and an incident x-ray beam of order 300-μm diameter, we can expect close to 2 x10^6 grains for a grain-size of 1-μm. Given the bandwidth of LCLS, about 1000 to 2000 of these grains will diffract, yielding statistically significant information about deformation as a function of angle. Thus the LCLS 10^{12} photons per pulse would provide for each grain to diffract close to 10^5 photons, which will depend on the ratio of the acceptance angle of a grain compared with the bandwidth of the source. Nonetheless, it is very clear that there will be more than a sufficient number of photons scattered by each of the many grains to allow recording of its response.

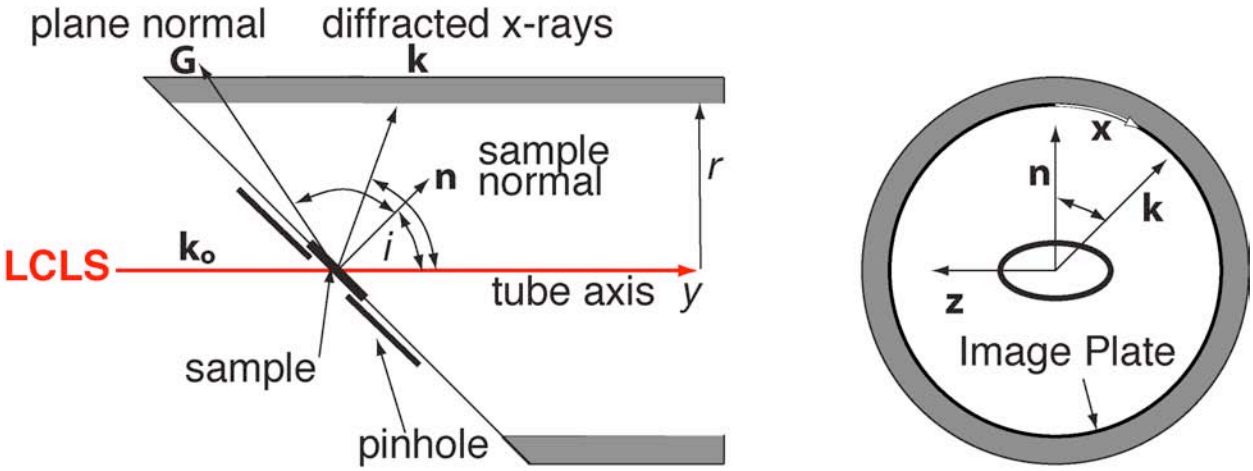

Fig. VI.C.3. A schematic diagram of a cylindrical pinhole powder camera diagnostic. The diagnostic consists of a tube radius r with axis along $\boldsymbol{y}$, one end of the tube is cut at the angle of the sample orientation, so that the same normal, $\boldsymbol{n}$, will make an angle i with respect to the tube axis. An image plate is wrapped around the inside of the tube, with distance x on the film given by the angle ϕ relative to the long side of the tube.

D) High Pressure Shocks and Phase Transitions

1) General comment on shock measurement at LCLS

The experiment that best fits the LCLS capability is powder diffraction from a micro-crystalline shocked sample. This would, most likely, require samples with sub-micron grain sizes, as the acceptance angle of a grain to diffraction would be about 10^{-4} to 10^{-3} radians. This implies one would want ~ 10^7 randomly oriented grains in a 300 μm diameter beam to get about 10^3 grains diffracting per diffraction ring. Then, assuming the shock travels 10 μm and the beam diameter is 300 μm, this indicates a grain size ~1 μm diameter. In some ways sub-μm grain sizes are not optimum, as 'normal' metals have larger grain sizes. On the other hand, 1 μm grains is much more closely associated with what one can achieve with MD simulations and will be a direct measure of the MD simulations. Thus, this is a excellent starting point.

2) Basic Requirements

First, we note that the laser energy needed to perform experiment at these pressures, i.e., near 500 kBar, is ~0.5 kJ at 0.5 μm wavelength. If the experiments require the use laser produced backlight one could use also use the residual energy of the high-energy laser to make a long pulse backlight or the short pulse intense laser to generate a shorter pulse. In fact, there are MD simulations that indicate that phase transitions in Fe occur on time scales much fast than expected, occurring on the 1 ps time scale. [74] These result indicate that the LCLS may be necessary to temporally resolve certain transitions as no other x-ray source could resolve the

There are two approaches to using a 4th generation x-ray source like the LCLS to measure dislocation densities. The simplest approach is actually to use the full bandwidth of the LCLS (0.3% bandwidth) to diffract from a laser-shocked crystal - we discussed above the parameters of

the optical laser required for shock compression of the single crystal. An analysis of the above pattern indicates that if we have 10^9-10^{10} photons, then for typical crystals, and diffraction from strongly reflecting planes (such as (002)) we would expect the bright central region in Fig. V.7 to correspond to of order 10 photons per square micron on a detector 10 cm from the shocked crystal – more than sufficient to provide single shot recording. Alternatively, one could arrange for the orientation of the shocked sample and the wavelength of the LCLS to be such that the Ewald sphere of diffraction of the quasi-monochromatic beam radiation intersects a significant portion of the 'streaks' along one of the particular <111> directions. In effect this corresponds to specular diffraction from (002), but in such a plane that the quasi-regular dislocation features add sidebands that deflect radiation at angles other than the normal Bragg angle. In either case only a single LCLS shot would be required.

3) Experimental Description

The X-ray FEL at LCLS also has the potential to provide considerable insight into the fundamental physics of shock-induced phase transitions. We provide as a candidate for first-light experiments an investigation into the shock response of iron on picosecond time-scales: not only is this the most well known, and indeed most widely-studied of shock-induced polymorphic phase transformations –where the original body-centered-cubic (bcc) lattice has been thought to transform to hexagonal close-packed (hcp)– but the transition is also of significance due to its relation to the millennia-old importance of iron in influencing the development of human civilization, as well as in geophysics, being the principal element within the earth's core. For reference the phase diagram is shown in Fig. VI.D.1. It is even speculated that the crystalline properties of the core have measurable affects on the surface. Furthermore, the relevance of the microscopic response of iron to shock compression to the missions of various national laboratories hardly requires emphasis. Due to this broadly interesting topic we provide the background for this experiment.

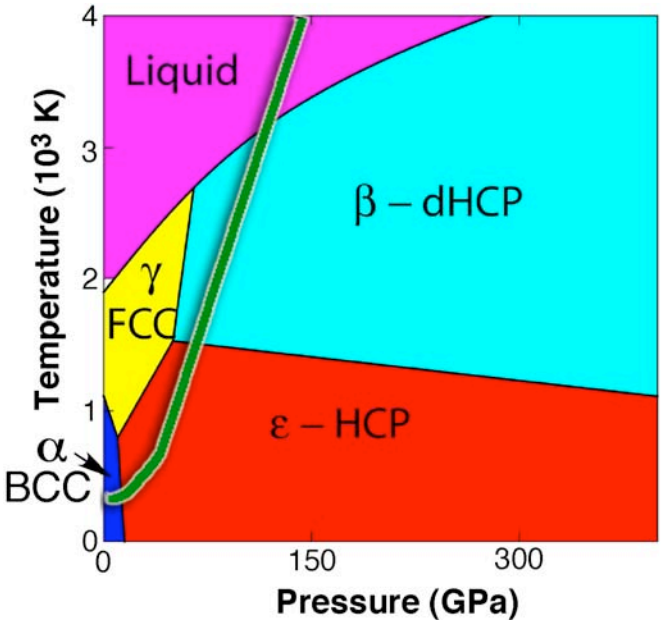

Figure VI.D.1. The Phase diagram of Fe. Black lines are known phases under static conditions [75]

and the green curve is the shock Hugoniot [76]

Interestingly, the current status of our knowledge of the response of iron on the lattice level to shock compression is at a crucial juncture where it is highly likely that the unique capabilities of LCLS will be of critical importance in furthering insight. In order to understand how the present situation has arisen, what that situation actually is, and where LCLS can play a pivotal role, we outline in brief below a (by necessity) partial history of the research in this area.

The first tentative evidence for this transition under shock conditions came half a century ago, when J.M. Walsh [77] reported data on the propagation of high-pressure shock waves in Armco iron that were in disagreement with an extrapolation of Bridgman's original low-pressure static compressibility measurements [78]. The discrepancy was resolved in the late 50's at Los Alamos by Bancroft, Peterson, and Minshall, [79] whose work indicated the existence of a multiple-wave shock structure within a single sample. They associated the splitting of the waves with plastic flow and then transformation of the iron to a different phase. Analysis of the wave profiles implied that the onset of the phase transition occurred at a pressure of 130 kbar. At that time the α-e, i.e. bcc – hcp, phase transition was unknown and it was speculated that it could possibly be the α-γ phase transition, bcc-fcc which was known to occur at ~1000 K at standard pressure. Initial electrical resistivity tests under static pressure were inconclusive in confirming the observed shock-induced phase transition, and as a result the validity of Minshall's data was called into question. Much of the criticism directed towards the then newly-emerging field of shock physics was no doubt due in part to the difficulty in believing that a solid-solid phase transition could occur on a sub-microsecond timescale.

It was only several years after Minshall's shock-wave work that the crystallographic evidence for a bcc-hcp transition at 130 kbar was obtained in static X-ray diffraction experiments by Jamieson and Lawson in the early 1960's [80]. This confirmation that a phase transition occurred under static conditions at an (almost) identical pressure to that deduced from the earlier shock-wave measurements effectively countered the doubts that had been expressed about the shock techniques, and this discovery of one of the most important phase transitions known to man has long been hailed as one of the major triumphs of the field of shock-wave physics. It has been assumed ever since that the transition associated with the multiple-waves seen in shock experiments and that observed under static high-pressure conditions are one and the same transition.

Even so, it was by no means clear that the fact that new wave profiles appear in the shock data at pressures the same, or at least close to, those seen in static experiments, implies that the phases under shock and static compression are the same. In particular the shear stress experienced by crystals under the two different techniques can be radically different: in static measurements the crystals are, as far as is possible, compressed under hydrostatic conditions, with no intentionally imposed shear. On the other hand, in planar shock wave experiments the crystal sample is subjected to uniaxial strain and hydrostatic conditions are only approached if significant plastic flow occurs (driven by the high shear stress) before the transition pressure is achieved, or if during the transition itself significant shear stress is relieved; even then the material will retain some degree of strength, ensuring that hydrostatic compression could only ever be an approximation, with some residual shear stress remaining. Thus on ultra-fast time-scales, before significant plastic flow may have had time to occur, there may be very significant

differences between the conditions experienced by the sample from the two techniques, and these differences may well alter not only the path taken to the new phase, but perhaps even the phase itself.

This was the situation at the end of the last millennium - classic shock wave techniques using the analysis of wave profiles, showed that transition took place under shock conditions - the pressure was the same as that for the bcc-hcp transition seen under static high-pressure experiments, but no direct evidence concerning the crystallographic phase under shock compression had ever been recorded. Of course, the reason for this lack of direct evidence was the fact that the transition is completely reversible - so that if a shocked sample is recovered, only the original bcc lattice remains. The only answer from an experimental point of view was the development of transient diffraction techniques to diagnose the shocked lattice in situ.

It is in this context that several recent seminal pieces of work should be viewed. The first was a several million-atom molecular dynamics simulation by the Los Alamos group. [81]. In this MD simulation, they used the well-known Voter-Chen embedded atom potential [82] to shock compress a single crystal of iron along the (001) axis. They clearly observed the bcc to hcp phase transition (which in the simulation took place on sub-picosecond timescales), and readily identified the transition mechanism. The transition is displacive - Martensitic - and the atoms "click" into place with the degenerate (110) axes of the original bcc phase becoming the c-axes of the new hcp phase. Interestingly, they saw no evidence of any plasticity, such that the length of the c-axis in the hcp phase was exactly $\sqrt{2}$ times the lattice parameter in the original bcc phase. The transition took place once the bcc phase had been compressed by 6%, with a sudden collapse into the hcp phase with compression between 15 and 18% depending upon the applied shock pressure.

Second, on the experimental front the results of these simulations were confirmed by an LLNL/LANL/Oxford collaboration where a nanosecond laser-plasma-based quasi-monochromatic diverging X-ray source was used to analyze the lattice of a single crystal of iron shock compressed along (001).[83] The agreement between experiment and MD simulations was remarkable, with the experiments also demonstrating an almost complete lack of plasticity, a rapid collapse to the hcp phase once the bcc phase had been uniaxially compressed by 6%, clear period doubling to the two-atom per unit cell hcp phase, and exactly the same relative orientation of the two phases as predicted.

It might be thought at this juncture that the story of the phase transition in iron was nearing its conclusion; however, this is far from the case. Just as the LLNL/LANL/Oxford collaboration published these ground-breaking single-crystal results, the Los Alamos MD group published further simulations that are, perhaps, of even greater significance. Firstly, they predicted that if one shocked single crystals of iron along the <110> or <111> directions, a significant fraction –close to 50%– of the crystal will actually transform to the γ (fcc) phase, rather than the ε (hcp) phase. [84] It is difficult to overestimate the importance of this prediction and the need to test it experimentally. The Huguniot of shocked Fe does *not* go through the γ phase as determined from static measurements. The LANL prediction is consistent with the concept that because of the large shear stresses present within a shock, which are absent in the static diamond-anvil-cell experiments, one can not simply overlay the pressure-volume Hugoniot onto a static phase diagram to determine the phases present under shock conditions. Yet that is

what is often done within the shock wave community, mainly, of course, because there has never been any direct structural information about the phase present during the shock conditions. An experimental confirmation of the LANL prediction would therefore have huge consequences for the whole field of shock waves in condensed matter, in that it would confirm that one can no longer blithely make the assumption that the phase under shock compression corresponds to the one seen under hydrostatic conditions. Unfortunately, these predictions have been, at least thus far, impossible to verify using laser-plasma based X-ray sources. It is thought that the difficulty is associated with the fact that it is predicted that the mixed hcp/fcc phase comprises many small crystallites that results in such angular broadening of the diffraction signal that it can not recorded with a laser plasma source –although, of course, this would not be true with LCLS.

Furthermore, pertinently, since that time an LANL/Oxford collaboration has shown that MD simulations predict that uniaxially-shocked polycrystalline iron is, on sub-nanosecond timescales, a mixture of the ε and γ phases.[85] In some ways this is unsurprising as the original MD simulation, for shocks along (001), predicted pure hcp, but along single crystal (111) predicted a mixture of hcp and fcc. Evidently a polycrystalline sample will always have grains randomly oriented with respect to the shock direction. Indeed, the relative fraction of hcp/fcc material within a particular grain is predicted to be a function of the orientation of that grain with respect to the shock propagation direction. A grain that is oriented such that the shock direction is along one of the principal crystallographic axes, e.g., (001), is almost entirely comprised of the hcp phase, whereas a grain where the (111) axis lies along the shock propagation direction is likely to have more fcc material within it than hcp material.

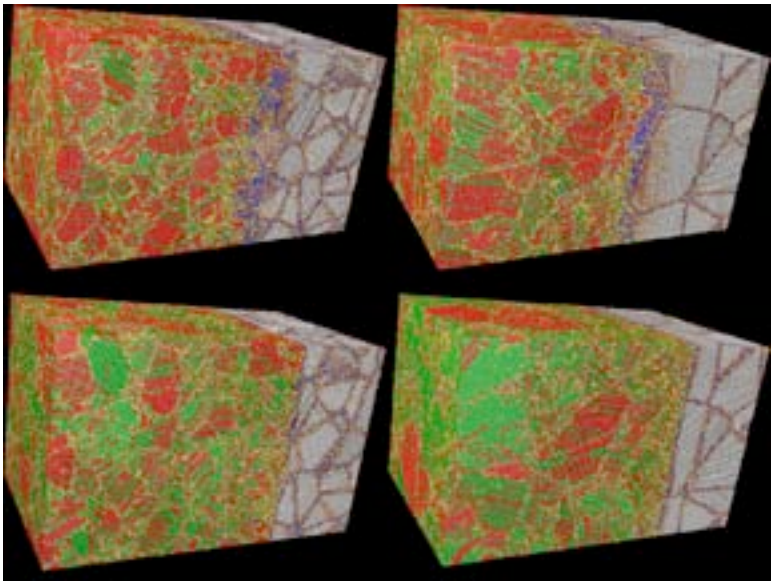

Figure VI.D.2 MD simulations of the response of polycrystalline iron to uniaxial shock compression at four different pressures above the pressure for the bcc-hcp transition. The atoms are colored according to coordination number: gray is the ambient bcc lattice; blue is shock-compressed bcc phase; green is fcc; and, red hcp

In order to illustrate this Fig. VI.D.2 shows MD simulations of the response of polycrystalline iron to uniaxial shock compression at four different pressures above the pressure for the bcc-hcp transition. The important point to note is the prediction that a considerable

fraction of the lattice in the phase-changed region is in the fcc phase, rather than hcp, which we recall is the conventional wisdom. It is also worth stating that the LANL/Oxford team have performed simulations with other forms of iron potentials, and all gave similar results – thus, the prediction that a shock may mechanically force atoms into a non-equilibrium phase does not seem to be simple a peculiarity of the Voter-Chen potential, but may be related to the fact that both hcp and fcc are close-packed structures, and on the timescale of uniaxial shock compression, the mechanical forcing of atoms along particular directions may play a more dominant role in the structure, at least on these picosecond timescales, than the phases that might ultimately be determined by equilibrium thermodynamics.

It is at this critical juncture that LCLS affords the potential to resolve these issues - that is, the LCLS is ideally suited to diagnosing polycrystalline shocked samples on the relevant picosecond timescales, being an ultra-bright, non-diverging, close-to-monochromatic source. As we have already mentioned above, in our discussion concerning the diagnosis of shock-induced plasticity in fcc (copper) samples, the Debye-Scherrer rings that will be produced by passing the monochromatic LCLS beam through a polycrystalline sample will provide a rich vista containing critical information in the particular case of uniaxially shocked samples. As noted, the breaking of the symmetry afforded by placing the shocked sample at an angle to the incident X-ray beam results in a dependence of the diffraction pattern on the azimuthal angle that is a function of the angle made by a particular grain to the shock direction. Furthermore, varying the angle made by the incident X-ray beam with respect to the shocked foil can alter this dependence. We note that this is precisely what is required since the MD simulations clearly predict two things for shocked polycrystalline iron foils: 1) The foils will actually be a mixture of hcp and fcc phases, *not* solely hcp as is normally thought, and 2) the relative fraction of these two phases is a function of the orientation of a grain with respect to the shock propagation direction. Thus the relatively simple experimental set-up of a laser-shocked iron foil, placed at various angles with respect to the LCLS beam, with diffraction rings recorded on relatively simple detectors, could well provide the most useful information on shock-induced displacive phase transitions to date.

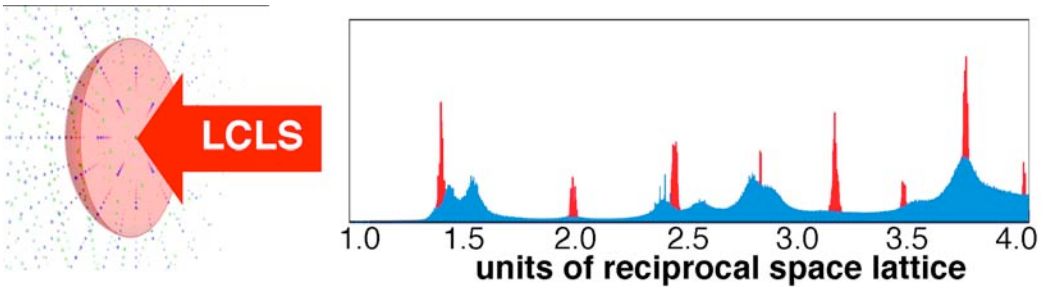

Figure VI.D.3. A simple schematic of the experiment on the left hand side and the results of the diffraction from polycrystalline Fe is shown is Fig. VI.D.2. The red signal derives from the unshocked (bcc) and blue is shocked material. The shocked material will be a mixture of the first wave, which is compressed bcc, and the hcp.

For a polycrystalline sample, many different lattices in k-space are oriented according to the grain orientation, with the same origin. To date there are not yet simulations with sufficient grains to meaningfully simulate the powder camera response; however, one can do a radial average. The results are show on the right hand side of Fig. VI.D.3 Large grain number simulations will be performed in the future.

VII) Discussion of Benefits to NNSA

A) Strategic coupling of NNSA to SC

Due to the interdisciplinary nature of high energy density science there is no single funding agency that could support the diverse and vast range of applications. Thus, the support for HED science comes from several federal agencies, each supporting a subset of the total. Note that the definition of the high energy density application space, as discussed here, does not coincide with those in the various federal reports [36, 37, 38] where, for example, astrophysics, nuclear physics, and ultrafast ultraintense laser science are included. That is, in this document we have discussed topics relevant to the NNSA mission. These topics represent a board set of research fields that require substantial scientific resources to develop solution to many of the intriguing and cross-disciplinary areas.

The most obvious coupling provided by the HEDS endstation at LCLS is the creation of a strong tie between the two components of DOE, the Office of Science (SC) and the National Nuclear Security Administration. The HEDS endstation would provide a venue, the LCLS, where a substantial subset of scientific experiments of interest to NNSA can be performed. Further, the Office of Basic Energy Sciences (BES), within SC, operates the LCLS. This would be a unique and complementary capability for the following reasons:

- *Maintenance of scientific quality in the future requires the active encouragement of a broad community to develop novel ideas.* As the high energy density science discussed here has become a subsidiary of NNSA support, establishing collaborations with an existing peer review process and, generally, increasing the number of researchers involved will be important in promoting a broadened scientific community.

- *Coupling of the BES mission to the NNSA mission provided by the HEDS endstation will augment the range of applications on x-ray light sources.* The current use of BES x-ray light sources for HEDS has been small, with the use of BES facilities being limited to two specific areas. The first is the study of non-thermal melt [86], which has been resolved. The second is the high-pressure experiments at the Advanced Photon Source (APS) beamline called HPCAT, commissioned in 2005,[87] where NNSA is a partner with SC in the operation of HPCAT. NNSA scientists have used HPCAT to produce forefront high-pressure data.[88] The beamline was also a crucial element of an intensive investigation of the effects of radiation damage – "aging" – on plutonium. HPCAT is an ideal example of scientific relevance and productivity made possible by NNSA leveraging a major SC-funded facility.

- *LCLS will operate as a user facility*, as do the other BES x-ray light sources, which allows science based peer group review to provide the oversight of the quality of the proposed science. The success of the x-ray light source model for users is well documented in the literally thousands of users at the four BES light sources. The range of applications on the extant light sources is also quite large and the interaction of this user base with those interested in the HEDS provides cross-fertilization that will assist both NNSA and SC.

- *NNSA will have several high-energy facilities where external user time will be available constrained*. However, the major facilities covered under this new policy (the National Ignition Facility at LLNL, Omega/Omega EP at LLE / University of Rochester, and the ZR/Z-Beamlet/Petawatt at Sandia National Laboratories) will have at most 15% of the shot time allocated to science support.

- *Major NNSA HEDS facilities are large in scale and require substantial training* and support from the facility, as utilization is extremely complex. Technique validation and preparation time will have to be performed on medium- or small-scale facilities. The use of the HEDS endstation would enhance the capability to perform technique development and provide preliminary validation for experiments that may migrate to the large-scale NNSA HEDS facilities.

- *Leverage for NNSA in the LCLS is substantial as the SC investment is large*. The incremental cost is small and both parties benefit substantially from the interactivity.

B) Building a Broad-based Scientific Community

Concerning the proposal for a High Energy Density Science capability at the LCLS (Linac Coherent Light Source), the 4th generation x-ray light source currently under construction at SLAC we note that the National Task Force on High Energy Density (HED) Physics, which was commissioned by the Interagency Working Group on the Physics of the Universe, and chaired by Prof. R. Davidson, had the defining interest in the promulgation, coordination, and development of HED physics in the community. It is in this regard the committee report [37] strongly supported the development of the HED capability for several reasons.

The Task Force made general recommendations in its final report and the proposed HED science capability at LCLS is extremely well aligned with several of these. First, the Task indicated "…a fusing of research capabilities and intellectual interests provides many new opportunities for scientific discovery… In addition, there are strong indications of latent research opportunities that are not so explicitly delineated. For example, the potential benefit of co-locating facilities such as intense particle or laser beams and light sources offers exciting new possibilities. One type of driver could be used to create and the other to probe new and fundamentally different states of matter…" The LCLS-based capability with the kJ class laser, the 100 TW short pulse laser and the intense, tunable, short-pulse LCLS x-ray laser will provide precisely the type of facility that was envisioned.

Second, the Task Force indicated that the field of HED science cuts across several fields of research having common physics issues and intellectual challenges. One example, understanding the fundamental properties of warm dense matter is an aspect of each of the four major research areas included in the report: astrophysics, beam-induced high energy density studies, Stockpile Stewardship, and ultrafast intense laser science. The Task Force commented "…Warm dense matter consists of extreme states of matter that are neither in a 'cold, condensed-matter' state, nor in a 'hot, plasma' state, but rather somewhere intermediate. Warm dense matter is typically a strongly-coupled, many-body charged particle system with energy density in the10^{11} J/m^3 range, conditions that are extremely difficult to study analytically and by numerical simulation. Many astrophysical systems, e.g., brown dwarfs, and giant planets, and laboratory experimental conditions fall into this regime…" The LCLS-based HED capability will be ideally

well situated to explore the warm dense matter regime whether it is created by shocks using the high-energy laser or directly by the volumetric heating with the x-ray laser. Indeed, this is one of the many examples where several of the fields of research have common interest.

Third, the Task Force found that there is a "need for a range of facilities to provide a cost-effective national research program." The example employed in the Report to illustrate this point is particularly relevant to the Department of Energy since "…a range of facilities is essential to perform experiments at increasing energy/current in order to develop experimental and diagnostic techniques before carrying out experiments on the larger facilities such as the National Ignition Facility (NIF) or the Z/ZR facility, where operating costs are high. This range of experiments will also help to validate the simulation capabilities, physics understanding, and target fabrication techniques, and ensure the success of the limited number of experiments possible on the largest facilities. It is unlikely that experimental run time would be awarded on the largest facilities in the absence of concept demonstrations on the smaller facilities. An effective facility usage plan would attract additional high quality researchers to the field, thereby increasing the number of trained scientists and benefiting the field of high energy density physics in the long term." By this example it is clear that a light source-based capability would be well adapted to the need as the light source model of facility use stands out as amongst the most successful in the scientific world.

Fourth, we note that the Task Force included specific recommendations pertaining to the general area of laser-driven HED physics the primary one was "Access to kJ-class facilities is essential to develop the scientific basis, experimental techniques, diagnostics, and simulation capabilities, including access by foreign nationals. If the present facilities cannot support this, either because of over-subscription, site access, or cost issues, then a new kJ class laser facility should be constructed and operated with user access at an open site." As the target users include, amongst others, university faculty members and their students and postdoctoral research associates the issue of access is a major consideration in the development of the field.

In summary, it is clear that this proposal for a HED effort at LCLS with its multiple drivers, housed at SLAC operating under the aegis of the Office of Science as a user-oriented capability will greatly advance the creation of a well-focused national policy on HED science and will become the leading research tool, unrivaled in the world.

C) Technique Development on LCLS

The development of techniques that can be used to interrogate plasmas, solid density matter both hot and warm, and provide *in situ* probes for matter at extreme conditions is a goal of numerous experimental efforts within the NNSA laboratories. These efforts are central to understanding, e.g., the implosion dynamics found in ICF experiments. Obviously, the Mission-oriented researchers will be the prime movers in these efforts. Further, the efforts are costly, large-scale research efforts incorporating large teams of people. Thus, an important consideration is where to develop the initial proof of principle techniques that are to be employed on larger scale laser or pulsed power systems? One answer is, the LCLS, which would be an experimental capability with a versatile laser source and provides unique diagnostic information to corroborate the results.

The development of techniques is one area of LCLS applications where the Mission

oriented researchers will have a large effect on the building or the HEDS community. Here these researchers will not only be part of the user base of the LCLS endstation but will be important collaborators in the development of capability of broad range of applications on the LCLS.

VIII) Appendices:

A) Workshop Agenda and Participant List

Wednesday, December 6, 2006 Building 543, Grand Canyon Room Unclassified Session		
Session I: Introduction to the workshop and overview		
8:30 a.m.	Welcome and logistics for the workshop	K. Budil, LLNL; J. Glownia, LANL
8:45 a.m.	NNSA Perspective on HEDS and LCLS	C. Keane, NNSA: ICF and NIF project
9:00 a.m.	LCLS and LUSI projects	J. Hastings, SLAC: LUSI Project
10:00 a.m.	HEDS end station project proposal	Budil
10:30 a.m.	BREAK	
Session II: Experimental techniques		
10:45 a.m.	LANL perspective	Fernandez
11:45 p.m.	LUNCH	
1:00 p.m.	X-ray Thompson scattering	Glenzer
2:00 p.m.	Material Dynamics techniques	Taylor/ Funk/ Lorenzana
3:30 p.m.	WDM techniques	Cauble/Benage/Murillo
4:30 p.m.	EOS Techniques	Collins
5:30 p.m.	ADJOURN	
Thursday, December 7, 2006 Building 111, Poseidon Room Classified Session		
Session III: Weapons physics introduction		
8:30 a.m.	Welcome and logistics for the workshop	Budil/ Glownia
8:45 a.m.	Secondary physics perspective	Wan/ Batha
9:45 a.m.	Primary physics perspective	Graziani/Reinovsky
10:45 a.m.	BREAK	
Session IV: Weapons physics issues and opportunities		
11:00 a.m.	WDM and discussion	Cauble/Benage/Murillo
12:30 p.m.	LUNCH	
1:30 p.m.	HDM and discussion	Shepherd/ Workman
3:00 p.m.	Materials and discussion	Belak/Streitz/Hixson/Germann
4:30 p.m.	Wrap-up and path forward	All
5:00 p.m.	ADJOURN	

Name	Institution	E-mail	Telephone
Barty, Christopher	LLNL	siders2@llnl.gov	(925) 423-8486
Batha, Steve	LANL	sbatha@lanl.gov	(505) 665-5898
Belak, Jim	LLNL	belak1@llnl.gov	(925) 422-6061
Benage, John	LANL	benage@lanl.gov	(505) 667-8900
Budil, Kim	LLNL	budil1@llnl.gov	(925) 423-8098
Caird, John	LLNL	caird1@llnl.gov	(925) 422-6159
Cauble, Robert	LLNL	cauble1@llnl.gov	(925) 422-4724
Cross, Rick	LLNL	cross1@llnl.gov	(925) 423-3817
Dunn, James	LLNL	dunn6@llnl.gov	(925) 423-1557
Erlandson, Al	LLNL	erlandson1@llnl.gov	(925) 423-3709
Falcone, Roger	LBNL\UCB	rwf@berkeley.edu	(510) 486-6692
Fernandez, Juan C.	LANL	juanc@lanl.gov	(505) 667-6575

Fulton, Doug	LANL	dfulton@lanl.gov	(505) 667-2652
Funk, David J.	LANL	djf@lanl.gov	(505) 667-9659
Germann, Tim	LANL	tcg@lanl.gov	(505) 665-9772
Glenzer, Siegfried	LLNL	glenzer1@llnl.gov	(925) 422-7409
Glownia, Jim	LANL	jglownia@lanl.gov	(505) 665-2527
Goodwin, Peter	LANL	pmg@lanl.gov	(505) 665-2506
Graziani, Frank	LLNL	graziani1@llnl.gov	(925) 422-4803
Hall, Clint	SNL	chall@sandia.gov	(505) 845-3300
Hastings, Jerome	SLAC	jbh@slac.stanford.edu	(650) 926-3107
Hawreliak, James	LLNL	hawreliak1@llnl.gov	(925) 424-2905
Hixson, Rob	LANL	hixson@lanl.gov	(505) 667-1964
Hsing, Warren	LLNL	hsing1@llnl.gov	(925) 423-2849
Keane, Chris	DOE	chris.keane@nnsa.doe.gov	(202) 586-0852
Kwan, Thomas	LANL	tjtk@lanl.gov	(505) 667-3447
Lee, Richard W.	LLNL	lee32@llnl.gov	(925) 422-7209
Lorenzana, Hector	LLNL	hlorenzana@llnl.gov	(925) 422-8982
Mailhiot, Christian	LLNL/NNSA	mailhiot1@llnl.gov	(925) 422-5873
Molander, Bill	LLNL	molander1@llnl.gov	(925) 423-9637
Murillo, Michael S.	LANL	murillo@lanl.gov	(505) 667-6767
Nelson, Art	LLNL	nelson63@llnl.gov	(925) 422-6455
Nilsen, Joseph	LLNL	jnilsen@llnl.gov	(925) 422-4766
Nitta, Cynthia	LLNL	nitta1@llnl.gov	(925) 423-3792
Oddone, Pat	LBNL	ploddone@lbl.gov	(510) 486-4600
Osterheld, Al	LLNL	osterheld1@llnl.gov	(925) 423-7432
Reinovsky, Bob	LANL	bobr@lanl.gov	(505) 667-8214
Rodriguez, George	LANL	rodrigeo@lanl.gov	(505) 665-3408
Satha, Steve	LANL	sbatha@lanl.gov	(505) 665-5898
Schwartz, Adam	LLNL	schwartz6@llnl.gov	(925) 423-3454
Schmitt, Mark	LANL	mjs@lanl.gov	(505) 665-7522
Shepherd, Ronnie	LLNL	shepherd1@llnl.gov	(925) 423-7456
Siders, Craig	LLNL	siders2@llnl.gov	(925) 424-4058
Springer, Paul	LLNL	springer6@llnl.gov	(925) 423-9221
Streitz, Fred	LLNL	streitz1@llnl.gov	(925) 423-3236
Taylor, Toni	LANL	ttaylor@lanl.gov	(505) 665-0030
Wan, Alan	LLNL	aswan@llnl.gov	(925) 423-3342
Williams, Jeff	LLNL	williams20@llnl.gov	(925) 422-6395
Wootton, Alan	LLNL/NNSA	wootton1@llnl.gov	(202) 586-0839
Workman, Jonathan	LANL	workman@lanl.gov	(505) 665-1784

B) LCLS Description:

1) Background

A free-electron laser (FEL) is a device for producing coherent radiation from a high-energy electron beam [89]. It has some similarity to an undulator source of synchrotron radiation, but whereas undulator radiation derives from electrons that are randomly spaced (on a scale of the radiation wavelength) the FEL incorporates a mechanism for longitudinal bunching of the electrons with the same period as the radiation (microbunching), so that the radiation emitted by the electrons is coherent [90]. The radiation field itself, bathing the electrons as they move through the undulator at relativistic speed, drives the microbunching. In order for the

microbunching to be effective, the electrons and radiation field must couple well. In particular, the emittance of the electron beam must match the emittance of the diffraction-limited coherent radiation field. This condition can be achieved for micrometer-wavelength radiation using electrons in a low-emittance storage ring [91], but even the large third-generation light source rings cannot support FEL action at x-ray wavelengths.

It is possible in principle to achieve the necessary conditions for an x-ray FEL using a high-energy linear electron accelerator. In 1992 it was first pointed out that the linear accelerator at the Stanford Linear Accelerator Center (SLAC) should be capable of driving an x-ray FEL [92]. Interest in this idea has grown, and has resulted in a project called the Linac Coherent Light Source (LCLS) [93, 94].

The LCLS will utilize one third of the 3-km SLAC Linac to accelerate an extremely bright electron pulse. During a single pass through a long (100m) undulator, this pulse will initiate FEL action at the undulator fundamental wavelength, which will be tunable between 15 Å and 1.5 Å. The FEL will operate in Self-Amplified Spontaneous Emission (SASE) mode, meaning that the FEL radiation field will arise from amplification of the spontaneous undulator radiation created at the start of the long undulator.

Due to the extremely short and bright electron pulse, and due to the exponential FEL amplification, the radiation produced by the LCLS will have unique properties. Its peak brightness will be about ten orders of magnitude greater than that of a third-generation synchrotron light source, its pulse length will be about three orders of magnitude shorter, and it will exhibit complete spatial coherence. These properties offer unprecedented opportunities in many fields of science [95, 96]. The specifications of the radiation generated at the LCLS is given in Table VIII.B.1

Laser (FEL) Specifications:	**15 Å**	**1.5 Å**	**Units**
RMS pulse duration	137	73	fs
Peak 1st FEL harmonic power	5	8	GW
Energy/FEL pulse	2.1	2.0	mJ
Number of photons/FEL pulse	12	1.1	10^{12}
FWHM FEL source size	116	86	μm
FWHM FEL source divergence	5.7	0.8	μrad
1st harmonic RMS FEL Rayleigh waist	49	36	μm
1st harmonic FEL Rayleigh length	10	54	m
1st harmonic homogeneous bandwidth S	0.07	0.03	%
1st harmonic inhomogeneous bandwidth D	0.19	0.07	%
Peak 1st FEL harmonic power density (@10m)	3	11	10^{11} W/mm^2
Peak 1st FEL harmonic field (@10m)	1.4	2.8	10^{10} V/m
Spontaneous Emission Specifications:	**15 Å**	**1.5 Å**	**Units**
Peak spontaneous power	4.1	73	GW
Time-averaged spontaneous power	0.24	2.2	W
90% total power bandwidth	0.006	0.025	keV
FWHM source size (far field)	120	85	μm
FWHM source divergence (far field)	8.6	2.7	μrad

Table VIII.B.1 The specifications of the LCSL radiation source for the lower and upper wavelength ranges. There is also 3rd harmonic radiation at 1/3 the wavelength with approximately 1% of the energy per pulse.

2) Organization of the LCLS Project

The LCLS construction project involves formal participation from four institutions (SLAC, Argonne National Laboratory, Lawrence Livermore National Laboratory, and the University of California Los Angeles) and informal collaboration with individual scientists from a number of other facilities. The Project Director is John Galayda of SLAC. Some of the participating institutions have taken on responsibility for particular aspects of the project. For instance, Argonne will develop the long LCLS undulator, and LLNL will develop the x-ray optics.

The project is funded by the US Dept. of Energy, Basic Energy Sciences Division. A funding baseline was established in 2005, with a total project cost of $379M. Major conventional construction began in 2006. First light is expected in the summer of 2008, and in April 2009 the LCLS construction project will terminate and operation as a DOE user facility will commence.

In the operational phase, the LCLS facility will operate for 4000-6000 hours per year as a DOE user facility, with an anticipated annual operating budget of roughly $50M. The LCLS facility will be managed by the Photon Sciences Division of SLAC, which also manages the Stanford Synchrotron Radiation Laboratory.

3) LCLS Experimental Facilities

Figure VII.B.1 show the general plan for the LCLS experimental areas. There will be three shielded enclosures (x-ray hutches) in the Near Experimental Hall, located about 150m from the FEL source, and three hutches about 400m from the source in the Far Experimental Hall. A single FEL source serves all of the x-ray hutches, so that in general only one experiment can use the source at a time. X-ray optics are planned to allow the FEL beam to be switched between experiments within a few minutes. Some optics under consideration would split the beam and allow simultaneous operation of two experiments, with reduced intensity for each. The LCLS construction project includes funding to fully instrument one experimental station. This station, which is in Hutch 2 in the Near Experimental Hall, is intended for studies of the interactions between intense x-ray pulses and single atoms or small atomic clusters. Instrumentation for additional experimental stations, for studies in the areas of chemistry, condensed-matter science, and biology, will be provided by a separate DOE BES project known as LCLS Ultrafast Science Instruments (LUSI).

Though the initial LCLS construction will provide only one FEL source and 6 experimental stations, the LCLS facility could in future be expanded to support several FEL sources and more than 20 experimental stations.

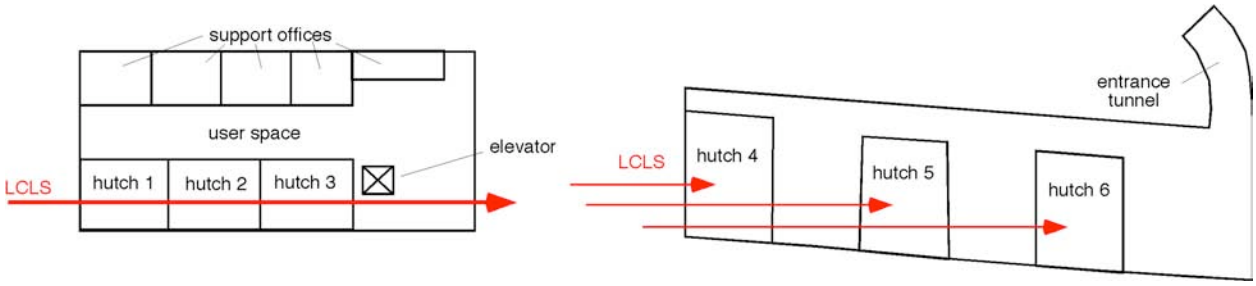

Fig. VIII.B.1 On the left. the Near Experimental Hall, which is ~150m from the FEL source. Each experimental enclosure (hutch) is roughly 10m square. On the right, the Far Experimental Hall is shown, which is ~400m from the FEL source. There will be optics to direct the beam into each of the hutches. The two halls are not drawn to the same scale.

C) High Energy Density Capability Description

1) Experimental equipment requirements

The following is a set of experimental equipment defined by a group of researchers involved with the definition of the initial Letter of Intent for experimental capabilities on the LCLS. The group was comprised of approximately 40 researchers from the US and 60 from overseas. The equipment will be used in the tow experimental areas, one in the far experimental hall of the LCLS and the other in the Laser building. The latter is a stand-alone facility that can operate independently of the LCLS.

- *Target Chamber and Optical Components*
  - Target chambers with vacuum pumping
  - Target alignment and rastering capability with real time viewing of the target.
  - In-vacuum translational 3-axis manipulator for foils with an alignment precision of 5 μm.
  - Sample transfer device without the need to break vacuum.
  - Collection optics to record incident and scattered spectrum simultaneously to deconvolve the scattered spectrum composed of: X-ray mirrors, crystals, and spectrometers
  - Beam splitting and delay optics
  - Attenuators (10^{-4})
  - Fast shutter
  - Optical laser energy diagnostics for energy transmitted, the energy scattered, and the energy reflected
  - Optical laser beam transport

• *Experiment Specific needs*

- Pulsed gas jet capable of operation at 10 Hz with a backing pressure of several 10's of atmospheres
- Pin diodes and CCDs with various filters for EUV, XUV, X radiation monitoring
- High efficiency XUV and X-ray spectrometers with resolving power of 10^4 (with capability for 10^5 for certain experiments) to be coupled to a streak camera and/or CCD
- X-ray / XUV streak camera with better than 200 fs temporal resolution with a temporal range up to the picosecond time-scale
- X-ray / XUV streak camera with ~2-5 ps temporal resolution with a temporal range up to the nanosecond time-scale
- Monochromator for X-ray Thomson scattering and optical pumping experiments
- A hemispherical electron analyzer to measure the electron energy per pulse
- TOF mass- and electron-spectrometers
- Fourier domain interferometric arrangement, including beam splitting, Michelson interferometer, the pulse recombining in a UV spectrometer with a CCD detection system
- CCD detector for diffraction experiment
- VISAR system to optically monitor shock breakout
- Optical Streak Cameras for temperature measurements on shocks
- Optical imager gated for spatially monitor WDM production
- Gated X-ray imager
- Sample fabrication equipment
- Harmonic generation setup – XUV and Visible relay optics, filters, XUV gratings

2) Short Pulse High Intensity Laser

A short pulse laser with 30 fs pulse length and ≥ 1 J in a high contrast pulse synchronized to the LCLS operating at 10 Hz. This will be used for: Plasma production; Foil heating, Fourier Domain Interferometry; backlight generation and Thomson Scattering ($n_e \leq 10^{22}$ cm^{-3}).

A system of this type is commercially available and it installed in several laboratories. A schematic of the system is shown below in Fig. VII.C.1

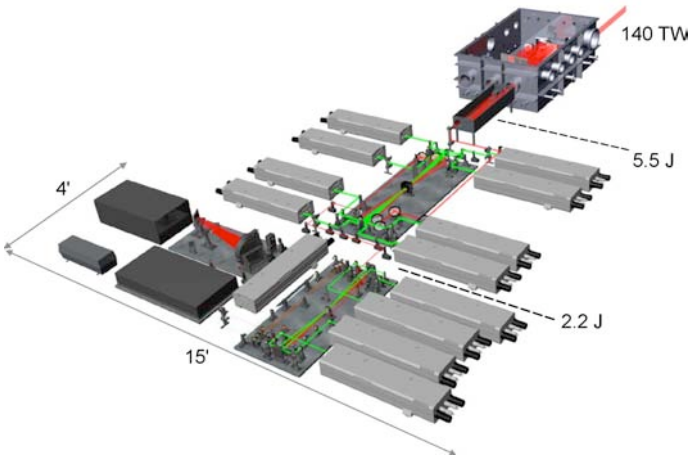

Figure VIII.C.1 A schematic of a intense short pulse system now operating at the University of Nebraska under the leadership of D. Umstadter. The system provides 140 TW, in 25 fs pulses of 3.5 Joules/per pulse and operates at 10 Hz.

3) Long Pulse High Energy laser:

High energy laser for shock generation and plasma production will be required. The minimum energy would be on the order of 100 Joules, with maximum of 4 kJ, at wavelengths of ~ 500nm. The pulse length would vary from ~100 ps to > 100 ns. The system will include the ability to generate shaped pulses up to 1 μs in duration. The design incorporates final amplification in Nova 31.5-cm disk amplifiers.

The system will include pulse temporal shaping in the front end and will be designed to accommodate long ($\approx\mu$s) drive laser pulses. A series of rod amplifiers will boost the energy to the Joule level, which is then injected into the final 4-pass, 31.5-cm disk amplifiers. Two configurations were evaluated for size and performance: either 11-m or 18-m focal length lenses in the final relay telescope.

System architecture:

1) fiber-based front end with pulse shaping, output $\approx$ 0.1 μJ

2) single/double-pass amplifiers, spatial filter relays, output $\approx$ 10 mJ

3) 32-mm rod amplifier, 4-pass, output $\approx$ 3 J

4) 31.5-cm disk amplifiers, 4-pass with U-turn

5) beam transport, frequency conversion, and target chamber

The estimated output energy at 1053 nm is shown as a function of pulse duration in Figure VIII.C.2. System performance can be optimized in several ways: Figure A.1 shows three possible configurations. Frequency conversion can be added in the relay output plane. The beam output diameter is 24-26 cm.

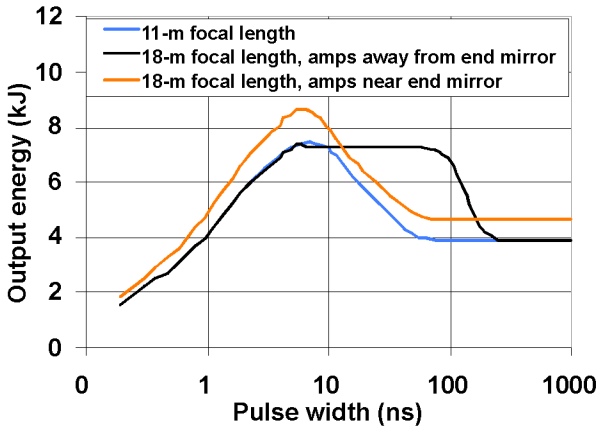

Figure VIII.C.2. Estimated system 1053-nm output energy as a function of pulse duration

4) Laser Hall:

A rough system layout is shown in Figure VIII.C.3. The 160' length by 75' wide. Approximately 12000 sq ft are required in the configuration shown to allow corridors, entranceways, and facilities. A break down of the room sizes is:

1) main laser bay 4200 sq ft, includes 420 sq ft clean room
2) power conditioning, 800 sq ft
3) control room, 800 sq ft
4) gowning area, 100 sq ft
5) beam transport and endstation area, 500 sq ft
6) Fabrication room, 400 sq ft
7) Short pulse laser room, 900 sq ft

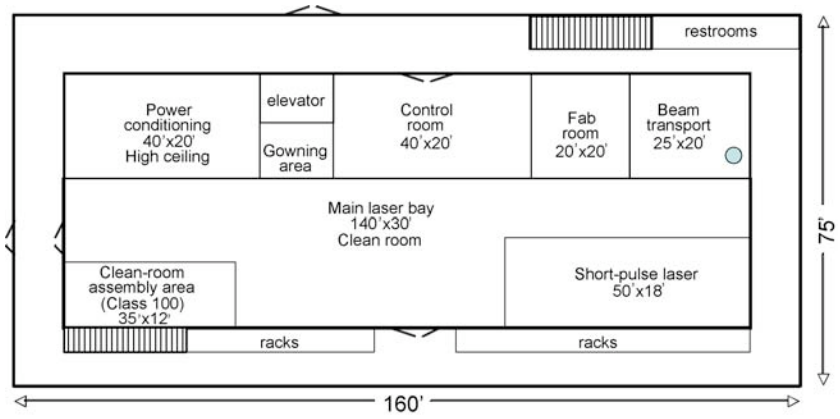

Figure VIII.C.3. The layout of the laser hall

This is a meant to be a conservative estimate. Space requirements may be reduced by further design optimization and system tradeoffs.

5) The Hutch in the far experimental hall of LCLS

The experiments to be carried out in the far experimental hall will require the availability of both the high-energy laser and the intense short pulse laser. These lasers will be taken from the Laser Hall through a beam pipe in the beam transport room, see the blue circle in Fig. VIII.C.3. The short pulse laser will be transported after it is chirped to a long pulse and recompressed in the Hutch. The high-energy laser will be transported at full aperture and focused in the hutch. Figure VII.C.4 shows the schematic of the two lasers applications.

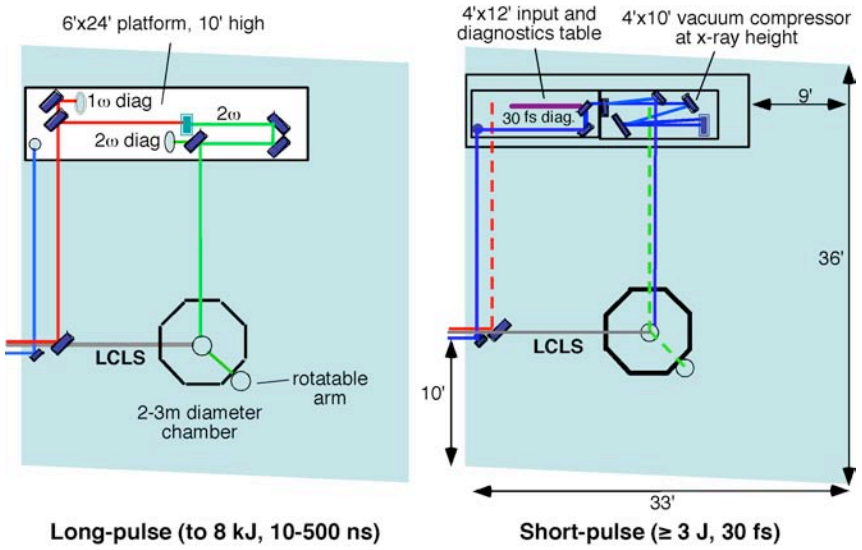

Figure VIII.C.4 The schematic layouts of the HEDS hutch in the far experimental hall of the LCLS. The Left hand side shows the configuration for the introduction of the high energy laser into the target chamber. The right hand side, which shows the dimension, indicates the introduction of the intense short pulse laser into the target chamber.

On the left is the high-energy laser is introduced into the hutch at 10' and directed to the upper platform of a two platform 6'x24' table. The high-energy laser is then frequency doubled, if required, and transported to the chamber via a rotatable mirror that can direct the beam into the various entry ports. The intense short pulse laser is transported to the hutch at the same height and the beam is directed down to the lower platform where it is compressed to a short pulse. The beam is then transported to the target chamber through a vacuum beam tube. The LCLS comes into the chamber at a lower height and goes directly into the chamber.

IX) References

1 H. Daido, Rep. Prog. Phys. **65** 1513 (2002); G. Tallents et al., Laser Part. Beams **20**, 201 (2002) and the references therein

2 R. W. Lee, R. Petrasso, and R.W. Falcone "Science on High Energy Lasers", University of

California Report UCRL-ID-119170 (1996) and http://www.llnl.gov/science_on_lasers/
3 D.E. Hinkel, et al., Phys. Plasmas **13,** 112701 (2005); D.E. Hinkel, et al., Phys. Plasmas **12,** 056305, (2005) ;
4 E. L. Dewald et al. Phys. Rev. Letts **95**, 215004 (2005)
5 J. D. Huba (2000) *NRL Plasma Formulary* (Office of Naval Research. Washington. DC) http://wwwppd.nrl.navy.mil/nrlformulary/nrlformulary.html
6 R. M. More *et al.*, Phys. of Fluids, **31**, 3059 (1988)
7 See*, e.g.*, K. S. Trainor, J. of Appl. Phys., **54**, 2372 (1983)
8 T. Guillot, Science **286**, 72 (1999)
9 M. N. Rosenbluth and R. Z. Sagdeev,. *Handbook of Plasma Physics*, ***3****, Physics of Laser Plasmas. (*Elsevier, Amsterdam, 1991)
10 J. Sheffield, *Plasma Scattering of Electromagnetic Radiation* (Academic, New York, 1975) and references therein
11 H.-J. Kunze, in *Plasma Diagnostics*, Ed. W. Lochte-Holtgreven, (North-Holland, Amsterdam, 1968)
12 C. A. Back, C. Chenais-Popovics, and R. W. Lee. *Phys. Rev. Letts.* **63**, 1471, (1989); C. A. Back, C. Chenais-Popovics, and R. W. Lee, *Phys. Rev.* A **44**, 6730 (1991)
13 J. A. Koch, et al., J. Quant Spec. Rad. Trans. **54**, 227-236 (1995)
14 M. E. Foord, et al., J. Quant Spec. Rad. Trans. **65**, 231, (2000)
15 A. Bar-Shalom, J. Oreg, J. and M. Klapisch *Phys. Rev.* A **38**, 1773, (1988)
16 R. Ramis et al., Comp. Phys. Comm., **49**, 475 (1987); K. Eidmann, Laser Part. Beams **12**, 223, (1994)
17 A. Loveridge-Smith, et al., Phys. Rev. Lett., **86**, 2349-52, (2001)
18 B. Holian and P.S. Lomdahl, Science 26; 280: 2085-2088, (1998)
19 E. M. Bringa et al., Nature Mat. **5**, 805 (2006) and references therein
20 A. Rosalankova and J. Wark, Private Communication, (2006)
21 P. Soderlind and J. A. Moriarty, Phys. Rev. B **57**, 10340 (1998).
22 B. A. Remington et al., Met. Mat. Trans. **35A**, 2587 (2004)
23 K. G. Hoge and A.K. Mukherjee: J. Mater. Sci., **12**, 1666 (1977)
24 D. J. Steinberg and C.M. Lund: J. Appl. Phys, **65**, 1528 (1989)
25 D.L. Preston, D.L. Tonks, and D.C. Wallace: J. Appl. Phys., **93**, 211 (2003).
26 V.A. Raevski, Report for Task I under Agreement No. B512964 (2001).
27 J. F. Barnes et al., J. Appl. Phys., **45**, 727 (1974); and **51**, 4678 (1980).
28 J. Edwards et al., Phys. Rev. Lett. **92**, 075002 (2004).
29 R. F. Smith, et al., Phys. Plasmas **14**, 057105 (2007)
30 D. Rothman, et al., J. Phys. D **38**, 733 (2005)
31 J.-P. Davis, J. Appl. Phys. **99**, 103512 (2006)
32 K. T. Lorenz et al., Phys. Plasmas **12** 056309 (2005); K. T. Lorenz et al., High Energy Density Physics, **2**, 113 (2006)
33 S. D. Rothman, et al., J. Phys. D **35**, 3021 (2002); S. D. Rothman et al., Phys. Plasmas **9**, 1721 (2002) .
34 R. F. Smith, et al., Phys. Rev. Lett. **98**, 065701 (2007)

35 J. Sheffield, *Plasma Scattering of Electromagnetic Radiation* (Academic, New York, 1975) and references therein
36 "Frontiers in High Energy Density Physics: The X-Games of Contemporary Science", Committee on High Energy Density Plasma Physics, Plasma Science Committee, National Research Council (R. Davidson et al.); "Connecting Quarks with the Cosmos: Eleven Science Questions for the New Century" the National Academy of Sciences (M. Turner et al.)
37 *Frontiers for Discovery in High Energy Density Physics,* Prepared for the Office of Science and Technology Policy National Science and Technology Council , Interagency Working Group on Physics of the Universe - www.ofes.fusion.doe.gov/News/HEDPReport.pdf - (R. Davidson et al.)
38 "Interagency Task Force Report on High Energy Density Physics" prepared for National Science and Technology Council, Committee on Science by the Interagency Working Group on the Physics of the Universe, - www.science.doe.gov/News_Information/Report of the Interagency Task Force on High Energy Density Physics.pdf
39 R. W. Lee, Joint Proposal for Peak Brightness Experiments on TTF-FEL; "Plan for TTF-II First Experiments" Private Communication
40 S. L. Johnson, et al., Phys. Rev. Lett. **94**, 057407 (2005); S. L. Johnson, et al., Phys. Rev. Lett. **91**, 157403 (2003)
41 D. A. Reis, et al., Phys. Rev. Lett. **86**, 3072-3075, (2001)
42 A. M. Lindenberg, et al., Phys. Rev. Lett. **84**, 111-114, (2000)
43 S. H. Glenzer, et al., Phys. Rev. Lett. **90,** 175002, (2003); S. H. Glenzer et al., Phys. Plasmas **10,** 2433, (2003)
44 G. Gregori, et al., Phys. Rev. E. **67,** 026412, (2003); G. Gregori, et al., J. Phys. A **36**, 5971, (2003)
45 H. Sawada, et al., 47th APS/DPP Denver, Colorado,24 Oct (2005)
46 W. Schülke Handbook on Synchrotron Radiation, **3** , G. Brown, D.E. Moncton (eds.), Elsevier, (1991)
47 D. Pines, Phys. Rev. **92,** 626, (1953)
48 S. H. Glenzer, et al., Phys. Plasmas 6, 21178, (1999)
49 A.J.Mackinnon, et al., Review of Sci. Intrum. **75**, 3906, (2004)
50 G. Gregori, et al., Phys. Plasmas **11**, 2754-2762, (2004)
51 G. Gregori, et al., J. Quant Spec. Rad. Trans. **99**, 225, (2006)
52 J. Chihara, J. Phys. F: Met. Phys. **17**, 295, (1987)
53 A. Hoell, et al., Eur. Phys. J. D **29**, 159 (2004)
54 S. Ichimaru, "Statistical Plasma Physics, Volume I: Basic Principals, Volume II: Condensed Plasmas" (Addison-Wesley, New York, 1994)
55 M. Fajardo, et al., J. Quant Spec. Rad. Trans. **71**, 317 (2001) and references therein
56 D. D. Burgess and C. H. Skinner, *J. Phys. B* **7**, L297, (1974)
57 G. Razdobarin, et al., Nuc. Fusion **19**, 1439, (1979)
58 R. C. Elton, *X-ray Lasers* (Academic Press, San Diego, 1990*)*
59 H. A. Scott, J. Quant Spec. Rad. Trans. ,**71**, 6891, (2001)
60 D. R. Kania, et al., Phys. Rev. A **46**, 7853, (1992)
61 J. A. Koch, et al., J. Quant Spec. Rad. Trans. **54**, 227, (1995)

62 J. C. Moreno, et al.. *Phys. Rev*. E **51**, 4897, 1995.
63 K. Widmann, et al., Phys. Plasmas **8**, 3869 (2001); K. Widmann, et al., Phys. Rev. Lett **92,** 125002 (2004): T. Ao, et al., Phys. Rev. Lett **96,** 055001 (2006)
64 A. Forsman, et al, Phys. Rev. E **58**, R1248 (1998)
65 G. Winans and R. M. Williams, Phys. Rev. **52**, 930 (1937)
66 D. Mihalas *Stellar atmospheres* (W. Freeman and Co., San Francisco, 1978); H. R. Griem *Principles of Plasma Spectroscopy* (Cambridge University Press, 1997); C. de Michelis and M. Mattioli, Nuc. Fusion, **21**, 677, (1981)
67 R. W. Lee et al., J. Opt. Soc. Am. B, **20,** 1, (2003)
68 J.-P. Briand et al., Phys. Rev. Lett., **65**, 159, (1990).
69 F. Rosmej et al., Phys. Rev. E **66**, 056402, (2002).
70 S. Gitomer et al., Phys. Fluids **29**, 2679, (1986)
71 P. R. tenWolde, M.J. Ruiz-Montero and D. Frenkel, Phys.Rev. Lett. **75**, 2714 (1995)
72 J. Belak, very private communication (2007)
73 J. D. Colvin, et al., J. Appl. Phys. **101**, 084906 (2007)
74 K. Kadau et al. Phys. Rev B, **72**, 064120, (2005)
75 S. K. Saxena and L. S. Dubrovinsky, Amer. Mineral. **85**, 372 (2000).
76 J. C. Boettger and D. C. Wallace, Phys. Rev. B 55, 2840 (1997) and C. S. Yoo et al., Phys. Rev. Lett. **70**, 3931 (1993)
77 J. M. Walsh and R. H. Christian, Phys. Rev. **97**, 1544 (1955)
78 P. W. Bridgman, J. Appl. Phys. **27**, 659 (1956)
79 D. Bancroft, E. L. Peterson, and S. Minshall, J. Appl. Phys. **27**, 291 (1956)
80 J. C. Jamieson and A.W. Lawson, J. Appl. Phys. **33**, 776 (1962)
81 K. Kadau, et al., Science **296**, 1681 (2002)
82 A.F. Voter and S.P. Chen, in "Characterization of Defects in Materials", R. W. Siegel, J. R. Weertman, and R. Sinclair, eds. Mater. Res. Soc. Symp. Proc. No. **82** (Materials Research Society, Pittsburgh, 1987), p. 175; and, A.F. Voter, Los Alamos Unclassified Technical Report No. LA-UR 93-3901, 1993 (unpublished)
83 D. Kalantar, et al., Phys. Rev. Lett. **95**, 0755021 (2005)
84 K. Kadau, et al., Phys. Rev. B **72**, 064120 (2005)
85 K. Kadau, et al., Phys. Rev. Lett. **98**, 135701 (2007)
86 A. M. Lindenberg et al., Phys. Rev. Lett. **84**, 111 (2000); S. L. Johnson et al., Phys. Rev. Lett., **91**, 157403/1-4 (2003) and references therein
87 High Pressure Collaborative Access Team, www.hpcat.aps.anl.gov/
88 See, for example: B. J. Baer et al., Phys. Rev. Lett. **98**, 235503 (2007); A. Lazicki et al., Phys. Rev. B **75**, 054507 (2007); V. Iota et al., Appl. Phys. Lett. **90**, 042505 (2007); V. Iota et al., Nature Mat. **6**, 34 (2007); G. W. Lee et al., Proc. Nat. Acad. Sci. **104**, 9178 (2007); B. R. Maddox et al., Phys. Rev. Lett. **96**, 215701 (2006); W. J. Evans et al., Chem. Mat. **18**, 2520 (2006); A. Lazicki et al., Phys. Rev. Lett. **95**, 165503 (2005).
89 J. Madey, J. Appl. Phys. **42**, 1906, (1971)
90 J. Murphy and C. Pellegrini, J. Opt. Soc. Am. **B2**, 259, (1985)
91 An internet site at the UC Santa Barbara contains links to information about FELs around the world. The address is: http://sbfel3.ucsb.edu/www/vl_fel.html

92 W. Barletta, A. Sessler, and L.-H. Yu, in "Workshop on Fourth Generation Light Sources", M. Cornacchia and H. Winick, eds., SSRL Report 92/02, 376 (1992)
93 LCLS Design Study Report, SLAC Report 521 (1998), see http://www-ssrl.slac.stanford.edu/lcls/design_report/e-toc.html
94 LCLS Conceptual Design Report, SLAC Report 593 (2002), see http://www-ssrl.slac.stanford.edu/lcls/cdr/
95 See http://www-ssrl.slac.stanford.edu/lcls/science.html
96 *LCLS the First Experiments*, G.K. Shenoy and J. Stöhr, eds., SLAC (2000) see http://www-ssrl.slac.stanford.edu/lcls/BESAC_TALKS_OCT2000.HTML